ABSTRACT

BARDALL, AARON RYDER. Static and Dynamic Influence of a Fluid Droplet on a Soft Deformable Solid. (Under the direction of Michael Shearer).

Here I present an in-depth look at the modeling and analysis of the influence of fluid droplets on soft solids both in static and dynamic cases. The study resides in the field of elastocapillarity, or the interaction of elastic and capillary influences. The interplay of these two effects leads to interesting phenomena not limited to those discussed in this thesis. Capillary energy in the form of liquid surface energy, the result of free energy from unbalanced molecular bonds at the fluid phase interface, influences the geometry of fluids seeking an energy minimizing shape. In the case of soft solids and fluids interacting, liquid surface energy generates forces which act to alter the shape of the solids introducing strains and elastic energy to the system. In the case of droplets resting on soft solids, the competition between equilibrium surface and elastic energies results in solid deformation in the form of a wetting ridge at the three phase triple point, or contact line.

We develop a model describing the influence of a resting droplet on a solid surface. From the model we obtain quantities such as the displacement of the solid, and resulting geometry of the deformed surface, as well as strains and stresses within the solid. This is done for two dimensional and three dimensional droplet geometries, as well as the separate scenario of a thin elastic rod being partially submerged in a fluid.

In the case of the two dimensional droplet geometry, we introduce spatial gradients in solid substrate properties, specifically the stiffness and solid surface energies. Consequently, equilibrium deformations in the solid substrate upon which the fluid rests become spatially asymmetric. The effects of this asymmetry are investigated as a potential source for inducing droplet motion, which has been observed experimentally for some scenarios such as solid thickness gradients. We quantify the resulting physical configuration of the system for a given substrate gradient. The absolute difference in apparent contact angle formed at the front and back of the fluid droplet is used as a benchmark criterion for the induction of droplet motion. Ultimately we find that given current experimental feasibility, a stiffness gradient is predicted to be insufficient to induce droplet dynamics. In contrast to this we find that a gradient in surface energy is capable of inducing motion of a fluid droplet over the surface of a soft solid. Dynamic droplet velocities for our feasible scenario are then predicted using a dissipation argument presented in the last chapter.

Static and Dynamic Influence of a Fluid Droplet on a Soft Deformable Solid

by
Aaron Ryder Bardall

A dissertation submitted to the Graduate Faculty of
North Carolina State University
in partial fulfillment of the
requirements for the Degree of
Doctor of Philosophy

Applied Mathematics

Raleigh, North Carolina

2019

APPROVED BY:

_____   _____
Karen Daniels   Mansoor Haider

_____   _____
Ralph Smith   Michael Shearer
                                                              Chair of Advisory Committee

DEDICATION

I dedicate this thesis to Larry Jr.

BIOGRAPHY

The author, Aaron Bardall, was born in Danville, Pennsylvania on August 31st 1991. One thing led to another, and now he resides in Raleigh, North Carolina. According to many who know him, he is now much smarter and larger than he was when he was born.

ACKNOWLEDGEMENTS

I would like to acknowledge my family, who have always been there for me. They believed in me even when I did not and I wouldn't have gotten this far without them. From apples and oranges math for me and Jared on the swing as kids to being kind, understanding and supportive through every decision I've made, I have become who I am because of them and am grateful for their love and support.

In addition I would like to acknowledge all the educators and advisors, especially my committee, who have helped me gain the knowledge and skills necessary to complete this work. Specifically my advisor Dr. Michael Shearer who has been a pleasure to work with. His support came not only in his vast knowledge and wisdom, but in his kindness and attention to detail. He was very trusting of me from the start and let me work quite independent from his active research but was always available to give suggestions and bounce ideas off of throughout the entirety of this project. He has helped me develop into a mathematician as well as a communicator and I cannot thank him enough.

Alongside Dr. Shearer, Dr. Karen Daniels has been like a second advisor to me throughout my graduate education. I still haven't figured out how she does all that she does while providing expertise and attention for each and every one of her students. She is quick to provide personalized advice from her seemingly endless supply of knowledge and experiences, and I truly believe she would selflessly drop everything at any time to help someone in need.

TABLE OF CONTENTS

LIST OF FIGURES

CHAPTER

1

INTRODUCTION

Elastocapillarity is the study of the influence of capillary forces on elastic materials. Examples include capillary rise between elastic sheets [21], smoothing of features on solid slabs [18, 19] and deformation of soft solids by immersion or resting fluids [4, 6, 19, 25, 41] as well as fluid motion over soft materials [26, 43, 48]. Exploring alternative and novel mechanisms for inducing droplet motion across soft materials is an emerging subject of interest for the soft matter and fluid dynamics communities. These methods rely on physical substrate configurations for which the droplet profile becomes asymmetric, subsequently causing a force imbalance driving the droplet to migrate to a region of lower total energy. Examples of current academic interest include motion induced by gradients in substrate rigidity [8], substrate thickness [43], and substrate pre-strain [7] among others.

Durotaxis, or motion caused by a rigidity gradient, is observed in living cells [31, 43]. In this process, the cells are believed to actively sense and relay changes in stiffness and respond by contracting and altering cellular shape to migrate to regions of higher stiffness. Though in recent experiments [43], migration of inorganic fluid is observed to be driven by a gradient in substrate thickness; a physical surrogate for the bulk elastic modulus. In these experiments, the droplets migrate to thicker, less hard regions of the substrate. This stands at odds with behavior observed by living cells which tend to prefer settling at harder regions of their organic matrix. However, recent computational results have suggested that fluid migration across a true rigidity gradient may as well be biased toward stiffer regions of the substrate [8], and may depend on the balance of interfacial energies at the

fluid-solid-vapor contact line. Further analysis into modes of migration of inorganic fluids may provide insight into the driving mechanisms for organic cells.

Driving mechanisms for droplet motion across rigid surfaces has been extensively studied. Droplet motion induced by periodically patterned surface energies [9, 14], thermal gradients [30], and magnetic fields [12] have been documented to name a few. Like rigid substrates, droplet motion across soft substrates relies on contact angle asymmetry resulting in a force imbalance inducing migration. However, additional factors affecting bulk fluid migration across soft substrates include elastic deformations and resulting elastic energy within the substrate as well as bulk energy dissipation within the substrate. In order to determine conditions for which a fluid droplet will begin to migrate across a soft surface, the deformation and associated elastic energy must be analyzed.

When a fluid droplet rests on a rigid substrate, surface energies γ at the phase interfaces govern the equilibrium contact angle θ_Y of the droplet:

$$\gamma_{sg} - \gamma_{ls} = \gamma_{lg} \cos\theta_Y \tag{1.1}$$

This relationship is widely known as Young's equation, and is the direct result of total surface energy minimization at the phase interfaces. In (1.1), subscripts on surface energy terms γ refer to the associated interface, i.e. γ_{sg} is the surface energy of the solid-gas interface. Young's equation also represents a tangential force balance at the triple point, or contact line. The remaining vertical force caused by the liquid-gas interface of the droplet is assumed to be resolved by the ideal rigid solid substrate for which strains approach zero as stiffness tends to infinity. When the difference in solid surface tensions $\gamma_{sg} - \gamma_{ls}$ is positive, the droplet substrate system is termed hydrophilic, and has an equilibrium Young's angle of $\theta_Y < 90°$, whereas if the difference is negative, the droplet substrate system is hydrophobic with Young's angle $\theta_Y > 90°$.

For soft solids, non-zero deformations influenced by the capillary forces of the droplet occur within the substrate introducing elastic energy into the system. This elastic energy competes with the aforementioned surface energy and determination of the equilibrium contact angle via minimization of total system energy becomes more complex. In addition, surface strains affect the solid surface stresses by the Shuttleworth effect [51, 52]:

$$\Upsilon_{\parallel} = \gamma_{\parallel} + \frac{\partial \gamma_{\parallel}}{\partial \varepsilon} \tag{1.2}$$

where the '$\parallel$' symbol refers to the component of surface stress parallel to the interface. This expression relates surface stresses Υ, which depends on strain ε, to surface energy γ which is a thermody-

2
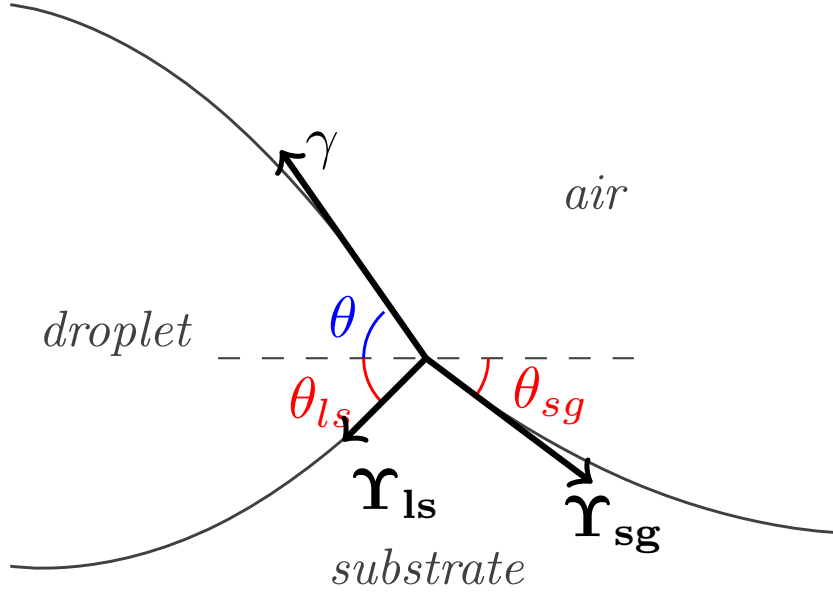
Figure 1.1 Wetting ridge formed by a resting fluid droplet. Solid surface stresses Υ balance surface tension of the contact line γ. Apparent contact angle θ illustrated in blue as the angle the fluid surface forms with the far field horizontal (dashed line), while solid contact angles θ_{ls} and θ_{sg} define respectively the angle of the liquid-solid and solid-gas interfaces form with the far field horizontal.

namic property of the two phases meeting at the interface. Surface energy is defined as the work done to increase the surface area per unit area, while surface stress is defined as the tensile force per unit width of the surface. For incompressible liquids, these two definitions are equivalent as molecules are free to rearrange absent of any solid structure.

The vertical component of force from the liquid-gas interface pulls up on the substrate creating a wetting ridge (Fig. 1.1). This resulting balance is referred to as Neumann's triangle [41, 45], where the solid interfaces now angle downward opposing the upward pull of the droplet edge creating a total force balance at the contact line. Neumann's triangle is expressed mathematically by

$$\vec{\Upsilon}_{sg} + \vec{\Upsilon}_{ls} + \vec{\gamma} = \vec{0} \tag{1.3}$$

where solid surface stress vectors $\vec{\Upsilon}$ balance with the surface tension vector $\vec{\gamma}$ of the droplet edge. The wetting ridge will form at approximately the size of the elastocapillary length scale $L_e = \gamma/E$, where E is the elastic modulus of the solid substrate. With typical liquid surface energies $\gamma \approx 6 \times 10^{-2}$

N/m, we find that micro-scale deformations occur at elastic moduli of order $E = \mathcal{O}(1 - 10 \text{ kPa})$. In [42] it is shown that though deformation is negligible in stiff substrates with elastocapillary length L_e much less than one micrometer ($L_e \ll 1 \ \mu\text{m}$), if the elastocapillary length L_e is larger than the atomic length scale, Neumann's triangle is still formed at the elastocapillary length scale despite negligible deformation at the visible scale.

For droplets of a similar length scale, these deformations are significant enough to alter the apparent contact angle, or angle the droplet edge forms with the far field horizontal plane, of the droplet several degrees from Young's angle θ_Y in (1.1) [41]. While deviation from Young's angle causes total surface energy to increase, deviations that reduce the angle with which the liquid-gas interface meets the solid surface reduces the upward pull of the liquid edge resulting in shallower deformations and strains and thus lower elastic energy. The competition of these two trends generally results in hydrophobic droplet-substrate systems to have equilibrium angles slightly greater than that predicted by (1.1), and similarly results in hydrophilic systems having equilibrium angles slightly less than that predicted by (1.1) [8, 41].

When a contact line at the fluid-solid-vapor interface advances or recedes, there are associated advancing and receding contact angles θ_a and θ_r respectively such that $\theta_r \leq \theta \leq \theta_a$, where θ is the static contact angle of the droplet. These dynamic contact lines exhibit hysteretic behavior, where by adding volume to the droplet, the contact angle will increase to the advancing angle θ_a, then the contact line will advance and settle at an equilibrium value. If the additional liquid is then removed, the contact angle must decrease down to the receding contact angle θ_r before the contact line recedes [1]. These angles can experimentally be found using the tilted plate method, where by resting a droplet on a plate and tilting it to an incline such that the droplet begins to migrate, the contact angles formed at the front and back of the droplet are equivalent to the advancing and receding contact angles respectively [1].

By introducing a gradient in a substrate property such as elastic modulus or surface energy, the apparent contact angle of a resting droplet becomes spatially dependent resulting in contact angle asymmetry. With enough bias in one direction, the force imbalance generated by the asymmetry can overcome pinning forces at the contact line and droplet motion is induced. In experiments by Style and Dufresne [43], by comparing to their contact angle theory to their experimental results they found a contact angle difference of $\Delta\theta = \theta_a - \theta_r \approx 1.8°$ was sufficient for water droplet motion over silicone gel. These results were independent of the droplet size, which is a factor in the equilibrium contact angle of the droplet on a soft surface. This suggests that motion is governed by the relative difference in contact angles as opposed to the absolute advancing and receding angles themselves.

The structure of the thesis is as follows. Chapter 2 contains relevant background information on elastic models and continuum mechanics, as well as the formulation of boundary conditions of a droplet in contact with a free solid surface. These are used to define the model boundary value problem in the form of model equation and shear and normal stress boundary conditions at the solid free surface exposed to the droplet. In addition, a discussion regarding current contact line models is included which is important for the general case of a non-trivial tangential contact line force which is neglected in most models.

Chapters 3 and 4 discuss static models related to the deformation caused by a resting fluid droplet (Ch. 3) or in a partially submerged rod (Ch. 4). Notably in Ch. 3, a necessary boundary condition is introduced to accommodate the general loading required of more recent contact line models. In addition in Ch. 4, the quasi-one dimensional submerged rod geometry is analyzed in connection with the droplet geometry to compare behavior of the contact line force in different geometries. Experimental results are discussed in Ch. 4, highlighting some of the experimental difficulties necessary to overcome in order to determine the nature of the contact line force for the given geometry.

Chapter 5 adapts the two-dimensional deformation model discussed in Chapter 3 to accommodate for gradients in substrate properties, ultimately resulting in contact angle asymmetry. Adopting the assumptions based on results from [43], we make predictions for when droplet motion is induced based on the relative difference in contact angle values. Ultimately it is shown that despite being able to cause asymmetry, a stiffness gradient is unlikely to succeed as the sole factor for inducing droplet motion. However, a gradient in surface energy is a theoretically feasible method for inducing motion over soft substrates.

Chapter 6 discusses methods to predict the resulting speed of droplet motion once sufficiently induced by substrate gradients in Ch. 5. These predictions rely on the balance between system dissipation and rate that energy is released in the system by migration. Here dissipation occurs dominantly in the solid, as opposed to the case of a rigid substrate for which dissipation within the fluid is dominant. This extra resistance introduced by the deformation of the solid and associated energy dissipation slows down the dynamics of droplets over soft solids when compared to motion over rigid surfaces. Concluding remarks and future project directions are then presented in Ch. 7.

CHAPTER

2

BACKGROUND

Here we outline a few topics that will be important throughout the body of the thesis. In §2.1 we establish formalism in linear elasticity which will be used the model the deformation of our solid substrate. In §2.2 the stress boundary conditions that characterize the surface exposed to the droplet, or solid free surface, are derived via an energy minimization argument. Through this derivation, the nature of the contact line force is left ambiguous. A discussion related to current theory presented in [51, 52] as well as experimental conjectures from [28] is presented in §2.3.

2.1   Elasticity and Continuum Mechanics

In a simple uniaxial elastic model depicted in Fig. 2.1, a tensile force applied to a one dimensional elastic beam induces stress within the beam resulting in a lengthening of the beam. Hooke's law relates the applied stress σ to the strain ε by a material parameter referred to as Young's modulus E by the following relationship

$$\sigma = E\varepsilon \tag{2.1}$$

Here, strain is defined as the change in length divided by the original length of the beam ($\varepsilon = \Delta L/L$) and stress is defined as the ratio of applied tensile force over the cross-sectional area of the beam ($\sigma = F/A$). Upon stretching, each point of material is displaced from its original pre-stretched position x to a new position X with the relation $X = x + u(x)$, where u represents the net change in position of the material at original location x. Using this formulation, we can define local strain as
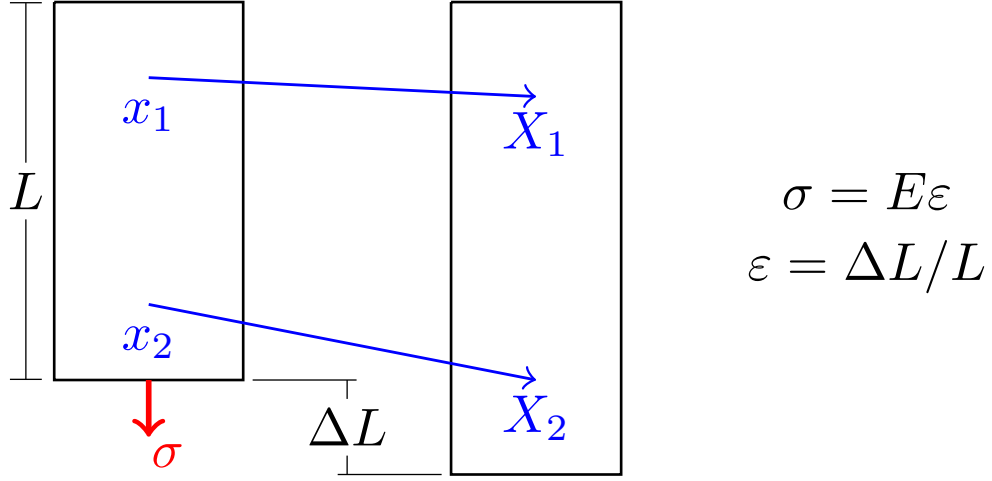
Figure 2.1 Uniaxial loading and deformation of a one-dimensional rod. A stress σ is applied tensively to a rod of length L, extending the length of the rod by a length ΔL. Points x_i are mapped to corresponding resulting locations $X_i = x_i + u(x_i)$ in the deformed state.

the rate of change of u with respect to x:

$$\varepsilon = \frac{d}{dx} u(x) \tag{2.2}$$

Considering a real three dimensional system, the stretching parallel to the applied force would result in the contraction of the material in the perpendicular direction. This introduces another material parameter, the Poisson's ratio ν, which relates the perpendicular strain to the axial strain applied to the rod.

$$\varepsilon_\perp = -\nu\varepsilon_\| \tag{2.3}$$

Combining these for loading in three orthogonal spatial dimensions we obtain a generalized Hooke's law depending on material parameters E and ν:

$$\varepsilon_{11} = \frac{1}{E}\left(\sigma_1 - \nu(\sigma_2 + \sigma_3)\right) \tag{2.4}$$

$$\varepsilon_{22} = \frac{1}{E}\left(\sigma_2 - \nu(\sigma_1 + \sigma_3)\right) \tag{2.5}$$

$$\varepsilon_{33} = \frac{1}{E}\left(\sigma_3 - \nu(\sigma_1 + \sigma_2)\right) \tag{2.6}$$

where strain $\varepsilon_{ii} = \partial_{x_i} u_i$. This can be put into matrix form:

$$\begin{bmatrix} \varepsilon_{11} \\ \varepsilon_{22} \\ \varepsilon_{33} \end{bmatrix} = \frac{1}{E} \begin{bmatrix} 1 & -\nu & -\nu \\ -\nu & 1 & -\nu \\ -\nu & -\nu & 1 \end{bmatrix} \begin{bmatrix} \sigma_1 \\ \sigma_2 \\ \sigma_3 \end{bmatrix} \tag{2.7}$$

which can be inverted to give the principal stresses as a function of strain:

$$\begin{bmatrix} \sigma_1 \\ \sigma_2 \\ \sigma_3 \end{bmatrix} = \frac{E}{(1+\nu)(1-2\nu)} \begin{bmatrix} 1-\nu & \nu & \nu \\ \nu & 1-\nu & \nu \\ \nu & \nu & 1-\nu \end{bmatrix} \begin{bmatrix} \varepsilon_1 \\ \varepsilon_2 \\ \varepsilon_3 \end{bmatrix} \tag{2.8}$$

In addition to normal stress-strain relationships derived above, we also are concerned with shear loading by tangential stresses. For each surface, there are two tangential shear directions as seen in Fig. 2.3 for the six cube faces. We define the shear modulus G by considering a shear stress τ applied to the top of a square in Fig. 2.2, where we define

$$G = \frac{\tau \Delta x}{L} = \tau \tan \phi = \tau \varepsilon_{shear} \tag{2.9}$$

where the strain $\varepsilon_{shear} = \tan \phi = \partial_{x_2} u_1$. By computing the axial strain from the bottom left to top right corners and comparing to the definition of the shear modulus, it can be shown that the two moduli are related by equation $E = 2(1+\nu)G$. Under multi-dimensional loading, shear forces accomplish three types transformations to the geometry of the elastic solid; these being shear, dilation and rotation. Shear is captured by the symmetric portion, while rotation by the antisymmetric portion of the matrix

$$[A]_{ij} = \partial_{x_i} u_j \tag{2.10}$$

and dilation is represented in both symmetric and antisymmetric portions. Using this, we define our symmetric strain tensor to be given by

$$[\varepsilon] = \varepsilon_{ij} = \frac{1}{2}(A + A^T) \quad \Rightarrow \quad \varepsilon_{ij} = \frac{1}{2}(\partial_{x_i} u_j + \partial_{x_j} u_i) \tag{2.11}$$

which is self-consistent with the definition of normal strains in (2.4). Using the solution for the normal strains in (2.8) as well as the stress-strain relationship in (2.9) and by defining $\tau_{ii} = \sigma_i$, we obtain the definition of the stress tensor in terms of strain tensor (2.11):

$$[\tau] = \tau_{ij} \quad \tau_{ij} = \frac{E}{1+\nu}\left[\varepsilon_{ij} + \frac{\nu}{1-2\nu}\delta_{ij}\varepsilon_{kk}\right] \tag{2.12}$$

where δ_{ij} is the Kronecker delta and ε_{kk} is the trace of the strain tensor.
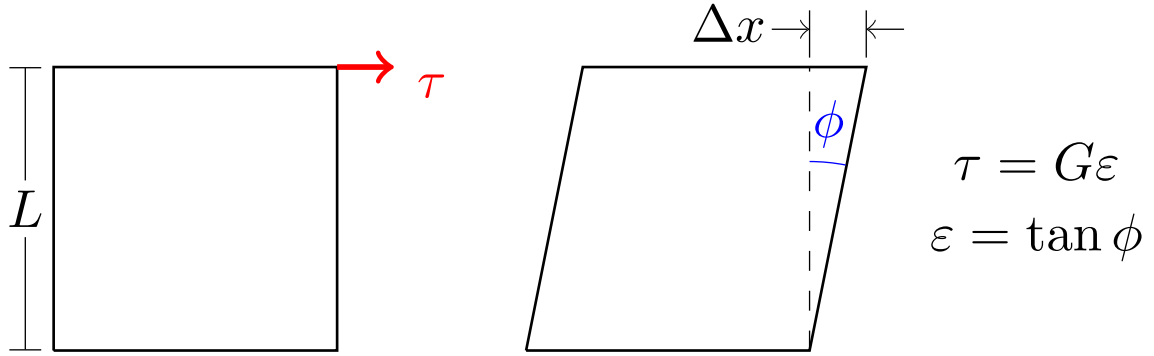
Figure 2.2 Square of elastic material deformed by shear loading. Stress τ applied along top edge while bottom edge is held fixed. The resulting deformation slides the top edge a length Δx and angle ϕ is formed with the vertical dashed line.
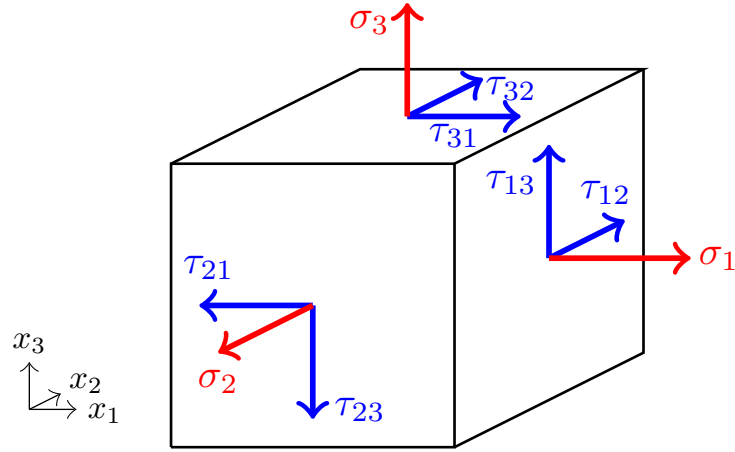
Figure 2.3 Shear (blue) and normal (red) loading on a 3d elastic solid. Positive orientation of shear stresses τ_{ij} shown, corresponding to the orientation of the normal vector to the exposed surface, i.e. τ_{21} oriented in the direction of $-\hat{i}$ is defined positively because outward unit normal vector $-\hat{j}$ opposes the positive x_1 direction, while the opposite is true for τ_{31} on the top face.

In addition to relating parallel and perpendicular normal strains as in (2.3), Poisson's ratio is indicative of the volumetric dilation of an elastic material under applied pressure p. The bulk modulus K of a material, defined as

$$K = -\frac{V}{\Delta V}\Delta p \tag{2.13}$$

quantifies the inverse of the volumetric change of material per change in hydrostatic compression Δp. This tends to infinity for incompressible materials. This modulus can be related to the shear and elastic moduli by relation

$$2(1+\nu)G = E = 3(1-2\nu)K \tag{2.14}$$

illustrating that $\nu = 1/2$ indicates the solid is incompressible. If the Poisson's ratio decreases from $\nu = 1/2$ then the bulk modulus in turn decreases representing a larger change in volume ΔV per incremental loading Δp, or more total solid compression.

In addition, these moduli from (2.14) relate to the Lamé parameters μ and λ from classical mechanics, which are defined as coefficients for components of the stress tensor:

$$\tau_{ij} = 2\mu\varepsilon_{ij} + \lambda\delta_{ij}\varepsilon_{kk} \tag{2.15}$$

where by comparing with (2.12), we see that μ is simply the shear modulus G and $\lambda = 2G\nu/(1-2\nu)$.

Using the derivations from above, we can develop a model describing the motion of a material point in an elastic solid by the applied stresses to the material. The volume specific force balance equation is represented by the sum of forces equation

$$\rho\ddot{\vec{u}} = \nabla\cdot\bar{\tau} + \vec{b} \tag{2.16}$$

where ρ is the mass density, $\vec{u}$ is the relative position vector, or displacement vector and $\vec{b}$ is the specific body force. With droplet size length scales on the order of the elastocapillary length scale $L_e = \gamma/E = \mathcal{O}(10\mu\text{m})$, we find that

$$\|\vec{b}\| \sim \rho g L_e^3 \ll \|\nabla\cdot\tau\| \sim \gamma L_e \tag{2.17}$$

This shows in general that gravitational body forces will compete with surface forces only if $L_e \sim L_c = \sqrt{\gamma/\rho g}$, where L_c is the capillary length scale. Under negligible gravitational influence, we adopt the continuum static equilibrium model to be

$$\nabla\cdot\bar{\tau} = \mathbf{0} \tag{2.18}$$

Using this with the linear elastic strain tensor (2.15), we obtain (letting $\partial_j = \partial_{x_j}$):

$$\nabla \cdot \bar{\tau} = \mathbf{0} \qquad \Rightarrow \qquad \partial_j \tau_{ij} = 0 \qquad (i = 1, 2, 3)$$

where for spatially constant Lamé parameters μ, λ we have that

$$2\mu \partial_j \varepsilon_{ij} + \lambda \partial_i \varepsilon_{jj} = 0 \qquad (i = 1, 2, 3)$$
$$\Rightarrow \mu \partial_j (\partial_i u_j + \partial_j u_i) + \lambda \partial_i (\partial_j u_j) = 0$$
$$\Rightarrow \mu \partial_j^2 u_i + (\lambda + \mu) \partial_i (\partial_j u_j) = 0$$
$$\Rightarrow \mu \Delta \mathbf{u} + (\lambda + \mu) \nabla (\nabla \cdot \mathbf{u}) = \mathbf{0}$$

Where upon substituting in our physical parameters we obtain the Elastostatic Navier equations for static equilibrium of a linearly elastic solid:

$$(1 - 2\nu)\Delta \mathbf{u} + \nabla (\nabla \cdot \mathbf{u}) = \mathbf{0} \tag{2.19}$$

Which will be solved for our specific model in later chapters.

2.2 Free Surface Boundary Conditions

Here we establish appropriate surface stress boundary conditions that reflect the influence of a resting droplet on a deformable elastic substrate. In this section, these boundary conditions will be derived using variational calculus to obtain conditions for a minimum in total system energy, and applied to our models in future chapters.

Following the work of [27], we seek to define the boundary conditions on the free surface as a result of a resting fluid droplet. These boundary conditions will define the shear and normal stresses associated with a resting two-dimensional droplet of radius R on an elastic substrate which undergoes deformation at the free surface with surface displacement vector $\vec{u}(x) = \langle u(x), w(x) \rangle$ containing the horizontal and vertical displacement of the surface. We will first construct the energy functional of the system per unit depth with penalties in the form of Lagrange multiplier constraints that restrict the fluid edge to meet with the solid surface at the contact line as well as enforcing constant cross-sectional area A of the droplet. Then, taking variations with respect to the droplet height $h(x)$, contact line location R and the solid surface profile displacements $u(x)$ and $w(x)$, we define the shear and normal surface stress boundary conditions τ_{xz} and τ_{zz} respectively. Utilizing symmetry, we will perform the analysis on the positive real line and extend our results to the entire real line.

We define our surface energy functional $\mathcal{E}_s$ below:

$$\mathcal{E}_s = \int_0^\infty \gamma_s(x) \left[\sqrt{(1+u')^2 + (w')^2} - 1 \right] dx + \int_0^R \gamma \sqrt{1+(h')^2} \, dx \tag{2.20}$$

where the first integral represents the solid surface energy and the second the energy of the liquid-gas phase. The elastic energy functional $\mathcal{E}_{el}$ is defined as

$$\mathcal{E}_{el} = \frac{1}{2} \iint_\Omega \tau \cdot \varepsilon \, d\Omega \tag{2.21}$$

which, for the purposes of these calculations, is rewritten using Divergence theorem. The inner product of the stress and strain tensors is manipulated as follows:

$$
\begin{aligned}
\tau \cdot \varepsilon &= \langle \varepsilon_{xx}, \varepsilon_{xz} \rangle \cdot \langle \tau_{xx}, \tau_{xz} \rangle + \langle \varepsilon_{xz}, \varepsilon_{zz} \rangle \cdot \langle \tau_{xz}, \tau_{zz} \rangle \\
&= \langle \partial_x u, \frac{1}{2}(\partial_z u + \partial_x w) \rangle \cdot \langle \tau_{xx}, \tau_{xz} \rangle + \langle \frac{1}{2}(\partial_z u + \partial_x w), \partial_z w \rangle \cdot \langle \tau_{xz}, \tau_{zz} \rangle \\
&= \nabla u \cdot \langle \tau_{xx}, \tau_{xz} \rangle + \nabla w \cdot \langle \tau_{xz}, \tau_{zz} \rangle \\
&= \nabla \cdot (u \langle \tau_{xx}, \tau_{xz} \rangle + w \langle \tau_{xz}, \tau_{zz} \rangle)
\end{aligned}
$$

where the last manipulation is a consequence of the equilibrium condition (2.18). Assuming fixed boundary conditions at the substrate boundaries everywhere except the free surface, we obtain a simplified energy functional by Divergence theorem:

$$\mathcal{E}_{el} = \frac{1}{2} \int_0^\infty (u \, \tau_{xz} + w \, \tau_{zz}) \, dx \tag{2.22}$$

Our total energy functional then becomes the sum of the surface and energy functionals as well as Lagrange multiplier constraint enforcing the triple point at the contact line:

$$\mathcal{E}_{tot} = \mathcal{E}_s + \mathcal{E}_{el} + \lambda_{cl}\big(h(R) - w(R)\big) + \lambda_A \left[A - \int_0^R \big(h(x) - w(x)\big) \, dx \right] \tag{2.23}$$

We take the first variation of the total energy with respect to droplet profile height $h(x)$:

$$
\begin{aligned}
\delta\mathcal{E}_{tot} &= \lim_{\epsilon \to 0} \frac{\mathcal{E}_{tot}\big(h(x) + \epsilon \delta h(x)\big) - \mathcal{E}_{tot}\big(h(x)\big)}{\epsilon} \\
&= \lim_{\epsilon \to 0} \frac{1}{\epsilon} \int_0^R \gamma \left(\sqrt{1+(h'+\epsilon\delta h')^2} - \sqrt{1+(h')^2} \right) dx + \lambda_{cl}\delta h(R) - \lambda_A \int_0^R \delta h(x) \, dx \\
&= \lim_{\epsilon \to 0} \frac{1}{\epsilon} \int_0^R \gamma \left(\sqrt{1+(h')^2 + 2\epsilon h' \delta h'} - \sqrt{1+(h')^2} \right) dx + \lambda_{cl}\delta h(R) - \lambda_A \int_0^R \delta h(x) \, dx
\end{aligned}
$$

where using approximation $\sqrt{a+\delta} - \sqrt{a} \approx \delta/2\sqrt{a}$ for $a \gg \delta$, we get

$$\delta\mathcal{E}_{tot} = \int_0^R \frac{h'(x)}{\sqrt{1+(h')^2}}\delta h'(x)\,dx + \lambda_{cl}\delta h(R) - \lambda_A \int_0^R \delta h(x)\,dx$$

$$= \left(\lambda_{cl} - \frac{h'(R)}{\sqrt{1+(h'(R))^2}}\right)\delta h(R) + \int_0^R \left(-\gamma\kappa - \lambda_A\right)\delta h(x)\,dx$$

where κ is the curvature of the liquid surface $h(x)$. By definition of Laplace pressure, $P = -\gamma\kappa$ we obtain $\lambda_A = P$. It also follows that $\lambda_{cl} = \gamma\sin\theta$ where θ is the angle the liquid edge forms with the horizontal. Following a similar procedure, taking the variation with respect to vertical displacement $w(x)$, we obtain

$$\delta\mathcal{E}_{tot} = \left(\gamma_{ls}\sin\theta_{ls} + \gamma_{sg}\sin\theta_{sg} - \lambda_{cl}\right)\delta w(R) + \int_0^\infty \left(\tau_{zz} - \gamma_s(x)(\vec{\kappa}_s \cdot \hat{e}_z)\right)\delta w(x)\,dx$$

$$+\lambda_A \int_0^R \delta w(x)\,dx$$

where θ_{ls} and θ_{sg} are the angle the solid-liquid phase and the liquid-gas phase forms with the horizontal depicted in Fig. 1.1 and $\vec{\kappa}_s$ is the curvature of the solid surface. Taking results from the variation with respect to droplet profile h, we obtain vertical contact line force balance equation

$$\gamma\sin\theta = \gamma_{ls}\sin\theta_{ls} + \gamma_{sg}\sin\theta_{sg} \tag{2.24}$$

as well as definition of normal stress at the free surface τ_{zz} for locations away from the contact line:

$$\tau_{zz}(x) = -PH(R-|x|) + \gamma_s(x)(\vec{\kappa}_s \cdot \hat{e}_z)$$

Incorporating the point loading force of the contact line, we obtain the free surface normal stress definition by variational principles:

$$\tau_{zz}(x) = \gamma\sin\theta\left(\delta(x+R) + \delta(x-R)\right) - PH(R-|x|) + \gamma_s(x)(\vec{\kappa}_s(x) \cdot \hat{e}_z) \tag{2.25}$$

Similarly, by taking variations with respect to contact line location R and horizontal displacement $u(x)$, we obtain horizontal contact line force balance equation

$$\gamma\cos\theta + \gamma_{ls}\cos\theta_{ls} = \gamma_{sg}\cos\theta_{sg} \tag{2.26}$$

and the free surface shear stress definition by variational principles:

$$\tau_{xz}(x) = f_t\left(\delta(x+R) - \delta(x-R)\right) + \gamma_s(x)(\vec{\kappa}_s(x) \cdot \hat{e}_x) \tag{2.27}$$

13

where f_t is a general tangential point loading at the contact line location, discussed in §2.3. These stresses (2.25) and (2.27) define the free surface boundary conditions representing the minimum total energy of the resting droplet system. Solving the general model (2.18) in coordination with these boundary conditions will yield the deformation and associated stresses and strains of the elastic substrate. In addition, the vertical and horizontal force balances at the contact line (2.24) and (2.26) derived by variational principles validate the Neumman triangle assumption (1.3) in the absence of the Shuttleworth effect (1.2).

We observe some key features in the stress boundary conditions (2.25) and (2.27), including point loadings at the contact lines at $x = \pm R$, as well as a pressure distribution under the droplet generated by the curvature of the droplet free surface. These stresses are a result of the fluid droplet itself, while the remaining terms involving the solid free surface curvature are a result of the curvature of the deformed substrate. As will be seen later in Ch. 3, under the assumption of point loading at the contact line, these traction stresses are crucial to ensure bounded displacements at the contact line location. Though point loading is physically unrealistic, the length scale over which the contact line applies stress is the atomic length scale of the fluid, which is several orders of magnitude less than the elastocapillary length scale $L_e = \gamma/E$. Though modeling the contact line as some small, but finite size would alleviate the need to have the solid traction stresses present to resolve unbounded displacements, our further work will use the point loading model for simplicity, and the inclusion of the solid traction in general only adds to the accuracy of the model.

2.3   Contact Line Models

When considering a fluid contact line with associated surface stress γ pulling on the surface of an elastic solid, the strength and orientation of the contact line force determines the resulting deformation of the solid as a result of the contact line. While for an angle θ between the surface normal vector and the vector parallel to the contact line, $f_n = \gamma \sin \theta$ is well agreed upon as the normal component of force at the contact line, the tangential component f_t has been a topic of debate and interest among soft matter researchers [28, 51, 52].

For droplets resting on rigid substrates exhibiting zero strain, Young's equation (1.1) defines an *a priori* force tangential balance. However, Shuttleworth's equation (1.2) predicts that the solid surface stresses are dependent on the strain. So for elastic substrates which deform under loading, (1.1) no longer guarantees a force balance in the tangential direction for droplets with contact angle equivalent to Young's contact angle θ_Y.

While if the strain dependence of the Shuttleworth equation (1.2) is negligible, we would still expect a

14

horizontal force balance making the tangential force $f_t = 0$, work by [18,52] utilizing thermodynamic arguments predict a tangential contact line force equivalent to

$$f_t = (\Upsilon_{ls} - \Upsilon_{sg}) - (\gamma_{ls} - \gamma_{sg}) = \frac{1-2\nu}{1-\nu}\gamma(1+\cos\theta_Y) \tag{2.28}$$

which depends on the liquid surface tension γ as well as the Poisson's ratio ν. Notably this prediction still yields a tangential force of zero for incompressible substrates, though predicts very large tangential loading for low values of ν, or highly compressible materials. This aspect of the predicted formula (2.28) makes it challenging to experimentally test using soft gel materials for which reside near the incompressible limit.

An alternative geometry, where an elastic rod is partially submerged inside a fluid bath, was studied by [28]. In this experiment, small beads were embedded inside the elastic rod to measure the strain both above and below the contact line. Using the method of virtual work akin to the principal governing the Wilhelmy plate method for determining surface tensions of liquid, [28] emperically predict a contact line force

$$f_t = \gamma(1+\cos\theta) \tag{2.29}$$

biased toward the liquid, where θ is the angle formed by the liquid meniscus. This equation is similar to that predicted by [52] in (2.28) without the dependence on the compressibility of the elastic solid.

Using substrate deformation data from [41] for a static droplet, the three contact line models (2.28), (2.29) and $f_t = 0$ were examined by [6]. In their simulations, it was shown that (2.29) was an unrealistic model for a droplet, but did not disprove its application to alternative geometries such as the rod geometry the force model was originally posed in. Furthermore, with the limitation of the data being from a nearly incompressible substrate, it was unsuccessful in providing insight on whether (2.28) or $f_t = 0$ is the correct model for the droplet geometry.

Furthermore, the previous tangential force models are all designed for fluids which obey Young's equation (1.1). Under deviation of the contact angle θ from θ_Y we theoretically predict a contact line force of

$$f_t = \gamma(\cos\theta - \cos\theta_Y) \tag{2.30}$$

In order to consider these non-trivial contact line models, adjustments must be made to existing solution methods in [6,41] to rectify the displacement singularity occurring due to the point loading approximation. Under linearized curvature, the curvature vector is approximated as completely normal to the surface which is sufficient to remove the vertical displacement singularity, though is not sufficient to remove a horizontal displacement singularity introduced by a non-zero tangential

15

force $f_t \neq 0$. We will show in Ch. 3 that including a horizontal component of the curvature vector, the horizontal (2D) or radial (3D) displacement singularity is also removed at the contact line.

CHAPTER

3

SYMMETRIC DEFORMATION MODEL

The work presented in §3.1-3.4 of this chapter is taken directly from or paraphrased from previously published work [4] by myself as well as Dr. Michael Shearer and Dr. Karen Daniels.

On a sufficiently-soft substrate, a resting fluid droplet will cause significant deformation of the substrate. This deformation is driven by a combination of capillary forces at the contact line and the fluid pressure at the solid surface. These forces are balanced at the surface by the solid traction stress induced by the substrate deformation. Young's Law, which predicts the equilibrium contact angle of the droplet, also indicates an *a priori* radial force balance for rigid substrates, but not necessarily for soft substrates which deform under loading. It remains an open question whether the contact line transmits a non-zero force tangent to the substrate surface in addition to the conventional normal (vertical) force.

In §3.2 we present an analytic Fourier transform solution technique that includes general interfacial energy conditions which govern the contact angle of a 2D droplet, for which we solve for the droplet profile and fluid pressure in §3.1. Importantly, we find in §3.3 performing a truncation error analysis on the inverse transform solutions to the model in §3.2 that in order to avoid a displacement singularity at the contact line under a non-zero tangential contact line force, it is necessary to include a previously-neglected horizontal traction boundary condition. These results are then extended to the neutral wetting case in §3.5 of the 3D droplet utilizing a Hankel transform, where similar results

are found regarding the displacement singularity at the contact line. Both two dimensional results and three dimensional axisymmetric results are explored in §3.4 as well as §3.6.

3.1 2D Droplet Shape and Fluid Pressure Under Gravity

The fluid pressure Π and droplet shape are influenced only slightly by the deformation in the substrate, which is localized near the contact line. In this section, we determine the pressure and droplet shape by assuming the substrate is rigid and flat. With this assumption, we determine the relationship between the fluid pressure Π and droplet radius R, and their dependence on surface tension and gravity. We use this then to define the pressure under the droplet used in our boundary value problem investigated in §3.2 and subsequent solutions.

Gravity influences droplets when the droplet size exceeds the capillary length scale: $R > L_c$. For small droplets ($R/L_c \ll 1$), the droplet surface takes on a circular shape (spherical in three dimensions). For large droplets, gravity dominates and the droplet flattens out except near the contact line as seen in Fig. 3.2.

The height $f(x)$ of the droplet free surface above the substrate is determined by minimizing the total energy. The differential gravitational and surface energies are given respectively by

$$dU_g(x) = \frac{\rho g f(x)^2}{2} \, dx$$

and

$$dU_s(x) = \gamma \sqrt{1 + f'(x)^2} \, dx.$$

We then consider the energy cost functional $\mathscr{E}$ representing the energy of half the droplet ($0 \le x \le R$), imposing a constant area A representing the amount of fluid in the droplet:

$$\mathscr{E} = \int \left[dU_g + dU_s - \lambda_A dA \right] + \lambda_{cl} f(R) = \int_0^R \left[\rho g f(x)^2/2 + \gamma \sqrt{1 + f'(x)^2} - \lambda f(x) \right] dx + \lambda_{cl} f(R) \quad (3.1)$$

where λ_A is a Lagrange multiplier enforcing constant droplet area and λ_{cl} is a Lagrange multiplier enforcing $f(R) = 0$. Computing the first variation with respect to droplet height, we get

$$
\begin{aligned}
\delta \mathscr{E} &= \lim_{\epsilon \to 0} \frac{\mathscr{E}(f + \epsilon \delta f) - \mathscr{E}(f)}{\epsilon} \\
&= \lim_{\epsilon \to 0} \frac{1}{\epsilon} \int_0^R \frac{\rho g}{2} \big((f + \epsilon \delta f)^2 - f^2\big) + \gamma \big(\sqrt{1 + (f' + \epsilon \delta f')^2} - \sqrt{1 + (f')^2}\big) \, dx \\
&\quad - \lambda_A \int_0^R \delta f \, dx + \lambda_{cl} \delta f(R) \\
&= \int_0^R \delta f \big[\rho g f - \lambda_A\big] \, dx + \int_0^R \gamma \frac{f' \delta f'}{\sqrt{1 + (f')^2}} \, dx + \lambda_{cl} \delta f(R) \\
&= \int_0^R \delta f \big[\rho g f - \gamma \frac{f''}{(1 + (f')^2)^{3/2}} - \lambda_A\big] \, dx + \delta f(R)\big(\lambda_{cl} - \gamma \sin \alpha\big).
\end{aligned}
$$

Setting the variation $\delta \mathscr{E}$ to zero we obtain the differential equation

$$
\lambda_A = \rho g f(x) - \gamma \frac{f''(x)}{(1 + f'(x)^2)^{3/2}} = \Pi_{\text{hydrostatic}} + \Pi_{\text{Laplace}} = \Pi. \tag{3.2}
$$

From this we find that the value of the Lagrange multiplier λ_A is equal to the sum of hydrostatic and Laplace pressures generated by weight and curvature respectively, while λ_{cl} is equal to the vertical contact line force $\gamma \sin \alpha$. This gives us that the fluid pressure Π at the solid surface is constant. In small gravity $R/L_c \ll 1$, the equation (3.2) gives us that the curvature of the droplet free surface $f(x)$ is constant, showing that for small droplets the liquid free surface forms a circular cap. It can be shown geometrically that for a circular cap forming a contact angle α with the horizontal and projected radius R, the area of the circular cap is equal to $A = R^2(\alpha \csc^2 \alpha - \cot \alpha)$. Using the low gravity approximation, we integrate (3.2) from 0 to R to obtain

$$
\int_0^R \Pi \, dx = \Pi R = \int_0^R \Big[\rho g f(x) - \gamma \frac{f''(x)}{(1 + f'(x)^2)^{3/2}}\Big] \, dx = \rho g \frac{A}{2} + \gamma \sin \alpha,
$$

giving us an asymptotic approximation of non-dimensionalized pressure for low gravity droplets:

$$
\frac{\Pi}{\rho g L_c} \sim \sin \alpha \frac{L_c}{R} + \frac{\alpha \csc^2 \alpha - \cot \alpha}{2} \frac{R}{L_c} \qquad \frac{R}{L_c} \ll 1. \tag{3.3}
$$

The differential equation (3.2) is solved more generally by utilizing the chain rule and imposing boundary conditions $f'(0) = f(R) = 0$, $f'(R) = -\tan \alpha$ to provide an implicit solution for the droplet

19

shape in terms of the non-dimensionalized pressure $\Pi/\rho g L_c$ and contact angle α:

$$\text{Let } f'(x) = v(f) \qquad \Rightarrow f''(x) = v'(f)f'(x) = v'v$$

$$\Rightarrow \rho g f - \gamma \frac{v'v}{(1+v^2)^{3/2}} = \Pi$$

$$\Rightarrow \int \gamma \frac{v \, dv}{(1+v^2)^{3/2}} = \int (\rho g f - \Pi) \, df$$

$$\Rightarrow -\gamma \frac{1}{\sqrt{1+v^2}} = \rho g \frac{f^2}{2} - \Pi f + C$$

where at $f = 0$ we have $f'(f=0) = -\tan\alpha$ giving $C = -\gamma\cos\alpha$. Solving for $v = f'(f)$ we get

$$v = \frac{df}{dx} = -\sqrt{\left(\frac{1}{2}\left(\frac{f}{L_c}\right)^2 - \frac{\Pi}{\rho g L_c}\frac{f}{L_c} - \cos\alpha\right)^{-2} - 1} \tag{3.4}$$

$$\Rightarrow \int_0^{f(x)} \frac{df}{\sqrt{\left(\frac{1}{2}\left(\frac{f}{L_c}\right)^2 - \frac{\Pi}{\rho g L_c}\frac{f}{L_c} - \cos\alpha\right)^{-2} - 1}} = \int_R^x -1 \, dx,$$

where after nondimensionalization by L_c we obtain

$$\frac{R-x}{L_c} = \int_0^{f(x)/L_c} \frac{d\xi}{\sqrt{\left(\frac{1}{2}\xi^2 - \frac{\Pi}{\rho g L_c}\xi - \cos\alpha\right)^{-2} - 1}}. \tag{3.5}$$

Enforcing boundary condition $f'(x=0) = 0$, we know that (3.4) is equal to zero at $x = 0$. From this we obtain condition

$$\frac{f(0)}{L_c} = \frac{\Pi}{\rho g L_c} - \sqrt{\left(\frac{\Pi}{\rho g L_c}\right)^2 - 2\left(1 - \cos\alpha\right)}. \tag{3.6}$$

Using upper bound from (3.6), we search for nondimensionalized pressure $\Pi/\rho g L_c$ which satisfies (3.5) at $x = 0$ using a bisection algorithm, then with the pressure defined we solve (3.5) implicitly for droplet profile $f(x)$. In Fig. 3.1, we plot the curve of such values for a contact angle of $\alpha = 90°$ obtained numerically from (3.5), (3.6) for specified R/L_c.

We further manipulate (3.5) to analytically solve for the asymptotic behavior of the nondimensionalized pressure $p = \Pi/\rho g L_c$ as $R/L_c \to \infty$. Enforcing that (3.6) is real valued, we define the minimum pressure to be $p_0 = 2\sin(\alpha/2)$ for which we obtain $\cos\alpha = 1 - p_0^2/2$. Under change of
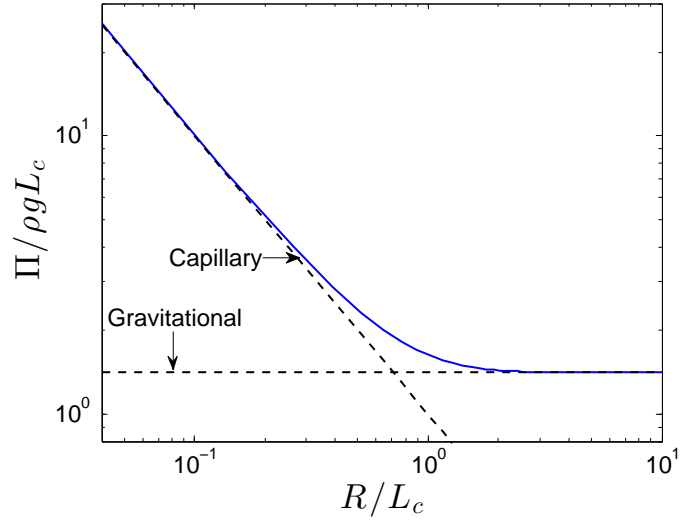
Figure 3.1 Nondimensionalized fluid pressure $\Pi/\rho g L_c$ as a function of droplet radius for contact angle $\alpha = 90°$. The capillary limit represents the Laplace pressure which decays inversely to the droplet radius R, while the gravitational limit represents the hydrostatic pressure limit generated by the fluid with depth equivalent to the equilibrium height of the fluid droplet as $R \to \infty$.

variables $\eta = p - \xi$ we obtain

$$
\begin{aligned}
\frac{R}{L_c}(p) &= \int_0^{p-\sqrt{p^2-p_0^2}} \frac{d\xi}{\sqrt{\left(\frac{1}{2}\xi^2 - p\xi - \cos\alpha\right)^{-2} - 1}} \\
&= \int_p^{\sqrt{p^2-p_0^2}} \frac{-d\eta}{\sqrt{\left(\frac{1}{2}(p-\eta)^2 - p(p-\eta) + \frac{1}{2}p_0^2 - 1\right)^{-2} - 1}} \\
&= \int_{\sqrt{p^2-p_0^2}}^{p} \frac{1 - \frac{1}{2}\left(\eta^2 - (p^2 - p_0^2)\right)}{\sqrt{1 - \left(\frac{1}{2}\left(\eta^2 - (p^2 - p_0^2)\right) - 1\right)^2}} \, d\eta
\end{aligned}
$$

Expanding the integrand about $\zeta = \sqrt{\eta^2 - (p^2 - p_0^2)}$, the integrand becomes

$$
\frac{1 - \frac{1}{2}\left(\eta^2 - (p^2 - p_0^2)\right)}{\sqrt{1 - \left(\frac{1}{2}\left(\eta^2 - (p^2 - p_0^2)\right) - 1\right)^2}} = \frac{1 - \frac{1}{2}\zeta^2}{\sqrt{1 - \left(\frac{1}{2}\zeta^2 - 1\right)^2}} = \frac{1 - \frac{1}{2}\zeta^2}{\zeta\sqrt{1 - \frac{1}{4}\zeta^2}} \sim \frac{1}{\zeta} + \mathcal{O}(\zeta)
$$

And we obtain estimate as $R/L_c \to \infty$:

$$
\frac{R}{L_c} \sim \int_{\sqrt{p^2-p_0^2}}^{p} \frac{d\eta}{\sqrt{\eta^2 - (p^2 - p_0^2)}} = \cosh^{-1}\frac{p}{\sqrt{p^2 - p_0^2}}
\tag{3.7}
$$

21

Solving algebraically for p we obtain

$$\cosh^2 \frac{R}{L_c} \sim \frac{p^2}{p^2 - p_0^2} \quad \Rightarrow \quad p \sim p_0 \coth \frac{R}{L_c}$$

as $R/L_c \to \infty$ and we get

$$\frac{\Pi}{\rho g L_c} \sim 2\sin(\alpha/2)\coth \frac{R}{L_c} \qquad \frac{R}{L_c} \gg 1. \tag{3.8}$$

which asymptotes at $\Pi/\rho g L_c = 2\sin(\alpha/2)$.

Fig. 3.1 illustrates that for droplets with projected radius $R \lesssim 0.3 L_c$, the Laplace pressure dominates hydrostatic pressure and a circular cap approximation for the droplet shape is accurate. Past the transition region $2L_c \lesssim R$, we observe the hydrostatic pressure dominate the Laplace pressure and the droplet shape flattens out to $f(x) \approx f(0) = 2L_c \sin(\alpha/2)$ everywhere except in the vicinity of the contact line. While for small droplets, the large Laplace pressure is significant in influencing deformation, as droplet size increases this pressure reduces in magnitude and negligibly affects the deformation.

Plotted in Fig. 3.2 is the droplet shape profile for a contact angle of $\alpha = 4\pi/9$ radians for droplets of various sizes. We see that for small droplets $R/L_c \ll 1$ that the droplet profile closely matches that of the circular cap approximation and begins to deviate from this limit as the ratio R/L_c approaches and exceeds 1.

3.2   2D Deformation Model

We consider the two dimensional droplet outlined in §3.1 resting on a solid substrate, depicted schematically in Fig. 3.3, with width $2R$ and resting on the free upper surface of a solid elastic substrate. In the reference configuration, the substrate is taken to be fixed on the bottom surface $z = 0$, to have infinite extent, and to have constant thickness h. The elastic modulus of the substrate is denoted by E, and Poisson's ratio by ν. The contact line introduces a vertical force $\gamma \sin\alpha$ and a tangential force f_t which cause significant deformation in a neighborhood of the contact line, depicted in Fig. 3.3(c). The fluid pressure Π in the droplet acts at the substrate interface to compress the substrate below. In this chapter, we quantify these influences and describe the deformation of the substrate.

The model depends largely on the formulation of boundary conditions at the free surface of the substrate outlined in §2.2. This is composed of two parts; the section under the droplet forming
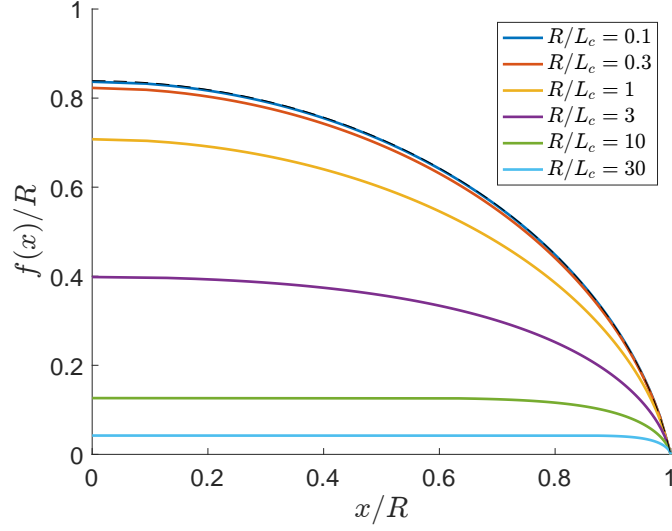
Figure 3.2 Various size droplet profiles for contact angle $\alpha = 4\pi/9$ rad. As the size of the droplet R/L_c increases, we see the droplet profile transition from the circular cap approximation (black dotted line) to a flat profile shape in the extreme limit of R/L_c.

the liquid solid interface and the solid-gas interface between the substrate and air. The effect of the droplet is expressed solely through the surface stress at the substrate surface and through the pressure Π. Once these are quantified, the droplet is effectively removed from the subsequent analysis.

To determine the shape of the substrate free surface, we formulate a boundary value problem for the elastic displacement within the substrate. It is convenient to use Eulerian coordinates (x, z), shown in Fig. 3.3. in which the substrate free boundary is located at $z = h$ in the reference configuration. The displacement $\vec{u}$ of the substrate is then represented in two components by

$$\vec{u}(x, z) = u(x, z)\hat{e}_x + w(x, z)\hat{e}_z, \quad -\infty < x < \infty, \ 0 < z < h, \tag{3.9}$$

where $\hat{e}_x$, $\hat{e}_z$ are unit vectors in the coordinate directions. The displacement is defined relative to the reference configuration, mapping the reference configuration to the static deformed substrate configuration:

$$(x, z) \mapsto (x + u(x, z), z + w(x, z)).$$

The elastostatic Navier equations

$$(1 - 2\nu)\Delta\vec{u} + \nabla(\nabla \cdot \vec{u}) = \mathbf{0}, \tag{3.10}$$

23
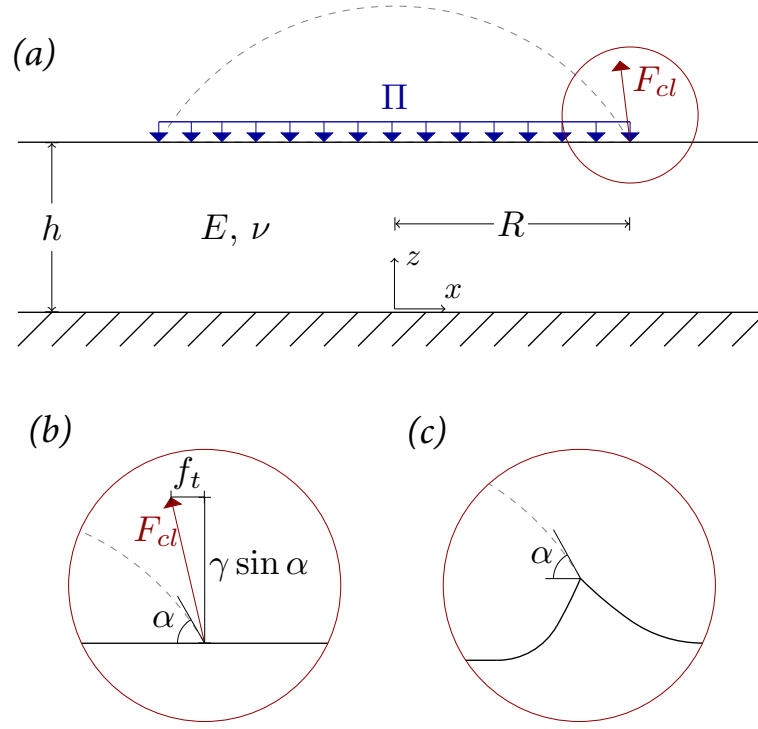
Figure 3.3 Schematic of geometry and forces. (a) Reference configuration showing horizontal substrate layer and droplet surface (dashed). Fluid pressure Π and contact line force F_{cl} act on the solid substrate with elastic modulus E and Poisson ratio ν. (b) Blow-up at the contact line showing the effective contact angle α, and contact line force F_{cl} that includes a non-zero tangential stress component f_t. (c) Deformation of the substrate free surface caused by capillary forces.

derived in Ch. 2 express force balance within the substrate. Here ν is the Poisson ratio of the substrate, where incompressible solids have a Poisson ratio of $\nu = 1/2$. In two dimensions, the strain ε and stress τ are represented by 2×2 matrices with components,

$$\varepsilon_{ij} = \frac{1}{2}\Big[\frac{\partial u_i}{\partial x_j} + \frac{\partial u_j}{\partial x_i}\Big] \tag{3.11}$$

and

$$\tau_{ij} = \frac{E}{1+\nu}\Big[\varepsilon_{ij} + \frac{\nu}{1-2\nu}\delta_{ij}\big(\varepsilon_{11} + \varepsilon_{22}\big)\Big] \tag{3.12}$$

where (u_1, u_2) correspond to displacements (u, w) and spatial variables $(x_1, x_2) = (x, z)$. In these tensors, E represents the elastic modulus of the substrate and δ_{ij} is the Kronecker delta.

Fixed boundary conditions are set at the solid surface $z = 0$, where displacement is assumed to be zero:

$$(u, w)|_{z=0} = (0, 0). \tag{3.13}$$

The effect of the droplet on the substrate is quantified by defining the shear stress τ_{xz} and normal stress τ_{zz} at the free surface $z = h$ derived in Ch. 2:

$$\tau_{xz}|_{z=h} = f_t\big(\delta(x + R) - \delta(x - R)\big) + \Upsilon(x)\big(\vec{\kappa}_s(x) \cdot \hat{e}_x\big) \tag{3.14}$$

$$\tau_{zz}|_{z=h} = \gamma \sin\alpha\big(\delta(x + R) + \delta(x - R)\big) - \Pi H(R - |x|) + \Upsilon(x)\big(\vec{\kappa}_s(x) \cdot \hat{e}_z\big) \tag{3.15}$$

where f_t is the tangential point loading at the contact line, $\gamma \sin\alpha$ the normal point loading at the contact line, Π the pressure distribution calculated in the previous section, $\Upsilon(x)$ being the solid surface stress, $\vec{\kappa}_s(x)$ the curvature of the solid surface, and $\delta(x)$ and $H(x)$ being the Dirac delta and Heaviside distributions respectively. We assume that the contact angle α is equivalent to the equilibrium Young's angle θ_Y.

By considering the general curvature vector instead of just the linearized vertical component, as done in previous work [6, 19, 41], we will show that the strain is bounded at the contact line in the horizontal as well as the vertical directions under a general contact line force. The solid surface stress is represented as the piecewise constant function

$$\Upsilon(x) = \Upsilon_{sg} + \Delta\Upsilon H(R - |x|), \qquad \text{with} \qquad \Delta\Upsilon = \Upsilon_{ls} - \Upsilon_{sg}. \tag{3.16}$$

The vector $\vec{r}(x) = \langle x + u, w + h \rangle|_{z=h}$ parameterizes the substrate free surface. Then the curvature vector is given as

$$\vec{\kappa}_s(x) = \frac{(1 + \partial_x u)\partial_{xx} w - \partial_{xx} u \partial_x w}{\big((1 + \partial_x u)^2 + (\partial_x w)^2\big)^2}\big((-\partial_x w)\hat{e}_x + (1 + \partial_x u)\hat{e}_z\big)\big|_{z=h}. \tag{3.17}$$

The conventional model assumes no tangential contact line force ($f_t = 0$). In this case, which simplifies the model, there is a bounded solution at the contact line. The inclusion of an approximation to the horizontal component of curvature in (3.14), (3.15) is expected to improve the fidelity of the solution by reconciling for the previously neglected horizontal traction force. In the general model ($f_t \neq 0$), the inclusion of the horizontal curvature approximation ensures a bounded solution, which otherwise would experience a logarithmic singularity at the contact line. In the generalized model, this tangential contact line force f_t arises due to the difference between surface stress and surface energy, and in general is represented as $f_t = (\Upsilon_{ls} - \Upsilon_{sg}) - (\gamma_{ls} - \gamma_{sg})$. Here we will consider both the

conventional model as well as the form proposed by [51, 52] discussed in Ch. 2:

$$f_t = \frac{1-2\nu}{1-\nu}\gamma(1+\cos\alpha), \tag{3.18}$$

It is useful to express the displacement vector $\vec{u}(x,z)$ in terms of a potential function Ψ. To do this, we define a Galerkin vector $\mathbf{G} = \Psi(x,z)\hat{e}_z$ [6, 39], and define

$$\vec{u}(x,z) = 2(1-\nu)\Delta\mathbf{G} - \nabla(\nabla \cdot \mathbf{G}). \tag{3.19}$$

By manipulating (3.19) and substituting into the Elastostatic Navier equations (3.10) we obtain:

$$\vec{u} = \langle -\partial_{xz}\Psi, 2(1-\nu)(\partial_{xx}\Psi + \partial_{zz}\Psi) - \partial_{zz}\Psi \rangle$$
$$= \langle -\partial_{xz}\Psi, 2(1-\nu)\partial_{xx}\Psi + (1-2\nu)\partial_{zz}\Psi \rangle$$

$$\Rightarrow \Delta\vec{u} = \langle -\partial_{xxxz}\Psi - \partial_{xzzz}\Psi, 2(1-\nu)\partial_{xxxx}\Psi + (3-4\nu)\partial_{xxzz}\Psi + (1-2\nu)\partial_{zzzz}\Psi \rangle$$

and

$$\nabla(\nabla \cdot \vec{u}) = (1-2\nu)\nabla(\partial_{xxz}\Psi + \partial_{zzz}\Psi) = (1-2\nu)\langle \partial_{xxxz}\Psi + \partial_{xzzz}\Psi, \partial_{xxzz}\Psi + \partial_{zzzz}\Psi \rangle$$

which gives us by plugging in to the elastostatic Navier equations

$$\Rightarrow (1-2\nu)\Delta\vec{u} + \nabla(\nabla \cdot \vec{u}) = (1-2\nu)\langle 0, 2(1-\nu)\big(\partial_{xxxx}\Psi + 2\partial_{xxzz}\Psi + \partial_{zzzz}\Psi\big)\rangle = \langle 0, 0 \rangle$$

From this we obtain that the potential is biharmonic:

$$\Delta^2\Psi(x,z) = 0 \tag{3.20}$$

We then obtain displacements and stresses in terms of potential function Ψ:

$$u = -\partial_{xz}\Psi, \tag{3.21a}$$

$$w = 2(1-\nu)\partial_{xx}\Psi + (1-2\nu)\partial_{zz}\Psi, \tag{3.21b}$$

$$\tau_{xz} = \frac{E}{1+\nu}((1-\nu)\partial_{xxx}\Psi - \nu\partial_{xzz}\Psi), \tag{3.21c}$$

$$\tau_{zz} = \frac{E}{1+\nu}((2-\nu)\partial_{xxz}\Psi + (1-\nu)\partial_{zzz}\Psi). \tag{3.21d}$$

One advantage of this potential function Ψ is that its definition allows for direct calculations involving incompressible solids where the Poisson's ratio $\nu = 1/2$, which is a good approximation for nearly incompressible soft materials such as PDMS or hydrogels. Using the definitions (3.21) it is shown that the apparent singularity in the stress tensor (3.12) is resolved in the incompressible limit where

we see the trace of the strain tensor is proportional to denominator $(1-2\nu)$:

$$\varepsilon_{kk} = \varepsilon_{xx} + \varepsilon_{zz} = \partial_x u + \partial_z w = (1-2\nu)\partial_z \Delta \Psi$$

and we obtain stress tensor

$$\tau_{ij} = \frac{E}{1+\nu}\big[\varepsilon_{ij} + \nu\partial_z \Delta\Psi \delta_{ij}\big].$$

We then manipulate the biharmonic equation (3.20) using a Fourier transform and obtain a system of equations to solve for the transformed potential. The Fourier transform is conducive to the cartesian coordinate representation of our two dimensional droplet, whereas a Hankel transform is appropriate in axisymmetric coordinates for the three dimensional droplet [6] and will be discussed later in §3.5. The surface displacements are recovered by truncating the inverse transform at a large wave number S. The asymptotic behavior of the error in this approximation show that the displacement singularity is completely regularized when using both traction boundary conditions.

In this chapter, we define the Fourier Transform pair for a function $f(x,z)$:

$$\mathscr{F}\big[f(x,z)\big] = \hat{f}(s,z) = \frac{1}{\sqrt{2\pi}} \int_{-\infty}^{\infty} f(x,z)e^{isx}dx,$$

$$f(x,z) = \mathscr{F}^{-1}\big[\hat{f}(s,z)\big] = \frac{1}{\sqrt{2\pi}} \int_{-\infty}^{\infty} \hat{f}(s,z)e^{-isx}ds \qquad (3.22)$$

where s is the wavenumber. This transform has derivative property $\mathscr{F}[f'(x)] = -is\hat{f}(s)$. Applying the forward transform (3.22) to the biharmonic potential equation (3.20), we obtain

$$\mathscr{F}\big[\Delta\Psi(x,z)\big] = \mathscr{F}\big[\partial_{xxxx}\Psi + 2\partial_{xxzz}\Psi + \partial_{zzzz}\Psi\big]$$
$$= (-is)^4\hat{\Psi} + (-is)^2\partial_{zz}\hat{\Psi} + \partial_{zzzz}\hat{\Psi}$$
$$= \left(\frac{d^4}{dz^4} - 2s^2\frac{d^2}{dz^2} + s^4\right)\hat{\Psi}$$
$$= \left(\frac{d^2}{dz^2} - s^2\right)^2 \hat{\Psi} = 0$$

which has general solution for the transformed potential:

$$\hat{\Psi}(s,z) = \big(A(s) + szB(s)\big)\cosh(sz) + \big(C(s) + szD(s)\big)\sinh(sz). \qquad (3.23)$$

Where $A(s)$, $B(s)$, $C(s)$ and $D(s)$ are Fourier coefficients to be determined by the boundary conditions (3.13) at $z = 0$ and stress boundary conditions (3.14), (3.15). Applying the fixed boundary

27

conditions (3.13), we calculate relationships between these Fourier coefficients:

$$u(x,0)=0 \Rightarrow \mathscr{F}\big[u(x,0)\big]=0$$
$$\Rightarrow \mathscr{F}\big[-\partial_{xz}\Psi(x,0)\big]=0$$
$$\Rightarrow is\partial_z\hat{\Psi}(s,0)=0$$
$$\Rightarrow is^2\Big[\big(A(s)+szB(s)+D(s)\big)\sinh(sz)+\big(C(s)+szD(s)+B(s)\big)\cosh(sz)\Big]_{z=0}=0$$
$$\Rightarrow is^2\big(C(s)+B(s)\big)=0$$
$$\Rightarrow B(s)=-C(s)$$

and

$$w(x,0)=0 \Rightarrow \mathscr{F}\big[w(x,0)\big]=0$$
$$\Rightarrow \mathscr{F}\big[2(1-\nu)\partial_{xx}\Psi(x,0)+(1-2\nu)\partial_{zz}\Psi(x,0)\big]=0$$
$$\Rightarrow -2(1-\nu)s^2\hat{\Psi}(s,0)+(1-2\nu)\partial_{zz}\hat{\Psi}(s,0)=0$$
$$\Rightarrow -2(1-\nu)s^2\Big[\big(A(s)+szB(s)\big)\cosh(sz)+\big(C(s)+szD(s)\big)\sinh(sz)\Big]_{z=0}+$$
$$(1-2\nu)s^2\Big[\big(A(s)+szB(s)+2D(s)\big)\cosh(sz)+\big(C(s)+szD(s)+2B(s)\big)\sinh(sz)\Big]_{z=0}=0$$
$$\Rightarrow -2(1-\nu)s^2A(s)+(1-2\nu)s^2\big(A(s)+2D(s)\big)=0$$
$$\Rightarrow s^2\big(-A(s)+2(1-2\nu)D(s)\big)=0$$
$$\Rightarrow A(s)=2(1-2\nu)D(s)$$

These expressions are substituted into (3.23) where the transformed potential $\hat{\Psi}$ is now an expression involving two unknown Fourier coefficients $C(s)$ and $D(s)$. After nondimensionalizing lengths x and z such that $x=\pm1$ corresponds to the contact line location and $z=\tilde{h}=h/R$ is the substrate free surface, Fourier coefficients $C(s)$ and $D(s)$ are determined from the two stress boundary conditions (3.14), (3.15) as follows. The convolution identity $\mathscr{F}\big[f(x)g(x)\big]=\mathscr{F}\big[f(x)\big]*\mathscr{F}\big[g(x)\big]/\sqrt{2\pi}$ is used throughout.

Transforming the shear stress boundary condition (3.14) we obtain

$$\mathscr{F}\big[\tau_{xz}(x,h)\big]=\mathscr{F}\Big[\frac{f_t}{R}\big(\delta(x+1)-\delta(x-1)\big)\Big]+\mathscr{F}\big[\Upsilon(x)\vec{\kappa}_s(x)\cdot\hat{e}_x\big]$$
$$=\frac{f_t}{R}\mathscr{F}\big[\big(\delta(x+1)-\delta(x-1)\big)\big]+\Upsilon_{sg}\mathscr{F}\big[\kappa_s(x)\cdot\hat{e}_x\big]+\frac{\Delta\Upsilon}{\sqrt{2\pi}}\mathscr{F}\big[H(1-|x|)\big]*\mathscr{F}\big[\kappa_s(x)\cdot\hat{e}_x\big],$$

and transforming the normal stress boundary condition (3.15) we obtain

$$\mathscr{F}\big[\tau_{xz}(x,h)\big] = \mathscr{F}\Big[\frac{\gamma\sin\alpha}{R}\big(\delta(x+1)+\delta(x-1)\big)-\Pi H(1-|x|)\Big]+\mathscr{F}\big[\Upsilon(x)\vec{\kappa}_s(x)\cdot\hat{e}_z\big]$$

$$= \frac{\gamma\sin\alpha}{R}\mathscr{F}\big[\big(\delta(x+1)+\delta(x-1)\big)\big]-\Pi\mathscr{F}\big[H(1-|x|)\big]+\Upsilon_{sg}\mathscr{F}\big[\kappa_s(x)\cdot\hat{e}_z\big]$$

$$+\frac{\Delta\Upsilon}{\sqrt{2\pi}}\mathscr{F}\big[H(1-|x|)\big]*\mathscr{F}\big[\kappa_s(x)\cdot\hat{e}_z\big].$$

We define from the shear stress equation

$$iM(s) = \frac{f_t}{R}\mathscr{F}\big[\big(\delta(x+1)-\delta(x-1)\big)\big]$$

$$= \frac{f_t}{\sqrt{2\pi}R}\int_{-\infty}^{\infty}\big(\delta(x+1)-\delta(x-1)\big)e^{isx}\,dx$$

$$= \frac{f_t}{\sqrt{2\pi}R}\big(e^{-is}-e^{is}\big)=-f_t\frac{2i}{\sqrt{2\pi}R}\sin s,$$

and from the normal stress equation

$$N(s) = \frac{\gamma\sin\alpha}{R}\mathscr{F}\big[\big(\delta(x+1)+\delta(x-1)\big)\big]-\Pi\mathscr{F}\big[H(1-|x|)\big]$$

$$= \frac{\gamma\sin\alpha}{\sqrt{2\pi}R}\int_{-\infty}^{\infty}\big(\delta(x+1)-\delta(x-1)\big)e^{isx}\,dx-\frac{\Pi}{\sqrt{2\pi}}\int_{-1}^{1}e^{isx}\,dx$$

$$= \frac{\gamma\sin\alpha}{\sqrt{2\pi}R}\big(e^{-is}+e^{is}\big)-\frac{\Pi}{\sqrt{2\pi}}\frac{e^{isx}}{is}\Big|_{-1}^{1}=\frac{2}{\sqrt{2\pi}}\Big(\frac{\gamma\sin\alpha}{R}\cos s-\Pi\frac{\sin s}{s}\Big).$$

From this we obtain equations which constrain coefficients $C(s)$, $D(s)$ (present in stress and displacement transforms):

$$-i\Big(\hat{\tau}_{xz}|_{z=\bar{h}}-\Upsilon_{sg}\mathscr{F}\big[\vec{\kappa}_s(x)\cdot\hat{e}_x\big]-\frac{\Delta\Upsilon}{\pi}\frac{\sin s}{s}*\mathscr{F}\big[\vec{\kappa}_s(x)\cdot\hat{e}_x\big]\Big)=M(s) \tag{3.24}$$

$$\Big(\hat{\tau}_{zz}|_{z=\bar{h}}-\Upsilon_{sg}\mathscr{F}\big[\vec{\kappa}_s(x)\cdot\hat{e}_z\big]-\frac{\Delta\Upsilon}{\pi}\frac{\sin s}{s}*\mathscr{F}\big[\vec{\kappa}_s(x)\cdot\hat{e}_z\big]\Big)=N(s) \tag{3.25}$$

While elasticity dominates the small wave number behavior of the displacements u and w in Fourier space, the traction stress generated by the geometry of the deformed substrate surface determines the decay of these transformed displacements for large wave numbers. Including this traction stress is sufficient to influence the decay of these transformed displacements in Fourier space, thereby eliminating the strain singularity at the contact line [19]. The transformed terms in the curvature approximation (3.17) determine the dominant component of the transformed displacements $\hat{u}$ and $\hat{w}$ as wave number $s\to\infty$. The surface traction force $\Upsilon(x)\vec{\kappa}_s(x)$ is estimated using the following

approximation which is justified later in §3.3:

$$\Upsilon(x)\vec{\kappa}_s(x) \approx k^2 \frac{\Upsilon(x)}{R^2}\partial_{xx}u|_{z=\tilde{h}}\ \hat{e}_x + \frac{\Upsilon(x)}{R^2}\partial_{xx}w|_{z=\tilde{h}}\ \hat{e}_z. \tag{3.26}$$

These terms are evaluated at the free surface $z = \tilde{h}$ and k is the characteristic slope of the vertical displacement near the contact line. For our simulations we define k to be the average magnitude of the rate of change of the vertical deformation w at the contact line, given by

$$k = \frac{1}{2R}\Big(\lim_{x\to 1^-}|\partial_x w(x,\tilde{h})| + \lim_{x\to 1^+}|\partial_x w(x,\tilde{h})|\Big). \tag{3.27}$$

Though the quantities in (3.27) are *a priori* unknown, we estimate k using a method similar to a predictor-corrector procedure. We first set $k = 0$ and calculate the derivative of the vertical displacement on both sides of the contact line providing a k value from (3.27). We then recalculate the displacement field observing that the vertical displacement is largely independent of k.

Previous work [6, 19, 41] has included the same vertical traction stress given by the second term in (3.26), but neglected the horizontal component (first term). We find that the inclusion of the first term is sufficient to obtain bounded horizontal deformation at the contact line under the generalized contact line model, justified later in the chapter in §3.3. From the traction stress estimate (3.26), we calculate the transform estimates

$$\mathscr{F}(\vec{\kappa}_s\cdot\hat{e}_x) \approx -k^2\frac{s^2}{R^2}\hat{u}|_{z=\tilde{h}}, \qquad \mathscr{F}(\vec{\kappa}_s\cdot\hat{e}_z) \approx -\frac{s^2}{R^2}\hat{w}|_{z=\tilde{h}}. \tag{3.28}$$

We then apply the Fourier transform to the definitions of displacement u and w and stresses τ_{xz} and τ_{zz} from (3.21). Transforming horizontal displacement (3.21a) we obtain:

$$\begin{aligned}
\hat{u}(s,z) &= \frac{1}{R^2}\mathscr{F}\big[-\partial_{xz}\Psi\big] \\
&= -(-is)\frac{1}{R^2}\partial_z\hat{\Psi} \\
&= is^2\frac{1}{R^2}\Big[C(s)\big(-sz\sinh(sz)\big) + D(s)\big((3-4\nu)\sinh(sz) + sz\cosh(sz)\big)\Big],
\end{aligned}$$

and vertical displacement (3.21b) we obtain:

$$
\begin{aligned}
\hat{w}(s,z) &= \frac{1}{R^2}\mathscr{F}\big[2(1-\nu)\partial_{xx}\Psi+(1-2\nu)\partial_{zz}\Psi\big]\\
&= \frac{1}{R^2}\big(2(1-\nu)(-is)^2\hat{\Psi}+(1-2\nu)\partial_{zz}\hat{\Psi}\big)\\
&= s^2\frac{1}{R^2}\Big[-2(1-\nu)\big(C(s)\big(\sinh(sz)-sz\cosh(sz)\big)+D(s)\big(2(1-2\nu)\cosh(sz)+sz\sinh(sz)\big)\big)\\
&\quad +(1-2\nu)\big(C(s)\big(-\sinh(sz)-sz\cosh(sz)\big)+D(s)\big(4(1-\nu)\cosh(sz)+sz\sinh(sz)\big)\big)\Big]\\
&= s^2\frac{1}{R^2}\Big[C(s)\big(-(3-4\nu)\sinh(sz)+sz\cosh(sz)\big)+D(s)\big(-sz\sinh(sz)\big)\Big].
\end{aligned}
$$

Transformed shear stress (3.21c) in terms of transformed potential $\hat{\Psi}$:

$$
\begin{aligned}
\hat{\tau}_{xz}(s,z) &= \frac{E}{(1+\nu)R^3}\mathscr{F}\big[(1-\nu)\partial_{xxx}\Psi-\nu\partial_{xzz}\Psi\big]\\
&= \frac{E}{(1+\nu)R^3}\big[(1-\nu)(-is)^3\hat{\Psi}-\nu(-is)\partial_{zz}\hat{\Psi}\big]\\
&= is^3\frac{E}{(1+\nu)R^3}\Big[(1-\nu)\big(C(s)\big(\sinh(sz)-sz\cosh(sz)\big)\\
&\quad +D(s)\big(2(1-2\nu)\cosh(sz)+sz\sinh(sz)\big)\big)+\nu\big(C(s)\big(-\sinh(sz)-sz\cosh(sz)\big)\\
&\quad +D(s)\big(4(1-\nu)\cosh(sz)+sz\sinh(sz)\big)\big)\Big]\\
&= is^3\frac{E}{(1+\nu)R^3}\Big[C(s)\big((1-2\nu)\sinh(sz)-sz\cosh(sz)\big)\\
&\quad +D(s)\big(2(1-\nu)\cosh(sz)+sz\sinh(sz)\big)\Big].
\end{aligned}
$$

and normal stress (3.21d) in terms of transformed potential $\hat{\Psi}$:

$$
\begin{aligned}
\hat{\tau}_{zz}(s,z) &= \frac{E}{(1+\nu)R^3}\mathscr{F}\big[(2-\nu)\partial_{xxz}\Psi+(1-\nu)\partial_{zzz}\Psi\big]\\
&= \frac{E}{(1+\nu)R^3}\big[(2-\nu)(-is)^2\partial_z\hat{\Psi}+(1-\nu)\partial_{zzz}\hat{\Psi}\big]\\
&= s^3\frac{E}{(1+\nu)R^3}\Big[(2-\nu)\big(C(s)\big(sz\sinh(sz)\big)+D(s)\big(-(3-4\nu)\sinh(sz)-sz\cosh(sz)\big)\big)\\
&\quad +(1-\nu)\big(C(s)\big(-2\cosh(sz)-sz\sinh(sz)\big)+D(s)\big((5-4\nu)\sinh(sz)+sz\cosh(sz)\big)\big)\Big]\\
&= s^3\frac{E}{(1+\nu)R^3}\Big[C(s)\big(-2(1-\nu)\cosh(sz)+sz\sinh(sz)\big)\\
&\quad +D(s)\big(-(1-2\nu)\sinh(sz)-sz\cosh(sz)\big)\Big].
\end{aligned}
$$

These expressions above allow us to rewrite (3.24), (3.25) as linear equations to solve for Fourier coefficients $C(s)$ and $D(s)$, and thus fully define our transformed displacements to obtain displace-

ments, strains and stresses in physical space. Substituting the definitions calculated above evaluated at the surface $z = \tilde{h}$ and transformed surface curvature transforms (3.28) into (3.24), (3.25), we obtain integral equations:

$$s^2 C(s)\beta_1(s) + s^2 D(s)\beta_2(s) + \frac{\Delta\Upsilon}{\pi}\frac{k^2}{R^2}\int_{-\infty}^{\infty}\frac{\sin(t-s)}{t-s}t^2\big(-i\hat{u}(t,\tilde{h})\big)dt = M(s), \qquad (3.29)$$

$$s^2 C(s)\mu_1(s) + s^2 D(s)\mu_2(s) + \frac{\Delta\Upsilon}{\pi}\frac{1}{R^2}\int_{-\infty}^{\infty}\frac{\sin(t-s)}{t-s}t^2\big(\hat{w}(t,\tilde{h})\big)dt = N(s). \qquad (3.30)$$

where $\beta_{1,2}$ and $\mu_{1,2}$ are defined as

$$\beta_1(s) = s\Big(\frac{(1-2\nu)E}{(1+\nu)R^3} - \frac{k^2 s^2 \tilde{h}\Upsilon_{sg}}{R^4}\Big)\sinh(s\tilde{h}) + s^2\Big(\frac{-E\tilde{h}}{(1+\nu)R^3}\Big)\cosh(s\tilde{h}) \qquad (3.31\text{a})$$

$$\beta_2(s) = s^2\Big(\frac{E\tilde{h}}{(1+\nu)R^3} + \frac{k^2(3-4\nu)\Upsilon_{sg}}{R^4}\Big)\sinh(s\tilde{h}) \qquad (3.31\text{b})$$

$$+ s\Big(\frac{2(1-\nu)E}{(1+\nu)R^3} + \frac{k^2 s^2 \tilde{h}\Upsilon_{sg}}{R^4}\Big)\cosh(s\tilde{h}) \qquad (3.31\text{c})$$

$$\mu_1(s) = s^2\Big(\frac{E\tilde{h}}{(1+\nu)R^3} - \frac{(3-4\nu)\Upsilon_{sg}}{R^4}\Big)\sinh(s\tilde{h}) + s\Big(\frac{-2(1-\nu)E}{(1+\nu)R^3} + \frac{s^2 \tilde{h}\Upsilon_{sg}}{R^4}\Big)\cosh(s\tilde{h}) \qquad (3.31\text{d})$$

$$\mu_2(s) = s\Big(\frac{-(1-2\nu)E}{(1+\nu)R^3} - \frac{s^2 \tilde{h}\Upsilon_{sg}}{R^4}\Big)\sinh(s\tilde{h}) + s^2\Big(\frac{-E\tilde{h}}{(1+\nu)R^3}\Big)\cosh(s\tilde{h}) \qquad (3.31\text{e})$$

Note that the system of equations (3.29) and (3.30) are algebraic for constant surface stress $\Delta\Upsilon = 0$, and coefficients C and D are simply solved by inverting the linear system. Since the displacement functions $u(x,z)$ and $w(x,z)$ are second order derivatives of the potential function $\psi(x,z)$, it follows that their transform variables $\hat{u}$ and $\hat{w}$ will be proportional to s^2. Therefore, rather than approximating the Fourier coefficients C and D directly, we instead approximate $s^2 C$ and $s^2 D$. Once the Fourier coefficients are calculated, the displacement field is obtained by approximating the inverse transforms:

$$u(x,z) = \sqrt{\frac{2}{\pi}}\int_0^{\infty}\big(-i\hat{u}(s,z)\big)\sin(sx)\,ds$$

$$= \sqrt{\frac{2}{\pi}}\frac{1}{R^2}\int_0^{\infty}\Big[s^2 C(s)\big(-sz\sinh(sz)\big) + s^2 D(s)\big((3-4\nu)\sinh(sz) + sz\cosh(sz)\big)\Big]\sin(sx)\,ds \quad (3.32)$$

$$w(x,z) = \sqrt{\frac{2}{\pi}}\int_0^{\infty}\big(\hat{w}(s,z)\big)\cos(sx)\,ds$$

$$= \sqrt{\frac{2}{\pi}}\frac{1}{R^2}\int_0^{\infty}\Big[s^2 C(s)\big(sz\cosh(sz) - (3-4\nu)\sinh(sz)\big) - s^2 D(s)\big(sz\sinh(sz)\big)\Big]\cos(sx)\,ds \quad (3.33)$$

These specify the displacement for $x \geq 0$, then odd and even extensions to $x < 0$ are taken for u and w respectively. We solve equations (3.29), (3.30) approximately by taking an asymptotic expansion of the transformed displacements $\hat{u}$, $\hat{w}$ as well as Fourier coefficients $C(s)$, $D(s)$:

$$\hat{u}(s,z) \;=\; \hat{u}_0(s,z) + \epsilon\,\hat{u}_1(s,z) + \epsilon^2\,\hat{u}_2(s,z) + \cdots, \tag{3.34a}$$

$$\hat{w}(s,z) \;=\; \hat{w}_0(s,z) + \epsilon\,\hat{w}_1(s,z) + \epsilon^2\,\hat{w}_2(s,z) + \cdots, \tag{3.34b}$$

$$C(s) \;=\; C_0(s) + \epsilon\,C_1(s) + \epsilon^2 C_2(s) + \cdots, \tag{3.34c}$$

$$D(s) \;=\; D_0(s) + \epsilon\,D_1(s) + \epsilon^2 D_2(s) + \cdots, \tag{3.34d}$$

where we set the small parameter $\epsilon = \Delta\Upsilon/\Upsilon_{sg}$ by assuming the change in surface energy is small. Under this expansion, we first solve for the zeroth order transformed displacements $\hat{u}_0$, $\hat{w}_0$ and use them to solve for the first order correction to the Fourier coefficients C, D. The system of equations to obtain the first order correction is given by:

$$s^2 C_0(s)\beta_1(s) + s^2 D_0(s)\beta_2(s) \;=\; M(s), \tag{3.35a}$$

$$s^2 C_0(s)\mu_1(s) + s^2 D_0(s)\mu_2(s) \;=\; N(s), \tag{3.35b}$$

and

$$s^2 C_1(s)\beta_1(s) + s^2 D_1(s)\beta_2(s) \;=\; -\frac{\Upsilon_{sg}}{\pi}\frac{k^2}{R^2}\int_{-\infty}^{\infty}\frac{\sin(t-s)}{t-s}t^2\big(-i\,\hat{u}_0(t,\tilde{h})\big)\,dt, \tag{3.36a}$$

$$s^2 C_1(s)\mu_1(s) + s^2 D_1(s)\mu_2(s) \;=\; -\frac{\Upsilon_{sg}}{\pi}\frac{1}{R^2}\int_{-\infty}^{\infty}\frac{\sin(t-s)}{t-s}t^2\big(\hat{w}_0(t,\tilde{h})\big)\,dt, \tag{3.36b}$$

The zeroth order coefficients $s^2 C_0$, $s^2 D_0$ are algebraically obtained from (3.35) and used to define the zeroth order transforms $\hat{u}_0$, $\hat{w}_0$. The limits of the transformed displacements for large s values are given by

$$\hat{u}_0(s,\tilde{h}) \sim \;\; i K_u s^{-2}\sin s \;\; = \hat{u}_{lim}(s), \tag{3.37a}$$

$$\hat{w}_0(s,\tilde{h}) \sim \;\; K_w s^{-2}\cos s \;\; = \hat{w}_{lim}(s), \tag{3.37b}$$

where constants $K_{u,w}$ are given by:

$$K_u \;=\; \frac{-2R f_t}{\sqrt{2\pi}\,k^2\Upsilon_{sg}} \tag{3.38a}$$

$$K_w \;=\; \frac{2R\gamma\sin\alpha}{\sqrt{2\pi}\,\Upsilon_{sg}} \tag{3.38b}$$

33

Where these coefficients are derived in §3.3. Substituting these limits into the right side of the equations in (3.36) in place of the zeroth order transforms, we calculate the principal values by the Cauchy Integral theorem (all integrals below are Principal Values):

$$\int_{-\infty}^{\infty} \frac{\sin(t-s)}{t-s} t^2 \left(-i\,\hat{u}_{lim}(t) \right) dt = \int_{-\infty}^{\infty} K_u \frac{\sin(t-s)\sin t}{t-s} dt$$

$$= -\frac{K_u}{2} \int_{-\infty}^{\infty} \frac{\cos(2t-s) - \cos(s)}{t-s} dt$$

$$= -\frac{K_u}{2} \int_{-\infty}^{\infty} \frac{\cos(2t-s)}{t-s} dt = -\frac{K_u}{2} \int_{-\infty}^{\infty} \frac{\cos\xi}{\xi-s} d\xi$$

$$= -\frac{K_u}{2} \Re\left(\pi i \operatorname{Res}\left[\frac{e^{i\xi}}{\xi-s}, \xi = s \right] \right) = \frac{\pi}{2} K_u \sin s,$$

and

$$\int_{-\infty}^{\infty} \frac{\sin(t-s)}{t-s} t^2 \left(\hat{w}_{lim}(t) \right) dt = \int_{-\infty}^{\infty} K_w \frac{\sin(t-s)\cos t}{t-s} dt$$

$$= \frac{K_w}{2} \int_{-\infty}^{\infty} \frac{\sin(2t-s) - \sin(s)}{t-s} dt$$

$$= \frac{K_w}{2} \int_{-\infty}^{\infty} \frac{\sin(2t-s)}{t-s} dt = \frac{K_w}{2} \int_{-\infty}^{\infty} \frac{\sin\xi}{\xi-s} d\xi$$

$$= \frac{K_w}{2} \Im\left(\pi i \operatorname{Res}\left[\frac{e^{i\xi}}{\xi-s}, \xi = s \right] \right) = \frac{\pi}{2} K_w \cos s.$$

To calculate the integrals in (3.36), the principal values above are added to the integral of the difference between the transformed displacements and their limits given in (3.37), calculated numerically over the interval $|s| \le \bar{S}$. This provides accurate results for the integrals in (3.36) over the interval $|s| \le S < \bar{S}$, where S is the wave number cap for our numerical calculations. With the solutions to (3.36), the first order transformed displacements $\hat{u}_1$, $\hat{w}_1$ are obtained and used to calculate the displacements $u(x,z)$, $w(x,z)$ by use of (3.32) and (3.33) using approximate Fourier coefficients $C(s) \approx C_0(s) + \epsilon C_1(s)$, $D(s) \approx D_0(s) + \epsilon D_1(s)$.

The solution method outlined in this section will be used in §3.4 to solve for the substrate profile for the different contact line models discussed in §2.3. Before this, we outline in §3.3 the error analysis which illustrates the sufficiency of the general linearized curvature transforms (3.28) in regulating both vertical and horizontal displacements at the contact line location.

3.3 Error Analysis of 2D Deformation Model

Here we outline the procedure to obtain the generalized linear curvature transforms (3.28). Ultimately in this section we will show that for the derived curvature approximations that the truncation error is bounded and approaches zero, giving us accurate results for finite wavenumber cap S. This is done by taking asymptotic estimates of the displacement transforms $\hat{u}$ and $\hat{w}$ at large wavenumbers s and performing a simplified truncated integral to estimate the truncation error for a given wavenumber cap S. These results are then verified by comparing to numerical results generated by the procedure outlined in §3.2 by adjusting the wavenumber cap S over several simulations. This is visually represented in Fig. 3.4.

For the error analysis to follow in this section, we assume that the solid surface stress is constant ($\Upsilon(x) = \Upsilon$). Taking constant surface stress reduces (3.24) and (3.25) from §3.2 to

$$-i\left(\hat{\tau}_{xz}|_{z=\tilde{h}} - \Upsilon \mathscr{F}\left[\vec{\kappa}_s(x) \cdot \hat{e}_x\right]\right) = M(s) \tag{3.39}$$

$$\left(\hat{\tau}_{zz}|_{z=\tilde{h}} - \Upsilon \mathscr{F}\left[\vec{\kappa}_s(x) \cdot \hat{e}_z\right]\right) = N(s) \tag{3.40}$$

Agreeing with Bostwick *et al* [6] regarding the vertical component of curvature, we take

$$\mathscr{F}\left[\vec{\kappa}_s \cdot \hat{e}_z\right] \approx \frac{1}{R^2}\mathscr{F}(\partial_{xx}w) = -\frac{s^2}{R^2}\hat{w} \tag{3.41}$$

We then take approximation from (3.17):

$$\vec{\kappa}_s(x) \cdot \hat{e}_x \approx \frac{1}{R^4}(\partial_x w)^2 \partial_{xx}u - \frac{1}{R^3}\partial_x w \partial_{xx}w$$

by assuming small strains $\partial_x u \ll 1$, $\partial_x w \ll 1$ similar as for the vertical curvature approximation.

$$\mathscr{F}\left[\vec{\kappa}_s \cdot \hat{e}_x\right] = \frac{1}{R^4} \frac{1}{\sqrt{2\pi}} \int_{-\infty}^{\infty} (\partial_x w)^2 \partial_{xx} u\, e^{isx} dx - \frac{1}{R^3} \frac{1}{\sqrt{2\pi}} \int_{-\infty}^{\infty} \frac{1}{2} \partial_x w \partial_{xx} w\, e^{isx} dx$$

$$= \frac{1}{R^4} \frac{1}{\sqrt{2\pi}} \int_{-\infty}^{\infty} (\partial_x w)^2 \partial_{xx} u\, e^{isx} dx - \frac{1}{R^3} \frac{1}{\sqrt{2\pi}} \int_{-\infty}^{\infty} \frac{1}{2} \partial_x \big((\partial_x w)^2\big) e^{isx} dx$$

$$= \frac{1}{R^4} \frac{1}{\sqrt{2\pi}} \int_{-\infty}^{\infty} (\partial_x w)^2 \partial_{xx} u\, e^{isx} dx + \frac{1}{R^3} \frac{is}{\sqrt{2\pi}} \int_{-\infty}^{\infty} \frac{1}{2} (\partial_x w)^2 e^{isx} dx$$

$$= \frac{1}{R^4} \frac{1}{\sqrt{2\pi}} \int_{-\infty}^{\infty} (\partial_x w)^2 \partial_{xx} u\, e^{isx} dx - \frac{1}{R^3} \frac{is}{\sqrt{2\pi}} \int_{-\infty}^{\infty} \frac{1}{2} w (is \partial_x w + \partial_{xx} w) e^{isx} dx$$

$$= \frac{1}{R^4} \frac{1}{\sqrt{2\pi}} \int_{-\infty}^{\infty} (\partial_x w)^2 \partial_{xx} u\, e^{isx} dx + \frac{s^2}{R^3} \frac{1}{\sqrt{2\pi}} \int_{-\infty}^{\infty} \frac{1}{4} \partial_x \big((w)^2\big) e^{isx} dx$$

$$\qquad - \frac{is}{R^3} \int_{-\infty}^{\infty} \frac{1}{2} w \partial_{xx} w\, e^{isx} dx$$

$$= \frac{1}{R^4} \frac{1}{\sqrt{2\pi}} \int_{-\infty}^{\infty} (\partial_x w)^2 \partial_{xx} u\, e^{isx} dx - \frac{is}{R^3} \Big[\frac{1}{4} s^2 \frac{1}{\sqrt{2\pi}} \int_{-\infty}^{\infty} (w)^2 e^{isx} dx$$

$$\qquad + \frac{1}{2} \frac{1}{\sqrt{2\pi}} \int_{-\infty}^{\infty} w \partial_{xx} w\, e^{isx} dx \Big]$$

$$= \frac{1}{R^2} \mathscr{F}\Big[\frac{(\partial_x w)^2}{R^2} \partial_{xx} u \Big] - i \frac{s}{R^3} \Big(s^2 \mathscr{F}\Big[\frac{(w)^2}{4} \Big] + \mathscr{F}\Big[\frac{w \partial_{xx} w}{2} \Big] \Big)$$

Further approximation is then taken to continue the analysis. The second derivatives $\partial_{xx} u$ and $\partial_{xx} w$ are assumed large in magnitude near the contact line where the wetting ridge is located, but by comparison are negligibly small elsewhere in the spatial domain. Therefore the largest component of the spatial integrals takes place near the contact line. This allows us to take characteristic slope near the contact line k^2 in place of $(\partial_x w)^2/R^2$ in the first integral and characteristic peak vertical displacement U in place of w in the third integral. Though the second integral contains a w^2 term, we take one w as the characteristic displacement U and leave the other in the transform. Again we justify this linearization for approximation since the vertical displacement field is largest at the contact line and close to zero elsewhere in the spatial domain. With these approximations, we obtain an estimate in terms of transformed displacements $\hat{u}$ and $\hat{w}$:

$$\mathscr{F}\left[\vec{\kappa}_s \cdot \hat{e}_x\right] \approx \frac{k^2}{R^2} \mathscr{F}(\partial_{xx} u) - i U \frac{s}{R^3} \Big[\frac{1}{4} s^2 \mathscr{F}(w) + \frac{1}{2} \mathscr{F}(\partial_{xx} w) \Big]$$

$$= -k^2 \frac{s^2}{R^2} \hat{u} - i U \frac{s^3}{R^3} \Big[\frac{1}{4} \hat{w} - \frac{1}{2} \hat{w} \Big]$$

$$= -k^2 \frac{s^2}{R^2} \hat{u} + i \frac{U}{4} \frac{s^3}{R^3} \hat{w} \qquad\qquad (3.42)$$

With the curvature transform approximations (3.42) and (3.41), the system of equations given by (3.39), (3.40) by definitions of transformed displacements and stresses to transformed potential $\hat{\Psi}$ (3.23) becomes

$$s^2 C(s)\beta_1^*(s) + s^2 D(s)\beta_2^*(s) = M(s) \tag{3.43}$$

$$s^2 C(s)\mu_1(s) + s^2 D(s)\mu_2(s) = N(s) \tag{3.44}$$

where

$$\beta_1^*(s) = \left(\frac{(1-2\nu)Es}{(1+\nu)R^3} + U\frac{(3-4\nu)\Upsilon s^3}{4R^5} - k^2 \frac{\Upsilon \tilde{h} s^3}{R^4} \right)\sinh(s\tilde{h}) + \left(-\frac{E\tilde{h}s^2}{(1+\nu)R^3} - U\frac{\Upsilon \tilde{h} s^4}{4R^5} \right)\cosh(s\tilde{h})$$

$$\beta_2^*(s) = \left(\frac{E\tilde{h}s^2}{(1+\nu)R^3} + U\frac{\Upsilon \tilde{h} s^4}{4R^5} + k^2 \frac{(3-4\nu)\Upsilon s^2}{R^4} \right)\sinh(s\tilde{h}) + \left(\frac{2(1-\nu)Es}{(1+\nu)R^3} + k^2 \frac{\Upsilon \tilde{h} s^3}{R^4} \right)\cosh(s\tilde{h})$$

and μ_1 and μ_2 are the same as in (3.31), while system coefficients $\beta_{1,2}^*$ are analogous to those in (3.31) with extra parameter U. Ultimately the parameter U is analytically shown to be insignificant in regulating the horizontal deformation and is neglected in our numerical simulations.

Solving the system (3.43), (3.44) for Fourier coefficients $s^2 C(s)$ and $s^2 D(s)$ algebraically yields

$$s^2 C(s) = \frac{\mu_2(s)M(s) - \beta_2^*(s)N(s)}{\chi(s)} \qquad s^2 D(s) = \frac{\beta_1^*(s)N(s) - \mu_1(s)M(s)}{\chi(s)} \tag{3.45}$$

where the determinant of the linear system is given as

$$\chi(s) = \beta_1^*(s)\mu_2(s) - \beta_2^*(s)\mu_1(s).$$

These Fourier coefficient solutions fully define our displacement transforms $\hat{u}$ and $\hat{w}$, allowing us to apply the inverse Fourier transforms (3.32), (3.33) to obtain our displacement solutions. These transforms are carried out numerically up to a wavenumber cap S, while contributions from the truncated portion of the inverse transforms over the large wavenumber domain $|s| > S$ remain unquantified. In the following analysis we will estimate the truncated portion of these integrals and obtain finite approximations for the truncation error, showing that the horizontal curvature estimate is sufficient to resolve the displacement singularity at the contact line. These approximations are then numerically verified by varying the numerical wavenumber cap S. First we quantify the asymptotic

behavior of displacement transforms $\hat{u}$, $\hat{w}$ for large wavenumbers:

$$\hat{u}(s,\tilde{h}) = i s^2 \frac{1}{R^2}\Big[C(s)\big(-s\tilde{h}\sinh(s\tilde{h})\big) + D(s)\big((3-4\nu)\sinh(s\tilde{h}) + s\tilde{h}\cosh(s\tilde{h})\big)\Big]$$
$$\sim i\frac{1}{R^2}\Big[\mu_2(s)\big(-s\tilde{h}\sinh(s\tilde{h})\big) - \mu_1(s)\big((3-4\nu)\sinh(s\tilde{h}) + s\tilde{h}\cosh(s\tilde{h})\big)\Big]\frac{M(s)}{\chi(s)}$$
$$\sim i(3-4\nu)^2\frac{\Upsilon s^2}{R^6}\frac{M(s)}{\chi(s)}\frac{e^{2sh}}{4}$$

and

$$\hat{w}(s,\tilde{h}) = s^2 \frac{1}{R^2}\Big[C(s)\big(-(3-4\nu)\sinh(s\tilde{h}) + s\tilde{h}\cosh(s\tilde{h})\big) + D(s)\big(-s\tilde{h}\sinh(s\tilde{h})\big)\Big]$$
$$\sim \frac{1}{R^2}\Big[\beta_2^*(s)\big((3-4\nu)\sinh(s\tilde{h}) - s\tilde{h}\cosh(s\tilde{h})\big) + \beta_1^*(s)\big(-s\tilde{h}\sinh(s\tilde{h})\big)\Big]\frac{N(s)}{\chi(s)}$$
$$\sim (3-4\nu)^2\frac{k^2\Upsilon s^2}{R^6}\frac{N(s)}{\chi(s)}\frac{e^{2sh}}{4}$$

where $\chi(s)$ has asymptotic approximation for large s:

$$\chi(s) \sim \frac{(3-4\nu)\Upsilon^2}{R^8}\Big[\Big(\frac{2(1-\nu)}{(1-\nu)}\frac{R}{\Upsilon/E}\Big)s^3 + \Big((3-4\nu)k^2 - \frac{1-2\nu}{4(1+\nu)}\frac{U}{\Upsilon/E}\Big)s^4\Big]\frac{e^{2sh}}{4}. \qquad (3.46)$$

Here we note in (3.46) that $\chi(s)$ grows exponentially, cancelling the exponential terms in each of the asymptotic behaviors of $\hat{u}$ and $\hat{w}$. The remaining structure contains a cubic and quartic term, where the quartic term dominates the cubic term only in the case that at least one of the horizontal curvature parameters k^2 and U are non-zero. By the inclusion of the nonzero horizontal curvature parameters, the displacement transforms decay by s^2 as opposed to s guaranteeing a bounded solution.

Here we compare the two coefficients in the quartic term to determine which component of the horizontal curvature approximation (3.42) is dominant. Assuming solid surface stress Υ is on the same order as liquid surface tension γ, we estimate $k^2 \approx 1/3$ using Neumanns triangle. Furthermore, the maximum displacement U at the contact line is predicted to be on the order of elastocapillary length scale $L_e = \gamma/E$, so the ratio U to Υ/E is expected to be $\mathcal{O}(1)$. Taking the substrate to be nearly incompressible $(1-2\nu) \ll 1$, we approximate the ratio of the quartic coefficients in (3.42):

$$\frac{\frac{1-2\nu}{4(1+\nu)}\frac{U}{\Upsilon/E}}{(3-4\nu)k^2} \approx \frac{1-2\nu}{2} \ll 1 \qquad \Rightarrow \qquad \frac{1-2\nu}{4(1+\nu)}\frac{U}{\Upsilon/E} \ll (3-4\nu)k^2$$

From this we determine that parameter U is not significant in regulating the solution at the contact line. We therefore neglect this parameter and rely on the single parameter k^2 and its associated

curvature component to regulate the horizontal deformation. We calculate the large wavenumber asymptotic behavior for the displacement transforms to be:

$$\hat{u}(s,\tilde{h}) \sim \frac{-2iRf_t}{\sqrt{2\pi}k^2\Upsilon}\frac{\sin s}{s^2}$$

and

$$\hat{w}(s,\tilde{h}) \sim \frac{2R\gamma\sin\alpha}{\sqrt{2\pi}\Upsilon}\frac{\cos s}{s^2}$$

which derive the zero order limit equations (3.37) used in §3.2. We define our truncation error for numerical wavenumber cap S to be

$$e_x = \max_x \left|\sqrt{\frac{2}{\pi}}\int_S^\infty \left(-i\,\hat{u}(s,\tilde{h})\right)\sin(sx)ds\right| \tag{3.47}$$

$$e_z = \max_x \left|\sqrt{\frac{2}{\pi}}\int_S^\infty \left(\hat{w}(s,\tilde{h})\right)\cos(sx)ds\right| \tag{3.48}$$

The surface displacement transforms above are oscillatory and decay algebraically by s^2. Observing the structure of the truncation errors, we argue that the maximum evaluation of the truncated inverse transforms occurs at the contact line location $x = 1$ where oscillatory terms constructively interfere at identical frequency. Using the asypmtotic approximations for surface displacement transforms above, the truncated portion of the inverse transforms can be asymptotically approximated giving us errors:

$$e_x \approx \frac{2|f_t|R}{\pi k^2\Upsilon}\int_S^\infty \frac{\sin^2 s}{s^2}\,ds \approx \frac{|f_t|R}{\pi k^2\Upsilon}\frac{1}{S} \tag{3.49}$$

$$e_x \approx \frac{2\gamma\sin\alpha R}{\pi\Upsilon}\int_S^\infty \frac{\cos^2 s}{s^2}\,ds \approx \frac{\gamma\sin\alpha R}{\pi\Upsilon}\frac{1}{S} \tag{3.50}$$

Vertical and horizontal displacement errors are calculated by recording the tip displacements relative to each other for different values of S and are plotted in Fig. 3.4 along with the error estimates from (3.49) and (3.50). The numerical simulations were calculated with a non-constant surface stress ($\Upsilon_{sg} \neq \Upsilon_{ls}$) using the mean solid stress as the characteristic stress Υ. The error estimates reasonably fit the predicted error and we conclude that the deformation is bounded at the contact line by the inclusion of the general traction boundary conditions.

3.4   2D Deformation Results

Using the method outlined in §3.2, we numerically calculate both the horizontal u and vertical w surface displacements for an example substrate using (3.32), (3.33) up to a sufficient upper bound S
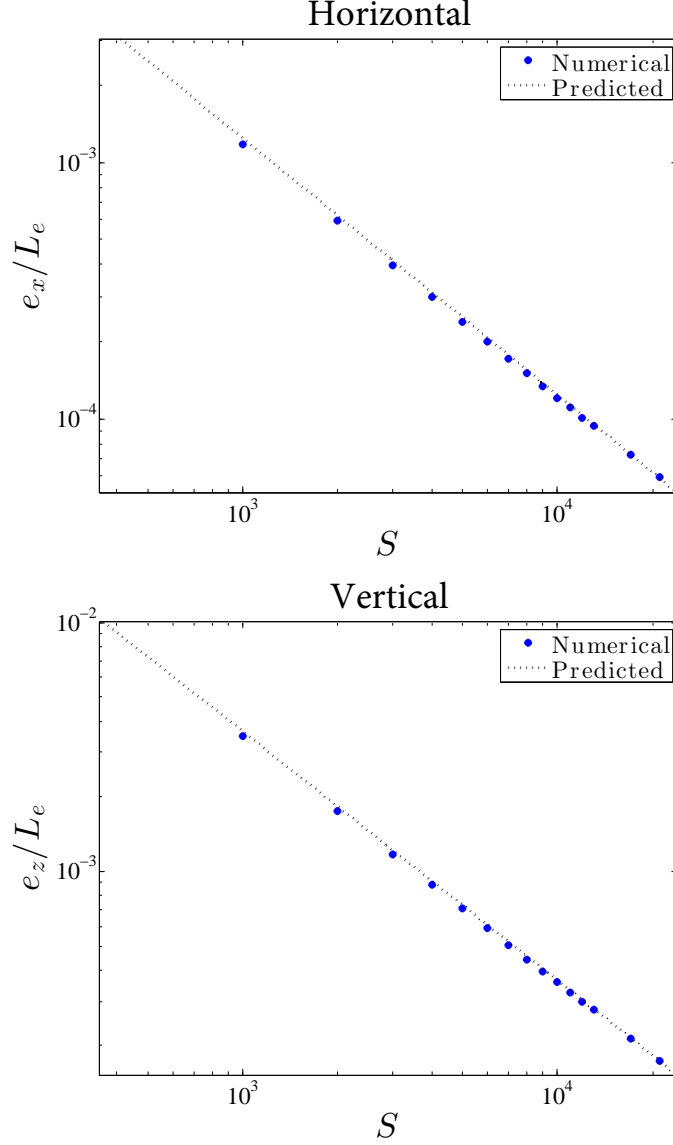
Figure 3.4 Horizontal (top) and vertical (bottom) numerical truncation error compared to predicted truncation error from (3.49), (3.50) plotted vs wave number cap S (log-log scale). Parameters: $E = 3$ kPa, $\nu = 0.47$, $h = 50\,\mu$m, $R = 150\,\mu$m, $\gamma = 50$ mN/m, $\Upsilon_{ls} = 30$ mN/m, $\Upsilon_{sg} = 42$ mN/m and $\bar{\Upsilon} = 36$ mN/m. The numerical errors e_x and e_z decay according to (3.49), (3.50), confirming the deformation is bounded at the contact line.

to reduce truncation errors (3.49), (3.50) to negligible quantities. These results are shown in Fig. 3.5 in physical units. We include the displacements calculated with the conventional contact line model ($f_t = 0$) and the generalized contact line model with f_t given by (3.18). We vary the substrate Poisson's ratio ν to illustrate the effect of compressibility on the deformation of the substrate for both

40
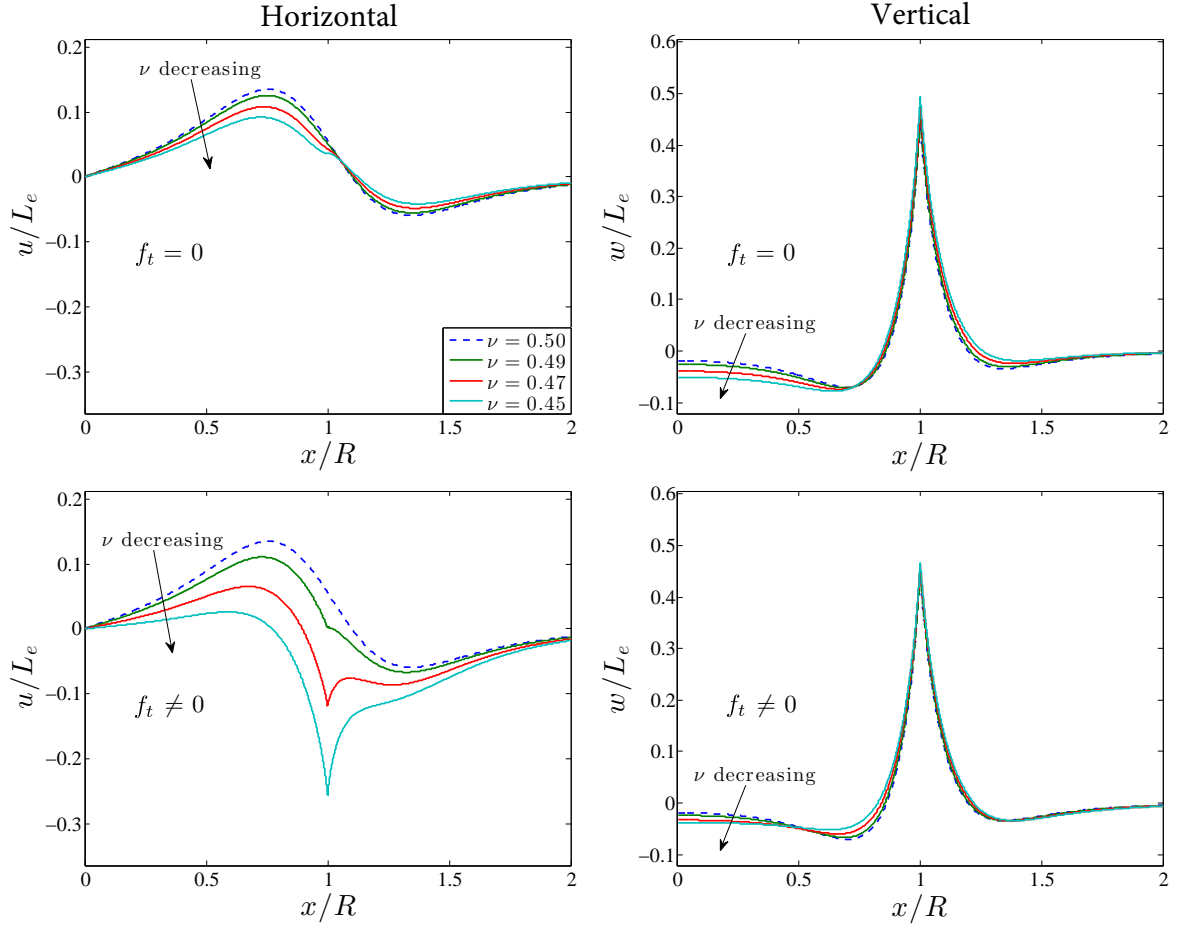
Figure 3.5 Horizontal (left) and vertical (right) displacements of the substrate surface for tangential contact line force $f_t = 0$ mN/m (top) and $f_t = (46 \text{ mN/m}) \times (1-2\nu)/(1-\nu)(1+\cos\alpha)$ (bottom). Parameters: $E = 4$ kPa, $h = 50 \, \mu$m, $R = 200 \, \mu$m, $\gamma = 46$ mN/m, $\Upsilon_{ls} = 33$ mN/m and $\Upsilon_{sg} = 38$ mN/m. (Legend in top left figure applies to all four figures.)

contact line models. Note that for the case of an incompressible substrate ($\nu = 1/2$), $f_t = 0$ regardless of the choice of contact line model, resulting in identical displacement calculations. As seen in the horizontal displacements, the non-zero tangential contact line force (3.18) pulls the substrate surface inward at the contact line location $x/R = 1$ with increasing magnitude as the Poisson's ratio ν decreases. This agrees with our intuition, as decreasing ν results in a larger tangential contact line force predicted by (3.18).

In contrast to the horizontal displacement in Fig. 3.5, the vertical displacement results are very similar, regardless of contact line model. Since the horizontal deformation is very small relative to the droplet radius R, the vertical displacement is a good visual representation of the actual sub-
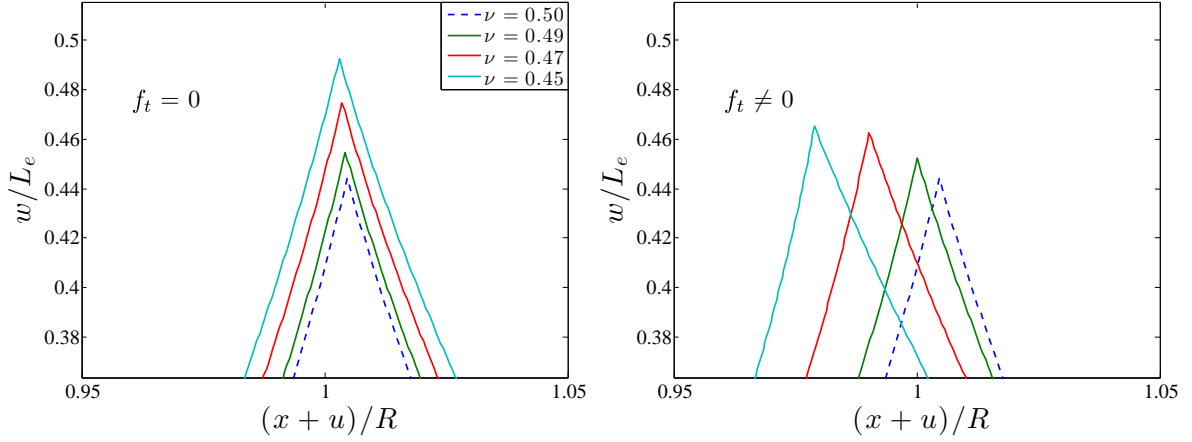
Figure 3.6 Surface deformation near the contact line for example substrate with tangential contact line force $f_t = 0$ mN/m (left) and $f_t = (46 \text{ mN/m}) \times (1-2\nu)/(1-\nu)(1+\cos\alpha)$ (right). Parameters identical to Fig. 3.5. (Legend in left figure applies to both figures.)

strate surface profile, where we observe a wetting ridge formed by the vertical contact line force. However, the horizontal deformation has a noticeable impact on the substrate surface profile near the contact line. Combining the horizontal and vertical deformations gives us the parametrized substrate surface $\vec{r}(x) = \langle x + u, w + h \rangle$, which is shown in Fig. 3.6 near the contact line for both models. This illustrates the overall effect of the contact line force and the different behavior between the two contact line models. Though not clearly visible in Fig. 3.5, the peak vertical displacement is lower for the generalized model ($f_t \neq 0$) for compressible substrates. This is the result of a small decrease in the vertical contact line force for a non-trivial tangential contact line force and constant solid surface stresses. Using the definition of Young's contact angle and the tangential force given in (3.18), we obtain

$$\cos\alpha = \frac{1-\nu}{\nu}\Big(\frac{\Upsilon_{sg} - \Upsilon_{ls}}{\gamma}\Big) + \frac{1-2\nu}{\nu}.$$

This equation increases in magnitude as ν is lowered in our simulations, resulting in a smaller vertical contact line force.

By including the previously-neglected horizontal traction stress, we gain a better understanding of the influence of the contact line in the horizontal direction. Not incorporating this horizontal traction leads to a horizontal displacement whose transform decays as $\mathcal{O}(s^{-1})$ under a non-zero f_t, which is insufficient to provide a bounded, realistic displacement. The inclusion of this stress is critical in understanding the geometry of the contact line location, at which the force necessary to induce motion is transmitted to the droplet. Fig. 3.6 provides quantitative predictions for what features to identify in future experiments. Though the tangential force is negligible for perfectly

incompressible substrates ($\nu = 1/2$), as ν decreases even slightly we see distinct changes in the contact line geometry caused by the horizontal displacement u for $f_t \neq 0$ observable in Figs. 3.5 & 3.6. Future experiments could investigate this effect.

With these advances in capability, we intend to use this model to further understand phenomena such as durotaxis, which depends largely on the displacement field and the contact angle of the droplet. Durotaxis refers to the onset motion of a droplet caused by an underlying stiffness gradient in the substrate, and has been experimentally observed [41] for droplets initially set on substrates with varying thickness. The ability for a stiffness gradient to induce droplet motion will be investigated in Chs. 5 and 6.

3.5 3D Model and Error Analysis

Here we switch our focus from the two dimensional droplet geometry to the axisymmetric three dimensional geometry. In align with Bostwick *et al* [6], we consider an axisymmetric droplet in three dimensions. Improving upon this work, we include the generalized linear curvature approximation from §3.2. Notably, by using the general linearized curvature used in §3.3 in three dimensions, we obtain similar error estimates at the contact line (3.49) and (3.50) as previously shown in 3.3, showing that the generalized curvature eliminates the displacement singularity in both rectangular and axisymmetric geometries.

Here we restrict our focus by assuming constant surface energy Υ, noting that by obtaining a bounded solution for this scenario indicates that the general scenario has bounded solution as well. We also assume the droplets are small enough such that the Laplace pressure generated by the curvature of the droplet is dominant. The Laplace pressure generated by the curvature of the droplet surface doubles compared to the two dimensional case due to the two identical principal curvatures of a spherical cap.

Notable differences in the axisymmetric case include different definitions of strains:

$$
\begin{bmatrix}
\varepsilon_{rr} & \varepsilon_{r\theta} & \varepsilon_{rz} \\
\varepsilon_{\theta r} & \varepsilon_{\theta\theta} & \varepsilon_{\theta z} \\
\varepsilon_{zr} & \varepsilon_{z\theta} & \varepsilon_{zz}
\end{bmatrix}
=
\begin{bmatrix}
\partial_r u & 0 & \frac{1}{2}(\partial_z u + \partial_r w) \\
0 & \frac{1}{r} u & 0 \\
\frac{1}{2}(\partial_z u + \partial_r w) & 0 & \partial_z w
\end{bmatrix}
$$

where u now refers to as the radial displacement and w the vertical displacement. Additionally, the Laplacian operator Δ changes form, were we define the surface Laplacian in polar coordinates:

$$\Delta_{\|}(\cdot) = \left(\partial_{rr} + \frac{1}{r}\partial_r\right)(\cdot), \tag{3.51}$$

which gives us bulk Laplacian operator

$$\Delta(\cdot) = \left(\partial_{zz} + \Delta_{\|}\right)(\cdot) = \left(\partial_{rr} + \frac{1}{r}\partial_r + \partial_{zz}\right)(\cdot).$$

We define our surface shear and normal stress boundary conditions as follows:

$$\tau_{rz}|_{z=h} = -f_t\delta(R-r) + k^2\Upsilon\Delta_{\|}u \tag{3.52}$$

$$\tau_{zz}|_{z=h} = \gamma\sin\alpha\left(\delta(R-r) - \frac{2}{R}H(R-r)\right) + \Upsilon\Delta_{\|}w \tag{3.53}$$

We wish to solve for the deformation of the substrate caused by the resting droplet. In the solution to follow, we are primarily interested in the effect of the shear stress boundary condition and how it works to regularize the deformation at the contact line. Previous work [6, 41] has solved for the deformation of the substrate using the Hankel transform. However, under the old models, a nontrivial radial contact line force f_t leaves the solution unbounded at the contact line. The inclusion of a two-component linearized curvature is shown to be sufficient in regularizing this singularity in the analysis to follow.

We use the same potential function (3.19) from §3.2 to define our displacements u and w. Following these definitions we calculate the trace of the strain tensor in axisymmetric radial coordinates:

$$\begin{aligned}
\varepsilon_{kk} &= \varepsilon_{rr} + \varepsilon_{\theta\theta} + \varepsilon_{zz} \\
&= \partial_r u + \frac{1}{r}u + \partial_z w \\
&= -\partial_{rrz}\Psi - \frac{1}{r}\partial_{rz}\Psi + 2(1-\nu)\partial_z\Delta\Psi - \partial_{zzz}\Psi \\
&= \partial_z\left(2(1-\nu)\Delta_{\|}\Psi - \Delta_{\|}\Psi + (1-2\nu)\partial_{zz}\Psi\right) \\
&= (1-2\nu)\partial_z\Delta\Psi
\end{aligned}$$

giving the same strain tensor from the 2D case:

$$\tau_{ij} = \frac{E}{1+\nu}\left[\varepsilon_{ij} + \nu\partial_z\Delta\Psi\delta_{ij}\right].$$

This is expected since the trace of the strain tensor is invariant under coordinate transformations. Again we obtain that our model equations, the elastostatic Navier equations (3.10), are satisfied if and only if our potential Ψ is biharmonic:

$$\Delta^2\Psi = 0.$$

We define a Hankel Transform pair:

$$\mathcal{H}[f(r)] = \int_0^\infty r f(r) J_0(sr)\, dr = \hat{f}(s) \tag{3.54}$$

$$\mathcal{H}^{-1}[\hat{f}(s)] = \int_0^\infty s \hat{f}(s) J_0(sr)\, ds = f(r) \tag{3.55}$$

where J_0 is the zero-th order Bessel function of the first kind. Here we calculate the Hankel transform of the surface Laplacian a function:

$$
\begin{aligned}
\mathcal{H}[\Delta_\| f(r)] &= \int_0^\infty r \Delta_\| f(r) J_0(sr)\, dr \\
&= \int_0^\infty \left(r\partial_{rr} f(r) + \partial_r f(r) \right) J_0(sr)\, dr \\
&= \int_0^\infty \partial_r \left(r\partial_r f(r) \right) J_0(sr)\, dr \\
&= \int_0^\infty s r \partial_r f(r) J_1(sr)\, dr \\
&= -\int_0^\infty s^2 r f(r) J_0(sr)\, dr \\
&= -s^2 \mathcal{H}[f(r)].
\end{aligned}
$$

This identity applied to the biharmonic potential gives us familiar ODE for the transformed potential $\hat{\Psi}$:

$$\mathcal{H}[\Delta^2\Psi] = \mathcal{H}[(\Delta_\| + \partial_{zz})^2\Psi] = \left(\frac{d^2}{dz^2} - s^2 \right)^2 \hat{\Psi} = 0$$

Solving this ODE and applying the fixed boundary conditions at $z = 0$ we obtain a general solution for transformed potential

$$\hat{\Psi}(s,z) = C(s)\psi(sz) + D(s)\left(\psi'(sz) + 2(1-2\nu)\cosh(sz) \right) \tag{3.56}$$

where we have function ψ defined by

$$\psi(\xi) = -\sinh\xi + \xi\cosh\xi \qquad \psi^{(n)}(sz) = \frac{d^n}{d\xi^n}\psi(\xi)\Big|_{\xi=sz} = s^{-n}(\partial_z)^n\psi(sz)$$

and coefficients $C(s)$ and $D(s)$ are determined by the shear and normal stress boundary conditions. Starting with the shear stress condition (3.52), we have

$$\left[\tau_{rz} - k^2\Upsilon\Delta_\| u\right]_{z=h} = -f_t\delta(R-r)$$

which redefining the left hand side in terms of potential Ψ we have

$$\tau_{rz} - k^2\Upsilon\Delta_\| u = \partial_r\left[2G\big((1-\nu)\Delta_\|\Psi - \nu\partial_{zz}\Psi\big) + k^2\Upsilon\partial_z\Delta_\|\Psi\right]$$

where $G = E/2(1+\nu)$ is the shear modulus of the substrate. Constructing the surface laplacian using the expression above we have that

$$\Delta_\|\left[2G\big((1-\nu)\Delta_\|\Psi - \nu\partial_{zz}\Psi\big) + k^2\Upsilon\partial_z\Delta_\|\Psi\right]_{z=h} = -f_t\left(\partial_r\delta(R-r) + \frac{1}{r}\delta(R-r)\right)$$

where the transform from the right hand side is evaluated:

$$\begin{aligned}
\mathscr{H}\left[\partial_r\delta(R-r) + \frac{1}{r}\delta(R-r)\right] &= \int_0^\infty (r\partial_r\delta(R-r) + \delta(R-r))\,J_0(sr)\,dr \\
&= \int_0^\infty (rsJ_1(sr) - J_0(sr) + J_0(sr))\,\delta(R-r)\,dr \\
&= sRJ_1(sR)
\end{aligned}$$

We then obtain system equation from the shear stress boundary condition:

$$s\left[2G\big((1-\nu)s^2\hat{\Psi} + \nu\partial_{zz}\hat{\Psi}\big) + k^2\Upsilon s^2\partial_z\hat{\Psi}\right]_{z=h} = -f_t RJ_1(sR) \tag{3.57}$$

Similarly with normal stress boundary condition (3.53):

$$\left[\tau_{zz} - \Upsilon\Delta_\| w\right]_{z=h} = \gamma\sin\alpha\left(\delta(R-r) - \frac{2}{R}H(R-r)\right)$$

we can define the left hand side as

$$\tau_{zz} - \Upsilon\Delta_\| w = 2G\big((2-\nu)\partial_z\Delta_\|\Psi + (1-\nu)\partial_{zzz}\Psi\big) - \Upsilon\Delta_\|\big(2(1-\nu)\Delta_\|\Psi + (1-2\nu)\partial_{zz}\Psi\big).$$

46

Evaluating the transform on the right hand side we get

$$\mathcal{H}\left[\delta(R-r)-\frac{2}{R}H(R-r)\right]=\int_0^\infty r\left(\delta(R-r)-\frac{2}{R}H(R-r)\right)J_0(sr)\,dr$$

$$=RJ_0(sR)-\frac{2}{R}\int_0^R rJ_0(sr)\,dr$$

$$=RJ_0(sR)-\frac{2}{R}\frac{r}{s}J_1(sr)\Big|_0^R$$

$$=RJ_0(sR)-\frac{2}{s}J_1(sR)$$

Giving us a second system equation from the normal stress boundary condition: Similarly with the normal stress condition we obtain a second transformed equation

$$\left[2G\left((1-\nu)\partial_{zzz}\hat{\Psi}-s^2(2-\nu)\partial_z\hat{\Psi}\right)+\Upsilon s^2\left((1-2\nu)\partial_{zz}\hat{\Psi}-2(1-\nu)s^2\hat{\Psi}\right)\right]_{z=h}$$

$$=\gamma\sin\alpha\left(RJ_0(sR)-\frac{2}{s}J_1(sR)\right) \tag{3.58}$$

These two equations are linear with respect to transform coefficients $C(s)$ and $D(s)$ and a linear system is set up and inverted to solve for C and D and thus $\hat{\Psi}$ from which the displacements, stresses and strains can be obtained. Manipulating the definitions of displacements u and w in terms of Ψ we obtain

$$u(r,z)=\int_0^\infty s^2\partial_z\hat{\Psi}J_1(sr)\,ds \tag{3.59}$$

$$w(r,z)=\int_0^\infty s\left[(1-2\nu)\partial_{zz}\hat{\Psi}-2(1-\nu)s^2\hat{\Psi}\right]J_0(sr)\,ds \tag{3.60}$$

The focus of this section is to analyze the truncation error in the calculations to confirm that the displacement singularity is regularized in the 3D geometry in addition to the 2D geometry. The integral solutions are approximated numerically up to a cutoff frequency S. For a general function $f(r)$ with Hankel transform $\hat{f}(s)$ we have

$$f(r)=\int_0^\infty s\hat{f}(s)J_0(sr)\,ds=\int_0^S s\hat{f}(s)J_0(sr)\,ds+\int_S^\infty s\hat{f}(s)J_0(sr)\,ds\approx\int_0^S s\hat{f}(s)J_0(sr)\,ds$$

as long as the error goes to zero as $S\to\infty$. An asymptotic analysis was taken of the integrands of the inverse Hankel transforms for u and w to guarantee the boundary conditions are sufficient to guarantee a bounded solution at the contact line under general contact line loading. Equations

47

(3.57) and (3.58) are a linear system for coefficients $C(s)$ and $D(s)$, written as

$$\beta(s)C(s) + \beta'(s)D(s) = M(s)$$
$$\mu(s)C(s) + \mu'(s)D(s) = N(s)$$

similar to the zero order equations in the 2D section. The coefficient functions β, β', μ, μ' and right hand sided M, N are given as (for $\epsilon = (1-2\nu)$):

$$\beta(s) = s^3\Big[2G\big((1-\nu)\psi + \nu\psi''\big) + k^2\Upsilon s\psi'\Big]_{z=h}$$
$$\beta'(s) = s^3\Big[2G\big((1-\nu)(\psi' + 2\epsilon\cosh sz) + \nu(\psi''' + 2\epsilon\cosh sz)\big) + k^2\Upsilon s(\psi'' + 2\epsilon\sinh sz)\Big]_{z=h}$$
$$\mu(s) = s^3\Big[2G\big((1-\nu)\psi''' - (2-\nu)\psi'\big) + \Upsilon s\big(\epsilon\psi'' - (\epsilon+1)\psi\big)\Big]_{z=h}$$
$$\mu'(s) = s^3\Big[2G\big((1-\nu)(\psi'''' + 2\epsilon\sinh sz) - (2-\nu)(\psi'' + 2\epsilon\sinh sz)\big)$$
$$\qquad\qquad + \Upsilon s\big(\epsilon(\psi''' + 2\epsilon\cosh sz) - (\epsilon+1)(\psi' + 2\epsilon\cosh sz)\big)\Big]_{z=h}$$
$$M(s) = -f_t R J_1(sR)$$
$$N(s) = \gamma\sin\alpha\Big[R J_0(sR) - \frac{2}{s}J_1(sR)\Big]$$

The linear system above has general solution

$$C(s) = \frac{\mu' M - \beta' N}{\beta\mu' - \beta'\mu} \qquad \text{and} \qquad D(s) = \frac{\beta N - \mu M}{\beta\mu' - \beta'\mu} \tag{3.61}$$

We want to analyze the effect of the radial component of curvature which is neglected in previous models. Normally the radial component of curvature is neglected but we will show that it is necessary to include to provide a bounded solution for nonzero radial contact line force f_t. We do this by showing that $k^2 \neq 0$ is necessary for the error to decay to zero and also calculate truncation error estimates for the inverse Hankel transforms. We define the truncation errors to be

$$e_r = \int_S^\infty s^2\partial_z\hat{\psi}(s,h)J_1(sR)\,ds \tag{3.62}$$

and

$$e_z = \int_S^\infty s\big(\epsilon\partial_{zz}\hat{\psi}(s,h) - (\epsilon+1)\hat{\psi}(s,h)\big)J_0(sR)\,ds \tag{3.63}$$

which should go to zero as $S \to \infty$ guaranteeing a bounded solution at the contact line. Using the definition of $\hat{\Psi}(s,z)$ from (3.56) and the solution for the coefficients $C(s)$ and $D(s)$ from (3.61), we

have:

$$e_r = \int_S^\infty s^3 \frac{M[\mu'\psi' - \mu(\psi'' + 2\epsilon \sinh sh)] + N[\beta(\psi'' + 2\epsilon \sinh sh) - \beta'\psi']}{\beta\mu' - \beta'\mu} J_1(sR)\, ds \qquad (3.64)$$

and

$$e_z = \int_S^\infty s^3 \Bigg[\frac{M[\mu(\psi' + 2\epsilon \cosh sh) - \mu'\psi + \epsilon(\mu'(\psi'' - \psi) - \mu(\psi''' - \psi'))]}{\beta\mu' - \beta'\mu} +$$

$$\frac{N[\beta'\psi - \beta(\psi' + 2\epsilon \cosh sh) + \epsilon(\beta(\psi''' - \psi') - \beta'(\psi'' - \psi))]}{\beta\mu' - \beta'\mu} \Bigg] J_0(sR)\, ds \qquad (3.65)$$

We then take the asymptotic behavior of the Bessel functions

$$J_0(sR) \sim \sqrt{\frac{2}{\pi sR}} \cos(sR - \pi/4)$$

$$J_1(sR) \sim \sqrt{\frac{2}{\pi sR}} \sin(sR - \pi/4)$$

giving us large wavenumber behavior of our system equations M and N:

$$M(s) \sim -f_t \sqrt{\frac{2R}{\pi s}} \sin(sR - \pi/4)$$

$$N(s) \sim \gamma \sin\alpha \sqrt{\frac{2R}{\pi s}} \cos(sR - \pi/4)$$

where we note that $M(s)$ constructively interferes with $J_1(sR)$ and $N(s)$ constructively interferes with $J_0(sR)$. From this we obtain estimates for errors:

$$e_r \sim \int_S^\infty -f_t \frac{2}{\pi} s^2 \frac{\mu'\psi' - \mu(\psi'' + 2\epsilon \sinh sh)}{\beta\mu' - \beta'\mu} \sin^2(sR - \pi/4)\, ds$$

$$\sim \frac{-f_t}{\pi} \int_S^\infty s^2 \frac{\mu'\psi' - \mu(\psi'' + 2\epsilon \sinh sh)}{\beta\mu' - \beta'\mu}\, ds \qquad (3.66)$$

and

$$e_z \sim \int_S^\infty \gamma \sin\alpha \frac{2}{\pi} s^2 \frac{\beta'\psi - \beta(\psi' + 2\epsilon \cosh sh) + \epsilon(\beta(\psi''' - \psi') - \beta'(\psi'' - \psi))}{\beta\mu' - \beta'\mu} \cos^2(sR - \pi/4)\, ds$$

$$\sim \frac{\gamma \sin\alpha}{\pi} \int_S^\infty s^2 \frac{\beta'\psi - \beta(\psi' + 2\epsilon \cosh sh) + \epsilon(\beta(\psi''' - \psi') - \beta'(\psi'' - \psi))}{\beta\mu' - \beta'\mu}\, ds \qquad (3.67)$$

49

Examining the large frequency asymptotic behavior of the coefficient functions, we have expansions:

$$\beta(s) \sim \frac{s^3 e^{sh}}{2}\left[2G(sh-\epsilon)+k^2\Upsilon s^2 h\right]$$

$$\beta'(s) \sim \frac{s^3 e^{sh}}{2}\left[2G(sh+\epsilon+1)+k^2\Upsilon s(sh+1+2\epsilon)\right]$$

$$\mu(s) \sim \frac{s^3 e^{sh}}{2}\left[2G(-sh+\epsilon+1)+\Upsilon s(-sh+1+2\epsilon)\right]$$

$$\mu'(s) \sim \frac{s^3 e^{sh}}{2}\left[2G(-sh-\epsilon)-\Upsilon s^2 h\right]$$

Below we obtain an asymptotic approximation of the denominator $\beta\mu'-\beta'\mu$:

$$\beta\mu' \sim s^6 \frac{e^{2sh}}{4}\left[-4G\left((sh)^2-\epsilon^2\right)-2G\Upsilon h s^2\left((sh-\epsilon)+k^2(sh+\epsilon)\right)-k^2\Upsilon^2 h^2 s^4\right]$$

$$\beta'\mu \sim s^6\frac{e^{2sh}}{4}\left[-4G\left((sh)^2-(\epsilon+1)^2\right)-2G\Upsilon s\left((sh+1+\epsilon)(sh-1-2\epsilon)\right.\right.$$
$$\left.\left.+k^2(sh-1-\epsilon)(sh+1+2\epsilon)\right)-k^2\Upsilon^2 s^2\left((sh)^2-(1+2\epsilon)^2\right)\right]$$

$$\Rightarrow \beta\mu'-\beta'\mu \sim s^6\frac{e^{2sh}}{4}\left[4G(1+2\epsilon)-2G\Upsilon s(1+k^2)(1+\epsilon)(1+2\epsilon)-k^2\Upsilon^2 s^2(1+2\epsilon)^2\right]$$

Therefore, for $k^2 \neq 0$, we have

$$\beta\mu'-\beta'\mu \sim -(1+2\epsilon)^2 k^2\Upsilon^2 s^8\frac{e^{2sh}}{4}$$

and for $k^2 = 0$ (neglecting the radial component of curvature), we have

$$\beta\mu'-\beta'\mu \sim -2(1+2\epsilon)(1+\epsilon)G\Upsilon s^7\frac{e^{2sh}}{4}$$

Asymptotic expansions of the numerators from (3.66), (3.67):

$$\text{Radial:} \quad \mu'\psi'-\mu(\psi''+2\epsilon\sinh sh) \sim \frac{e^{sh}}{2}\left(sh\mu'-(sh+1+2\epsilon)\mu\right)$$

$$\sim s^3\frac{e^{2sh}}{4}\left[-2Gsh(sh+\epsilon)-\Upsilon s^3 h^2-(sh+1+2\epsilon)\left(-2G(sh-1-\epsilon)-\Upsilon s(sh-1-2\epsilon)\right)\right]$$

$$=-s^3\frac{e^{2sh}}{4}\left[2G(1+\epsilon)(1+2\epsilon)+\Upsilon s(1+2\epsilon)^2\right] \sim -(1+2\epsilon)^2\Upsilon s^4\frac{e^{2sh}}{4} \tag{3.68}$$

50

$$\text{Vertical:} \quad \beta'\psi - \beta(\psi' + 2\epsilon\cosh sh) + \epsilon\big(\beta(\psi''' - \psi') - \beta'(\psi'' - \psi)\big)$$

$$\sim \frac{e^{sh}}{2}\big((sh-1)\beta' - (sh+2\epsilon)\beta + 2\epsilon(\beta - \beta')\big)$$

$$\sim s^3 \frac{e^{2sh}}{4}\Big[(sh-1)\big(2G(sh+1+\epsilon) + k^2\Upsilon s(sh+1+2\epsilon)\big) - $$

$$(sh+2\epsilon)\big(2G(sh-\epsilon) + k^2\Upsilon s^2 h\big) - 2\epsilon(1+2\epsilon)\big(2G + k^2\Upsilon s\big)\Big]$$

$$= -s^3 \frac{e^{2sh}}{4}\Big[2G(1+\epsilon)(1+2\epsilon) + k^2\Upsilon s(1+2\epsilon)^2\Big] \tag{3.69}$$

We now compute the asymptotic expansions to obtain the truncation error estimates. We will compute the error estimate for the case that $k^2 \neq 0$ and show that the radial deformation is unbounded with the exclusion of the radial component of curvature ($k^2 = 0$). The truncation error estimates are computed as follows following (3.66) and (3.67):

$$e_r \sim \frac{-f_t}{\pi}\int_S^\infty s^2 \frac{-(1+2\epsilon)^2\Upsilon s^4}{-(1+2\epsilon)^2 k^2\Upsilon^2 s^8}\, ds = \frac{-f_t}{\pi k^2\Upsilon}\int_S^\infty s^{-2}\, ds = \frac{-f_t}{\pi k^2\Upsilon}\frac{1}{S} \tag{3.70}$$

and

$$e_z \sim \frac{\gamma\sin\alpha}{\pi}\int_S^\infty s^2 \frac{-(1+2\epsilon)^2 k^2\Upsilon s^4}{-(1+2\epsilon)^2 k^2\Upsilon^2 s^8}\, ds = \frac{\gamma\sin\alpha}{\pi\Upsilon}\int_S^\infty s^{-2}\, ds = \frac{\gamma\sin\alpha}{\pi\Upsilon}\frac{1}{S} \tag{3.71}$$

Which both decay to zero as frequency cap $S \to \infty$ guaranteeing a bounded solution at the contact line for both radial and vertical deformations. If we neglect the radial component of curvature, we have radial deformation error estimate given by

$$e_r \sim \frac{-f_t}{\pi}\int_S^\infty s^2 \frac{-(1+2\epsilon)^2\Upsilon s^4}{-2(1+2\epsilon)(1+\epsilon)G\Upsilon s^7}\, ds = \frac{-(1+2\epsilon)f_t}{2\pi(1+\epsilon)G}\int_S^\infty s^{-1}\, ds \to \infty$$

illustrating that without the radial component of curvature, the radial deformation transform does not decay appropriately giving an infinite deformation at the contact line. Just as the vertical component of curvature is necessary to bound the vertical displacement, the radial component is necessary to bound the radial displacement.

3.6 Comparison of Two Dimensional and Axisymmetric Deformations

Using the solution methods outlined in both §3.2 for the two dimensional case and §3.5 for the axisymmetric case, we plot the displacements in both both the two dimensional geometry and three dimensional axisymmetric geometry in Fig. 3.7. As can be seen in the horizontal/radial deformation plot, the tangential contact line force $f_t = 5$ mN/m pulls in at the contact line location, while the vertical force $f_n = 80$ mN/m pulls up at the contact line in the vertical plot forming the wetting ridge.

When comparing the axisymmetric case to the two dimensional case, we see that the results are qualitatively similar. We observe some differences, notably a higher compression in the substrate below the droplet in the axisymmetric case when compared to the two dimensional case. This can be attributed the the larger Laplace pressure generated by the two principal curvatures of the droplet. We also observe that the radial deformation is slightly larger in the axisymmetric case as opposed to the two dimensional case. This again can be attributed to the difference in geometry of droplet acting on an incompressible solid ($\nu = 1/2$). Positive radial deformation represents outward stretching of the surface. In two dimensions this horizontal deformation is more balanced as at each x value, a given value of horizontal stretch corresponds to the same increase of volume locally, whereas larger radial deformations in three dimensions closer to the origin $r = 0$ correspond to less local dilation as a radial deformation farther away from the origin. For this reason we see more extreme positive values of radial deformation near the origin and less extreme negative values of radial deformation away from the origin than compared to the two dimensional case.

For comparison, we also plot the radial deformation results using the single term linearized curvature used in previous work. These are plotted in Fig. 3.8. We see in §3.3 and §3.5 that for wavenumber cap S the horizontal/radial truncation error is bounded and decays to zero for the case that $k^2 \neq 0$ giving us a nonzero horizontal/radial traction force preventing a singularity. Without this horizontal/radial traction, or equivalently setting $k^2 = 0$ we observe a logarithmic singularity in the radial deformation at the contact line. The predicted deformation neglecting this term is shown in Fig. 3.8.

These plots in Fig. 3.8 highlight the importance of the inclusion of a general curvature providing a bounded solution at the contact line for both geometries. Taking this advancement in the model forward to our analysis in Ch. 5 & Ch. 6 will be necessary when considering asymmetric droplets as deviation from Young's contact angle introduces nontrivial contact line force of the form $f_t = \gamma(\cos\alpha - \cos\theta_Y)$ as discussed in §2.3.
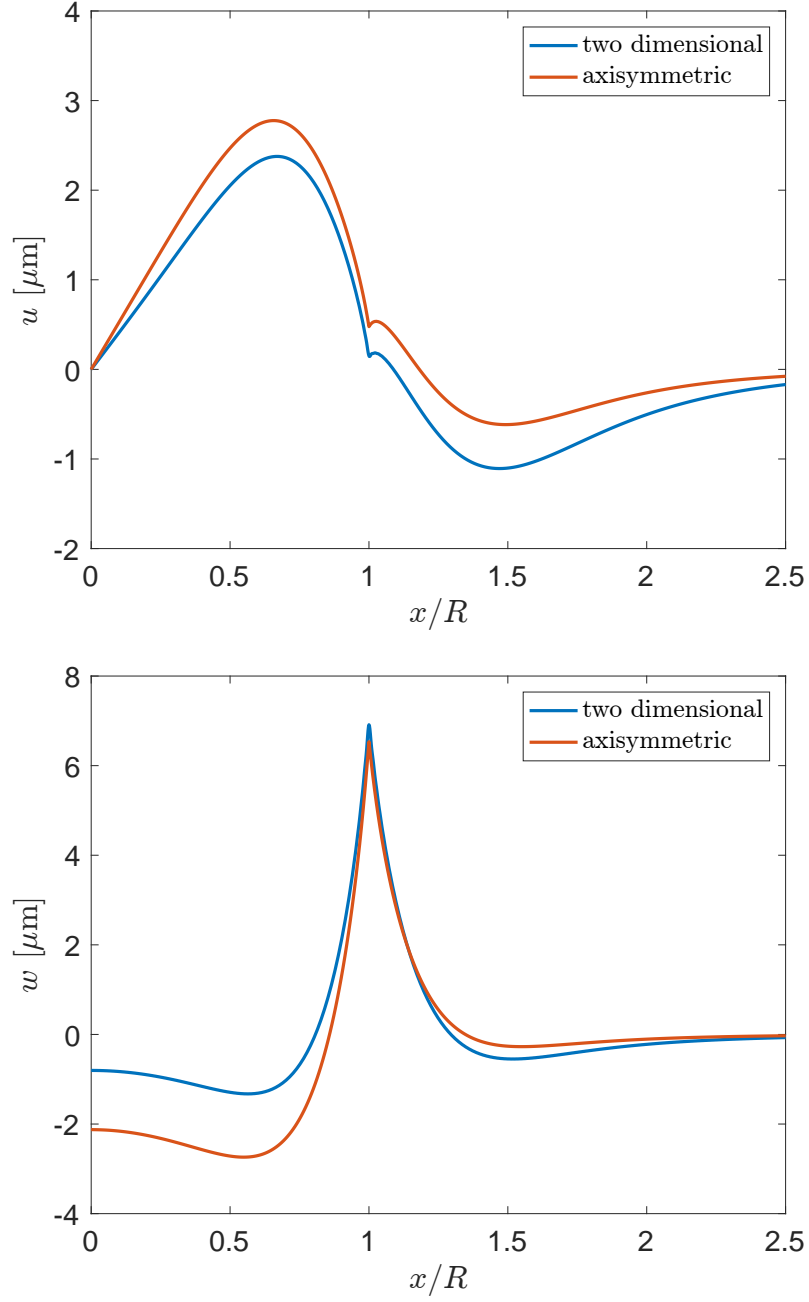
Figure 3.7 Plot of horizontal/radial u (top) and vertical w (bottom) deformations for both the two dimensional and axisymmetric droplet geometries. Parameters: $\gamma = \Upsilon_{ls} = \Upsilon_{sg} = 80$ mN/m, $\alpha = \pi/2$ rad, $k^2 = 1/3$, $E = 6$ kPa, $\nu = 1/2$, $h = 50$ μm, $R = 150$ μm and $f_t = 5$ mN/m.
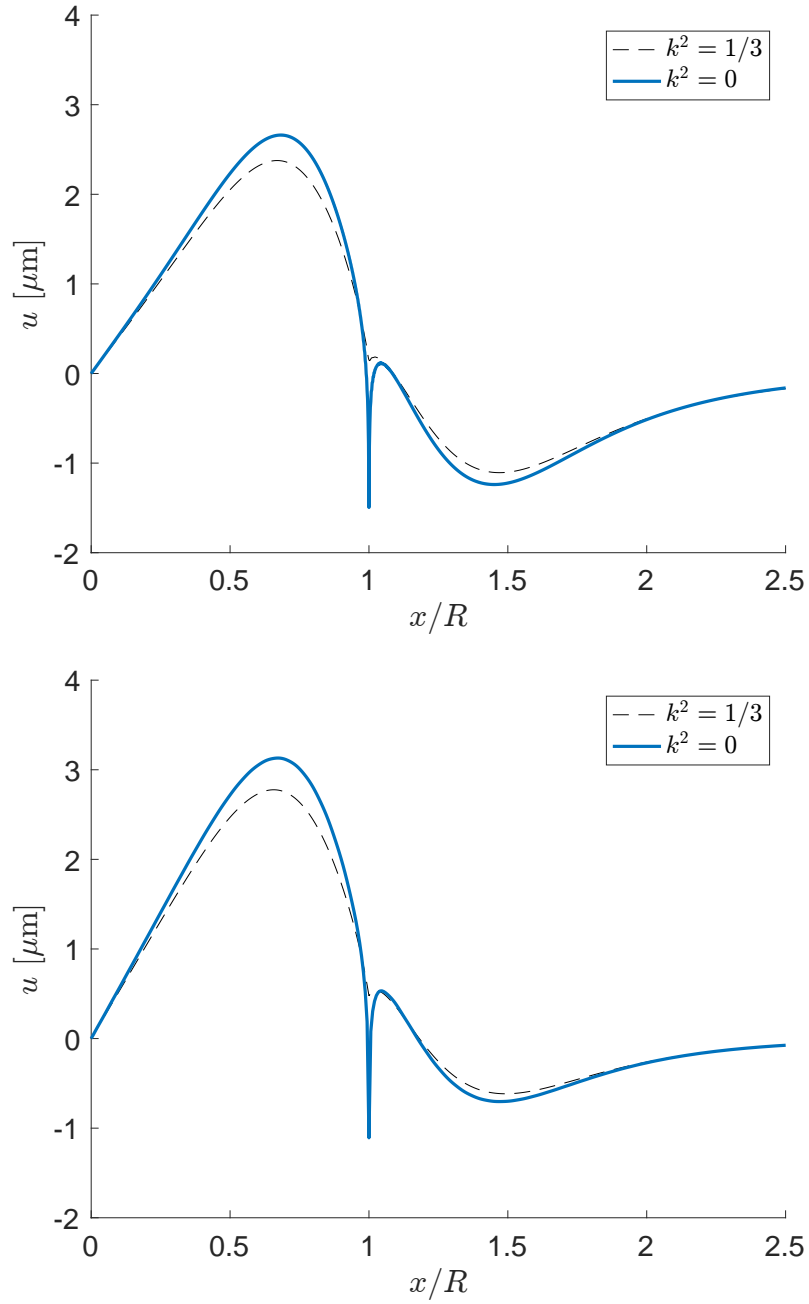
Figure 3.8 Plot of horizontal deformation u for the two dimensional geometry (top) and radial deformation u for the axisymmetric geometry (bottom) with zero horizontal/radial traction term. Nondimensional wavenumber cap $S = 2000$ used for two dimensional case while wavenumber cap S for axisymmetric case defined such that $SR = 2000$. Parameters: $\gamma = \Upsilon_{ls} = \Upsilon_{sg} = 80$ mN/m, $\alpha = \pi/2$ rad, $E = 6$ kPa, $\nu = 1/2$, $h = 50$ μm, $R = 150$ μm and $f_t = 5$ mN/m.

4

DEFORMATION OF A PARTIALLY SUBMERGED ROD

In this chapter, we develop a model to calculate the displacement of a thin elastic rod partially submerged in a fluid bath in order to investigate a tangential contact line force proposed by Marchand *et al* [28]:

$$f_t = \gamma(1 + \cos\theta_Y)$$

pulling toward the liquid phase. Using a simplified one dimensional elastic model, we calculate predicted displacements u_z in the rod as a function of vertical coordinate z as done similarly in [28], with a contact line force left to be determined by fitting the data to the derived model and solving for the best fit force at the contact line.

Though not corresponding directly to the droplet geometry discussed in Chs. 3, 5 & 6, the investigation of the nature of contact lines in producing tangential contact line forces is crucial to understand for both the rod as well as the droplet geometries. Ultimately through our collaborations with Shih-Yuan Chen, a graduate student working on experiments to test the model outlined here, we acknowledge several experimental issues which were addressed in order to obtain useful data. One of these issues being the proper cleaning of the gel surface removing uncrosslinked monomers within the rod matrix which normally would be extruded from the solid affecting the
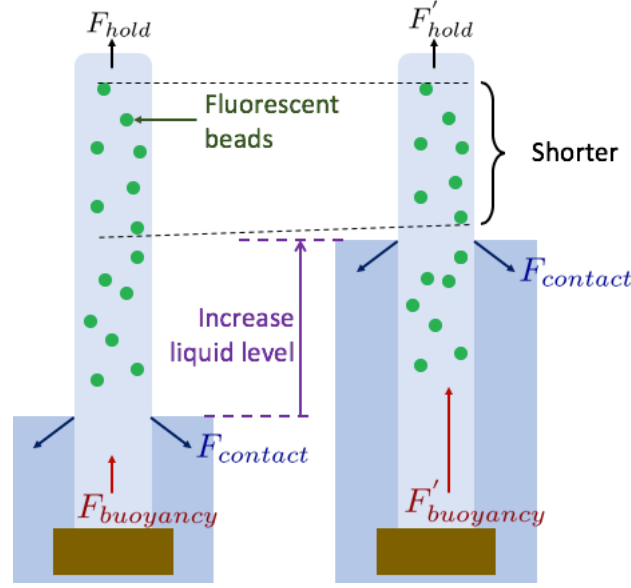
Figure 4.1 Experimental setup with partially submerged rod at different fluid levels. Fluorescent beads measure the relative position from one state to the next from which relative strain is calculated between the two states. Buoyancy acts on the submerged portion of the gel. Orientation of the contact line force $F_{contact}$ is to be determined by the relative strains. Photo credit: Shih-Yuan Chen.

surface energies at the air-liquid-solid triple line [15, 16] ultimately altering the predictions made by the model. In addition, issues such as gel swelling by the fluid and fluid evaporation needed to be addressed by proper choice of fluid. The effect of swelling is qualitatively shown in the results §4.2.

In addition, improving upon the model of Marchand *et al*, we predict an extra term in our strain equation associated with the buoyancy of the submerged portion of the rod. The inclusion of this term in our model is crucial in matching the experimental deformation data obtained by Chen illustrated in Fig. 4.2. Through addressing the experimental difficulties associated with the rod geometry and careful investigation of the rod deformation model, evidence for a tangential contact line force as proposed by Marchand *et al* becomes less convincing.

First an outline of the model solution is provided in §4.1. Then the resulting equations for deformation are obtained and compared to that of the experimental data obtained by Chen. Conjecture for the absence of a tangential contact line force is presented based on both a theoretical argument as well as experimental results by Chen.

4.1 Rod Deformation Model

To solve for the axial deformation u_z in the rod, we derive an expression for the axial strain $\varepsilon_{zz} = \partial_z u_z$ as a function of applied axial and radial stresses, then we will incorporate the stresses induced by the partial submersion, then we will calculate expressions to predict the net axial displacement in the gel caused by adjusting the fluid level. Here we note that the solution is axisymmetric as no torque is applied to the rod and thus all variations with respect to angle θ can be set to zero. Next we note for a small radius that $\varepsilon_{rr} \approx \varepsilon_{\theta\theta}$ as by a Taylor expansion we find that $\partial_r u_r - u_r/r \approx 0$. Taking this approximation and manipulating the trace equation we have

$$\varepsilon_{kk} = \varepsilon_{rr} + \varepsilon_{\theta\theta} + \varepsilon_{zz} \approx 2\varepsilon_{rr} + \varepsilon_{zz}$$

$$\Rightarrow \varepsilon_{rr} = \frac{1}{2}\left(\varepsilon_{kk} - \varepsilon_{zz}\right)$$

The following calculation then isolates an expression for axial strain $\varepsilon_{zz} = \partial_z u_z$:

$$\sigma_{zz} - 2\nu\sigma_{rr} = \frac{E}{1+\nu}\left[(\partial_z u_z - 2\nu\partial_r u_r) + \frac{\nu}{1-2\nu}(1-2\nu)\varepsilon_{kk}\right]$$

$$= \frac{E}{1+\nu}\left[(\partial_z u_z - \nu(\varepsilon_{kk} - \partial_z u_z)) + \nu\varepsilon_{kk}\right] = E\partial_z u_z$$

$$\Rightarrow \varepsilon_{zz} = \partial_z u_z = \frac{1}{E}\left[\sigma_{zz} - 2\nu\sigma_{rr}\right] \tag{4.1}$$

We define F_{hold} to be the force per unit length needed to support the thread from above as seen in Fig. 4.1. This value can be derived using the principal of virtual work, where we take the first variation of the total energy $\mathscr{E}_{total}$ with respect to the dry length of the rod, resulting in the total external force required to keep the rod in position. We have that

$$2\pi R F_{hold} = \delta\mathscr{E}_{total} = \lim_{\epsilon \to 0} \frac{\mathscr{E}_{total}(\epsilon) - \mathscr{E}_{total}(0)}{\epsilon}$$

Here $\mathscr{E}_{total}$ refers to the sum of surface and potential energies. We let γ_{sg} and γ_{ls} be the solid-gas and liquid-solid surface energies respectively and let $L = L_{sg} + L_{ls}$ be the total length of the rod of radius R, where L_{sg} and L_{ls} are the initial dry and submerged lengths of the rod. Then for

$$\mathscr{E}_{total} = \mathscr{E}_{surface} + \mathscr{E}_{potential}$$

we have that for the rod to be pulled up a length ϵ out of the fluid, extending the dry portion of the rod by length ϵ

$$\mathscr{E}_{surface}(\epsilon) = 2\pi R\left((L_{sg} + \epsilon)\gamma_{sg} + (L_{ls} - \epsilon)\gamma_{ls}\right)$$

$$\Rightarrow \frac{\mathscr{E}_{surface}(\epsilon) - \mathscr{E}_{surface}(0)}{\epsilon} = 2\pi R(\gamma_{sg} - \gamma_{ls})$$

In addition to the surface energy changing, we also have an increase in gravitational potential energy. To calculate this we take a slice of the solid rod of thickness ϵ from the bottom of the rod and calculate the energy needed to lift it to be placed at the top of the rod. We acknowledge that buoyancy acts on this thin slice as it is being lifted through the liquid, while not through the surrounding air. Defining ρ_s and ρ_l to be the density of the solid and liquid respectively, we define the effective weight density in the liquid, or the specific force needed to move the mass upward, to be $\Delta\rho g = (\rho_s - \rho_l)g$. From this we have that

$$\mathscr{E}_{potential}(\epsilon) = \pi R^2 g \int_0^\epsilon \Delta\rho(L_{ls} - \xi) + \rho_s(L_{sg} + \xi)\, d\xi$$

$$\Rightarrow \lim_{\epsilon \to 0} \frac{\mathscr{E}_{potential}(\epsilon) - \mathscr{E}_{potential}(0)}{\epsilon} = \pi R^2 g\big(\Delta\rho\, L_{ls} + \rho_s L_{sg}\big)$$
$$= \pi R^2 g\big(\rho_s L - \rho_l L_{ls}\big)$$
$$= g(\rho_s V - \rho_l V_{submerged})$$

Subtracting off the preloaded force of gravity we then obtain our external force

$$2\pi R F_{hold} = 2\pi R\gamma\cos\theta - \rho_l g V_{submerged}$$

where R is the radius of the rod, γ is the liquid-vapor surface stress, θ is Young's angle for the contact line, ρ_l is the liquid density, g the gravitational constant and V_{ls} the submerged volume. In addition we suppose the bottom of the submerged rod is subject to upward force given by

$$2\pi R F_{bottom} = 2\pi R\Gamma + \rho_l g V_{submerged}$$

where the first term contains an unknown Γ which we will treat as a fitting parameter for the effective surface tension along the perimeter of the rod and the remaining term is a result of buoyancy. Note that this leaves an unresolved force at the contact line given by

$$2\pi R F_{contact} = 2\pi R(\gamma\cos\theta + \Gamma)$$

oriented into the fluid. Note that if $\Gamma = -\gamma\cos\theta$ that there is no net contact line force, and if $\Gamma = \gamma$ we obtain the proposed form by Marchand *et al*. We suspect the former to be true as by replacing solid-gas surface energy γ_{sg} with liquid-solid surface energy γ_{ls} upon submersion, the change in hoop stress σ_{hoop} applied relative to the dry state would be the same as that caused alleviating the rod of hoop stress caused by solid-gas surface energy in its base state and replacing it with that of

liquid-solid surface energy upon submersion, giving us

$$\sigma_{hoop} = \frac{\gamma_{sg} - \gamma_{ls}}{R} = \frac{\gamma \cos\theta}{R}$$

and since the magnitude of axial stress is double that of the hoop stress, we have that the resulting upward force should be given by $-2\pi R\gamma\cos\theta$, or equivalently $\Gamma = -\gamma\cos\theta$ corresponding to a tangential contact line force of zero fitting the conventional model for rigid solids.

In addition to vertical forces, we consider axial stresses resulting from the solid surface stress. As there is no change in hoop stress for the unsubmerged portion of the gel, we suppose that $\sigma_{rr}|_{z>0} = 0$. The hoop stress in the submerged portion of the gel can be written as $\sigma_{rr}|_{z<0} = -\Gamma/R + \rho_l g z$, the first term having to do with the surface stress and the second with hydrostatic pressure. Taking this information we can describe both the axial and radial stresses applied on both portions of the gel provided below:

$$\sigma_{zz}(R,\theta,z) = \begin{cases} -2\Gamma/R - \rho_l g L_{ls} & z < 0 \\ 2\gamma\cos\theta/R - \rho_l g L_{ls} & z > 0 \end{cases}$$

and

$$\sigma_{rr}(R,\theta,z) = \begin{cases} -\Gamma/R + \rho_l g z & z < 0 \\ 0 & z > 0 \end{cases}$$

Using these stresses we solve for the axial strain using the solution given in the previous section. We obtain

$$\varepsilon_{zz}(R,\theta,z) = \begin{cases} \frac{1}{E}\left(-\Gamma/R - \rho_l g(2\nu z + L_{ls})\right) & z < 0 \\ \frac{1}{E}\left(2\gamma\cos\theta/R - \rho_l g L_{ls}\right) & z > 0 \end{cases}$$

The experiment measures the net displacement in the rod after raising the fluid level by ΔL between the left and right states as seen is Fig. 4.1. We calculate the resulting displacements above and below the new fluid level using the strains predicted by the model. Primes will denote the second state (raised fluid level) while the original state is notated normally. The net strain above the raised liquid level is given by

$$\partial_z u_z(z' > 0) = \varepsilon_{zz}(R,\theta,z' > 0) - \varepsilon_{zz}(R,\theta,z > 0)$$

$$= \frac{1}{E}\left[-\rho_l g(L'_{ls} - L_{ls})\right] = -\frac{\rho_l g \Delta L}{E}$$

while the net strain evaluated below the raised liquid level is given by

$$\partial_z u_z(z' < 0) = \varepsilon_{zz}(R,\theta,z' < 0) - \varepsilon_{zz}(R,\theta,z > 0)$$

$$= \frac{1}{E}\left[-\frac{2\gamma\cos\theta + \Gamma}{R} - \rho_l g(2\nu z' + \Delta L)\right]$$

Taking $z' \to z$ for the new liquid level, we integrate these formulas and set the displacement to zero at the origin to obtain expressions for the displacements above and below the final liquid level:

$$u_z(-\Delta L < z < 0) = \frac{1}{E}\Big[-\frac{2\gamma\cos\theta + \Gamma}{R}z - \rho_l g z(\nu z + \Delta L)\Big] \tag{4.2}$$

and

$$u_z(z > 0) = -\frac{\rho_l g \Delta L}{E}z \tag{4.3}$$

These results differ from [28] in that they neglected to include buoyancy in the external force calculation, and is of large enough magnitude to be significant in the deformation results.

4.2   Results

Experimental work by Chen has shown that (4.3) accurately fits data using a PVS gel thread submerged in both glycerol and FC-40 fluids chosen to avoid issues such as swelling and evaporation as presented in Fig. 4.2. In addition, the necessary experimental procedures to avoid these issues suggest that the result achieved by Marchand *et al* should be revisited with proper attention to these concerns. These experimental concerns include the proper cleaning of the gel surface to avoid uncrosslinked monomers from being extruded into the fluid affecting assumed physical values such as surface tension, as seen in [1, 16], as well as swelling and evaporation mentioned earlier.

Swelling interferes with measurements of strain by breaking the assumption that the solid remains in complete phase separation from the fluid. Using a fluid such as ethanol which increases the volume of the submerged gel increases the volume of the gel pushing it upward. This is depicted in Fig. 4.2, where using ethanol as the wetting fluid not only increased the strain, it changed the sign of the strain in the dry portion of the gel. By isolating this effect and removing it from experiments as done by Chen *et al* using the model outlined here, there is reason to investigate whether these experimental issues unknowingly affected the results of Marchand *et al* and the orientation of the contact line force F_{cl} needs to be further analyzed experimentally. We suspect that in light of the experimental difficulties encountered and solved by Chen, including swelling, we may obtain results suggesting the absence of a tangentially directed force at the contact line. This would then quantitatively agree with the conventional contact line model which proposes the net force by a contact line is normal to the surface and suggest that this is not an issue of geometry. This opens the possibility of testing contact line models on geometries other than droplets as discussed in Ch. 3.
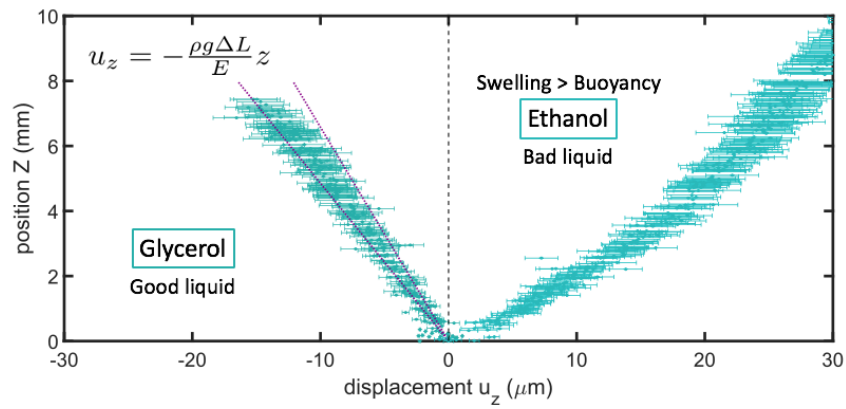
Figure 4.2 Axial displacement u_z of the PVS gel above the contact line. Theoretical prediction range plotted in purple and experimental data plotted in blue for both glycerol (left) and ethanol (right). The glycerol does not swell the PVS gel and fits the theoretical prediction of the model well, whereas the swelling caused by the ethanol causes the data to fall well outside the theoretically predicted range. Figure Credit: Shih-Yuan Chen.

CHAPTER

5

SUBSTRATE GRADIENTS AND ASYMMETRIC DEFORMATION

In this chapter we investigate a two dimensional deformation model in a soft substrate with a gradient in stiffness $G(x)$ as well as in solid surface energy $\gamma_s(x)$. We will restrict our focus to that of incompressible substrates where the Poisson's ratio $\nu = \frac{1}{2}$. In addition, for simplicity we assume that the strain dependence of the surface stress is negligible in the Shuttleworth equation (1.2):

$$\gamma_s \gg \frac{\partial \gamma_s}{\partial \varepsilon_\parallel}.$$

This allows us to set the surface stress $\Upsilon(x)$ equal to $\gamma_s(x)$. Furthermore we restrict the analysis to that where the solid surface energy $\gamma_s(x)$ is assumed to be constant, representative of droplets with Young's angle $\theta_Y = 90°$. For the case of applying a gradient in stiffness $G(x)$, we will take the solid surface energy γ_s to be constant and in the case of the surface energy gradient we will take shear modulus G to be constant.

By allowing spatially dependent substrate properties such as stiffness G and surface energy γ_s, the static deformation caused by a resting fluid droplet becomes asymmetric. Altering these properties also affects the apparent contact angle of the droplet [27, 41, 43], so allowing stiffness or surface energy to become spatially dependent in general allows for our two dimensional droplet to have

an asymmetric profile and a nonzero difference in contact angle from left to right. This contact angle difference determines the onset of droplet motion [1, 43] and we will use the magnitude of contact angle difference from Style *et al* [43] of 1.8° as a benchmark for inducing droplet motion. We acknowledge that this threshold may be a function of the liquid-solid system, but as indicated by the results of Style *et al* this is not a function of the droplet size.

Throughout the remainder of the thesis we will use the linear incompressible stress tensor

$$\tau_{ij}(x,z) = 2G(x)\varepsilon_{ij}(x,z) - p(x,z)\delta_{ij} \tag{5.1}$$

where G is the shear modulus of the substrate and p represents the isotropic stress in the solid. Along with this stress tensor, for a finite value of p we enforce the incompressibility condition

$$\varepsilon_{kk} = \varepsilon_{xx} + \varepsilon_{zz} = \partial_x u + \partial_z w = 0 \tag{5.2}$$

Again we enforce stress boundary conditions introduced previously, though due to the asymmetry we allow in general two different contact angles α_l and α_r. Along with assuming an incompressible substrate, we note that the tangential force contribution (2.28) is zero, however we note that since the droplet contact angles will differ from Young's angle θ_Y due to the elastic deformation at the wetting ridge, we will observe tangential contact line forces f_l and f_r given by

$$f_{l,r} = \gamma(\cos\alpha_{l,r} - \cos\theta_Y).$$

This gives stress boundary conditions at the free surface given by

$$\tau_{xz}|_{z=h} = f_l\delta(x+R) - f_r\delta(x-R) + k^2\Upsilon\partial_{xx}u|_{z=h} \tag{5.3}$$

$$\tau_{zz}|_{z=h} = \gamma\sin\alpha_l\delta(x+R) + \gamma\sin\alpha_r\delta(x-R) - \Pi H(R-|x|) + \Upsilon\partial_{xx}w|_{z=h} \tag{5.4}$$

In these equations $f_{l,r}$ refers to the tangential contact line force, γ is the fluid surface stress, $\alpha_{l,r}$ is the left and right contact angles, R is the projected radius of the droplet onto the substrate surface, Π is the fluid pressure underneath the droplet, and δ and H are respectively the Dirac-delta and Heaviside distributions.

The solution to our model equation $\nabla \cdot \bar{\tau} = \mathbf{0}$ with stress boundary conditions (5.3), (5.4) at the free surface $z = h$ and fixed boundary conditions $u(x,0) = w(x,0) = 0$ at the base of the substrate for each given substrate gradient will result in asymmetric deformation of the substate ultimately resulting in a contact angle asymmetry. Adopting the assumption by [43] that the difference in contact angle governs the onset of motion of the droplet, we will investigate the ability of each

gradient in creating a contact angle asymmetry and predict the conditions for which this asymmetry will cause droplet motion.

First we will employ a Fourier transform approach analogous to that shown in Ch. 3 for the symmetric two dimensional geometry. The method is generalized allowing for asymmetric contact angles and deformation. Next we will introduce numerical computations utilizing the Finite Element Method to replicate results for the substrate deformation. For each method, we will generate the deformation results for given contact angles $\alpha_{l,r}$ and show that they quantitatively agree with each other.

Next we compute the elastic energy in the substrate for the given deformation field. From this a total energy functional is created comprised of the elastic and surface energies, and from the energy functional we can numerically solve for the static contact angles $\alpha_{l,r}$ that will minimize this total energy of the system with the aid of MATLAB's optimization toolbox. Ultimately we proceed with the Fourier transform approach to predict the static configuration of the droplet and predict conditions for which droplet motion would be induced for each substrate gradient.

The droplet configuration characterized by the contact angles α_l and α_r that minimizes the total energy will then be recorded for example cases presented in 5.7. These cases investigate the ability of each gradient to cause sufficient contact angle asymmetry to induce droplet motion. Recording the conditions for which droplet motion is induced according to the simulations presented in this chapter, a model to predict the magnitude of the droplet velocity is presented in Ch. 6.

5.1   Stiffness Gradient

In this section we outline the static asymmetric two dimensional solution to the model for the case of a gradient in elastic shear modulus G. To study the deformation of the substrate with a gradient in elastic modulus, we prescribe a modulus of the form

$$G(x) = \bar{G} + a\tilde{G}(x) \qquad \tilde{G}(x) = \frac{2}{\pi}\arctan(x/L) \tag{5.5}$$

where $\bar{G}$ is the average modulus, a is a small parameter such that the total variation of the modulus G is much less than the average modulus $\bar{G}$ ($|2a| \ll \bar{G}$), and L is the length scale over which the modulus gradient is influential. In order to solve the model equations $\partial_j \tau_{ij} = 0$, we utilize an expansion in small parameter a and apply a Fourier transform in the horizontal direction on the scale separated boundary value problems. Transforming the separated boundary value problems to Fourier space we will then solve for the transformed displacements and apply the inverse Fourier transform to obtain the substrate deformation.

Expanding variables with respect to small parameter a we have $u \approx u_0 + a\, u_1$ (and similarly for w and p). Iterating each equation in the force balance equation $\partial_j \tau_{ij} = 0$ we obtain governing model equations

$$\partial_x \tau_{xx} + \partial_z \tau_{xz} = \quad 0 \tag{5.6a}$$

$$\partial_x \tau_{xz} + \partial_z \tau_{zz} = \quad 0 \tag{5.6b}$$

Expanding the horizontal balance equation (5.6a) using stess tensor (5.1), incompressibility condition (5.2) and definition of the shear modulus (5.5), we get

$$
\begin{aligned}
\partial_x \tau_{xx} + \partial_z \tau_{xz} &= \partial_x\big(2G(x)\partial_x u - p\big) + \partial_z\big(G(x)\big(\partial_x w + \partial_z u\big)\big) \\
&= \partial_x\big(2\bar{G}\partial_x u_0 - p_0 + a\big(2\tilde{G}(x)\partial_x u_0 - p_1 + 2\bar{G}\partial_x u_1\big)\big) \\
&\quad + \bar{G}\big(\partial_{xz} w_0 + \partial_{zz} u_0\big) + a\tilde{G}\big(\partial_{xz} w_0 + \partial_{zz} u_0\big) + a\bar{G}\big(\partial_{xz} w_1 + \partial_{zz} u_1\big) + \mathcal{O}(a^2) \\
&= \bar{G}\big(2\partial_{xx} u_0 + \partial_{xz} w_0 + \partial_{zz} u_0\big) - \partial_x p_0 \\
&\quad + a\Big[\tilde{G}(x)\big(2\partial_{xx} u_0 + \partial_{xz} w_0 + \partial_{zz} u_0\big) + \bar{G}\big(2\partial_{xx} u_1 + \partial_{xz} w_1 + \partial_{zz} u_1\big) \\
&\quad + 2\tilde{G}'(x)\partial_x u_0 - \partial_x p_1\Big] + \mathcal{O}(a^2) \\
&= \bar{G}\Delta u_0 - \partial_x p_0 + a\Big[\tilde{G}(x)\Delta u_0 + \bar{G}\Delta u_1 + 2\tilde{G}'(x)\partial_x u_0 - \partial_x p_1\Big] + \mathcal{O}(a^2) = 0.
\end{aligned}
$$

Similarly with the vertical balance equation (5.6b) we get

$$
\begin{aligned}
\partial_x \tau_{xz} + \partial_z \tau_{zz} &= \partial_x\big(G(x)\big(\partial_x w + \partial_z u\big)\big) + \partial_z\big(2G(x)\partial_z w - p\big) \\
&= \partial_x\big(\bar{G}\big(\partial_x w_0 + \partial_z u_0\big) + a\tilde{G}(x)\big(\partial_z w_0 + \partial_x u_0\big) + a\bar{G}\big(\partial_z w_1 + \partial_x u_1\big)\big) \\
&\quad + 2\bar{G}\partial_{zz} w_0 - \partial_z p_0 + 2a\tilde{G}(x)\partial_{zz} w_0 + 2a\bar{G}\partial_{zz} w_1 + \mathcal{O}(a^2) \\
&= \bar{G}\big(2\partial_{zz} w_0 + \partial_{xx} w_0 + \partial_{xz} u_0\big) - \partial_z p_0 \\
&\quad + a\Big[\tilde{G}(x)\big(2\partial_{zz} w_0 + \partial_{xx} w_0 + \partial_{xz} u_0\big) + \bar{G}\big(2\partial_{zz} w_1 + \partial_{xx} w_1 + \partial_{xz} u_1\big) \\
&\quad + \tilde{G}'(x)\big(\partial_x w_0 + \partial_z u_0\big) - \partial_z p_1\Big] \\
&= \bar{G}\Delta w_0 - \partial_z p_0 + a\Big[\tilde{G}(x)\Delta w_0 + \bar{G}\Delta w_1 + \tilde{G}'(x)\big(\partial_x w_0 + \partial_z u_0\big)\Big] + \mathcal{O}(a^2) = 0
\end{aligned}
$$

Comparing terms of the same magnitude we obtain scale separated boundary value problems, a zero order symmetric boundary value problem:

$$\partial_x p_0 = \bar{G}\Delta u_0 \tag{5.7a}$$

$$\partial_z p_0 = \bar{G}\Delta w_0 \tag{5.7b}$$

$$\left[\bar{G}(\partial_z u_0 + \partial_x w_0) - k^2\Upsilon\partial_{xx} u_0\right]_{z=h} = f_l\delta(x+R) - f_r\delta(x-R) \tag{5.7c}$$

$$\left[2\bar{G}\partial_z w_0 - p_0 - \Upsilon\partial_{xx} w_0\right]_{z=h} = \gamma\left(\sin\alpha_l\delta(x+R) + \sin\alpha_r\delta(x-R)\right) - \Pi H(R-|x|) \tag{5.7d}$$

and a first order antisymmetric boundary value problem:

$$\partial_x p_1 = \bar{G}\Delta u_1 + \tilde{G}\Delta u_0 + 2\tilde{G}'\partial_x u_0 \tag{5.8a}$$

$$\partial_z p_1 = \bar{G}\Delta w_1 + \tilde{G}\Delta w_0 + \tilde{G}'(\partial_x w_0 + \partial_z u_0) \tag{5.8b}$$

$$\left[\bar{G}(\partial_z u_1 + \partial_x w_1) - k^2\Upsilon\partial_{xx} u_1\right]_{z=h} = -\left[\tilde{G}(\partial_z u_0 + \partial_x w_0)\right]_{z=h} \tag{5.8c}$$

$$\left[2\bar{G}\partial_z w_1 - p_1 - \Upsilon\partial_{xx} w_1\right]_{z=h} = -\left[2\tilde{G}\partial_z w_0\right]_{z=h} \tag{5.8d}$$

In both these boundary value problems (5.7), (5.8) we preserve the incompressibility condition (5.2) at each scale $\partial_x u_k + \partial_z w_k = 0$ for $k = 0,1$. Boundary conditions (5.7c), (5.7d), (5.8c) and (5.8d) come from the scale separation of (5.3) and (5.4) by small parameter a.

In this chapter we define the Fourier transform pair to be

$$\mathscr{F}[f(x)] = \int_{-\infty}^{\infty} f(x)e^{-isx}dx = \hat{f}(s)$$

$$\mathscr{F}^{-1}[\hat{f}(s)] = \frac{1}{2\pi}\int_{-\infty}^{\infty} \hat{f}(s)e^{isx}ds = f(x).$$

With derivative and convolution properties respectively given by

$$\mathscr{F}[f'(x)] = is\hat{f}(s) \qquad \text{and} \qquad \mathscr{F}[f(x)g(x)] = \frac{1}{2\pi}\hat{f}(s) * \hat{g}(s)$$

Here we derive the transform of the derivative of perturbation $\tilde{G}(x)$:

$$\tilde{G}'(x) = \frac{2}{\pi}\frac{L}{x^2 + L^2}$$

$$\mathscr{F}[\tilde{G}'(x)] = \frac{2L}{\pi}\int_{-\infty}^{\infty} \frac{e^{-isx}}{x^2 + L^2}dx$$

66

Using contour integration in the complex plane, we note that there are poles at $\xi = \pm i L$. Considering semicircular positively oriented path integrals, we note that for $s > 0$ the magnitude of function

$$f(\xi) = \frac{e^{-i s \xi}}{\xi^2 + L^2}$$

approaches zero as $|\xi| \to \infty$, $\Im(\xi) < 0$ and is unbounded for $|\xi| \to \infty$, $\Im(\xi) > 0$. Integrating the positively oriented curve consisting of real line segment $-r < \Re(\xi) = x < r$ and the semicircle in the negative imaginary portion of the complex plane of radius r, taking $r \to \infty$ we obtain (for $s > 0$):

$$\frac{2L}{\pi} \int_{-\infty}^{\infty} \frac{e^{-i s x}}{x^2 + L^2} d x = \frac{2L}{\pi} \left(-2\pi i \operatorname{Res}[f, -i L] \right) = -4 i L \frac{e^{-s L}}{-2 i L} = 2 e^{-s L}.$$

Similarly, for $s < 0$ we get that $|f| \to 0$ as $|\xi| \to \infty$, $\Im(\xi) > 0$ and is unbounded for $|\xi| \to \infty$, $\Im(\xi) < 0$. Using the upper half semicircle we obtain (for $s < 0$):

$$\frac{2L}{\pi} \int_{-\infty}^{\infty} \frac{e^{-i s x}}{x^2 + L^2} d x = \frac{2L}{\pi} \left(2\pi i \operatorname{Res}[f, i L] \right) = 4 i L \frac{e^{s L}}{2 i L} = 2 e^{s L}.$$

This gives us transform

$$\mathscr{F}\left[\tilde{G}'(x)\right] = 2 e^{-|s| L}. \tag{5.9}$$

Because $\tilde{G}(x)$ has average value 0, we can utilize the derivative identity to obtain transform of the perturbation $\tilde{G}(x)$:

$$\mathscr{F}\left[\tilde{G}(x)\right] = \frac{2 e^{-|s| L}}{i s} \tag{5.10}$$

Transforming the system equations in the zero order BVP (5.7) we obtain:

$$i s \hat{p}_0 = \bar{G}(\partial_{zz} - s^2) \hat{u}_0$$

$$\partial_z \hat{p}_0 = \bar{G}(\partial_{zz} - s^2) \hat{w}_0$$

therefore we have that

$$i s \partial_z \hat{p}_0 = \bar{G}(\partial_{zz} - s^2) \partial_z \hat{u}_0 = i s \bar{G}(\partial_{zz} - s^2) \hat{w}_0.$$

Transforming the scaled equation (5.2) we have that

$$\mathscr{F}\left[\varepsilon_{kk}\right] = i s \hat{u}_0 + \partial_z \hat{w}_0 = 0 \quad \Rightarrow \quad \hat{u}_0 = \frac{i}{s} \partial_z \hat{w}_0.$$

which results in

$$(\partial_{zz} - s^2) \frac{i}{s} \partial_{zz} \hat{w}_0 = i s (\partial_{zz} - s^2) \hat{w}_0$$

$$\Rightarrow (\partial_{zz} - s^2)^2 \, \hat{w}_0 = 0.$$

This is familiar from Ch. 3 as the resulting ODE for the transformed biharmonic potential $\hat{\Psi}$. Using standard solution to this ODE shown previously (3.23) and applying fixed boundary conditions at $z = 0$, we obtain general solution form for $\hat{w}_0$ and from the incompressibility condition (5.2) we obtain solution for $\hat{u}_0$ and $\hat{w}_0$:

$$\hat{u}_0(s, z) = i C_0(s) \psi'(sz) + i D_0(s) \psi''(sz) \tag{5.11a}$$

$$\hat{w}_0(s, z) = C_0(s) \psi(sz) + D_0(s) \psi'(sz) e \, x \tag{5.11b}$$

where

$$\psi(\xi) = -\sinh(\xi) + \xi \cosh(\xi) \qquad \psi'(sz) = \frac{d}{d\xi} \psi(\xi)|_{\xi = sz} = s^{-1} \partial_z \psi(sz)$$

and $C_0(s)$, $D_0(s)$ are Fourier coefficients that will be defined by applying the shear and normal boundary conditions given by (5.3), (5.4). Transforming these boundary conditions gives us the following system of equations

$$C_0(s) \beta(s) + D_0(s) \beta'(s) = M_0(s) \tag{5.12a}$$

$$C_0(s) \mu(s) + D_0(s) \mu'(s) = N_0(s) \tag{5.12b}$$

where the right hand sides to (5.12) are defined as

$$M_0(s) = (f_r + f_l) \sin s R + i (f_r - f_l) \cos s R$$

$$N_0(s) = \gamma (\sin \alpha_l + \sin \alpha_r) \cos s R + i \gamma (\sin \alpha_l - \sin \alpha_r) \sin s R - 2\Pi \frac{\sin s R}{s}$$

resulting from the Fourier transform of the capillary forces in the tangential and normal directions respectively, and coefficient functions are given by:

$$\beta(s) = \bar{G} s \big(\psi(sh) + \psi''(sh) \big) + k^2 \Upsilon s^2 \psi'(sh)$$

$$\beta'(s) = \bar{G} s \big(\psi'(sh) + \psi'''(sh) \big) + k^2 \Upsilon s^2 \psi''(sh)$$

$$\mu(s) = \bar{G} s \big(3\psi'(sh) - \psi'''(sh) \big) + \Upsilon s^2 \psi(sh)$$

$$\mu'(s) = \bar{G} s \big(3\psi''(sh) - \psi''''(sh) \big) + \Upsilon s^2 \psi'(sh)$$

Solving for the Fourier coefficients $C_0(s)$ and $D_0(s)$ in (5.12) we obtain the zero order displacement transforms $\hat{u}_0(s, z)$ and $\hat{w}_0(s, z)$ identical to the incompressible case from Ch. 3. Applying the transform to the first order correction BVP (5.8) we obtain:

$$i s \hat{p}_1 = \bar{G} (\partial_{zz} - s^2) \hat{u}_1 + \frac{1}{2\pi} \Big[\mathscr{F}\big[\tilde{G}\big] * \big((\partial_{zz} - s^2) \hat{u}_0 \big) + 2\mathscr{F}\big[\tilde{G}'\big] * (i s \hat{u}_0) \Big]$$

and
$$\partial_z \hat{p}_1 = \bar{G}(\partial_{zz} - s^2)\hat{w}_1 + \frac{1}{2\pi}\Big[\mathscr{F}[\tilde{G}] * \big((\partial_{zz} - s^2)\hat{w}_0\big) + \mathscr{F}[\tilde{G}'] * \big(i s \hat{w}_0 + \partial_z u_0\big)\Big]$$

resulting in equality

$$\Rightarrow i s \partial_z \hat{p}_1 = \bar{G}(\partial_{zz} - s^2)\partial_z \hat{u}_1 + \frac{1}{2\pi}\Big[\mathscr{F}[\tilde{G}] * \big((\partial_{zz} - s^2)\partial_z \hat{u}_0\big) + 2\mathscr{F}[\tilde{G}'] * (i s \partial_z \hat{u}_0)\Big]$$

$$= i s \bar{G}(\partial_{zz} - s^2)\hat{w}_1 + i s \frac{1}{2\pi}\Big[\mathscr{F}[\tilde{G}] * \big((\partial_{zz} - s^2)\hat{w}_0\big) + \mathscr{F}[\tilde{G}'] * \big(i s \hat{w}_0 + \partial_z u_0\big)\Big]$$

From this we manipulate the above expression to obtain a nonhomogeneous ODE for the first order correction terms:

$$(\partial_{zz} - s^2)^2 \hat{w}_1 = \Phi(s, z) = \frac{i s}{2\pi \bar{G}}\Big[-2\mathscr{F}[\tilde{G}'] * \big((\partial_{zz} - s^2)\hat{w}_0\big) + \big(s\mathscr{F}[\tilde{G}']\big) * \big(s^{-1}(\partial_{zz} + s^2)\hat{w}_0\big)\Big] \quad (5.13)$$

where again due to the incompressibility condition (5.2) we have that $\hat{u}_1 = i s^{-1}\partial_z \hat{w}_1$. Solving for the fundamental solution f to the transformed biharmonic operator we have that

$$(\partial_{zz} - s^2)f = \delta(z)$$

$$\Rightarrow \mathscr{L}[f] = \frac{1}{(k^2 - s^2)^2}$$

$$\Rightarrow f(z) = \mathscr{L}^{-1}\Big[\frac{1}{(k^2 - s^2)^2}\Big] = \frac{1}{2s^3}\psi(s z)$$

where $\mathscr{L}$ is the Laplace transform with respect to variable z:

$$\mathscr{L}[f(z)] = \int_0^\infty f(z)e^{-kz} \, dz$$

From this we obtain solutions for transformed first order deformations $\hat{u}_1$ and $\hat{w}_1$:

$$\hat{u}_1 = i C_1(s)\psi'(s z) + i D_1(s)\psi''(s z) + i \hat{F}_1(s, z) \qquad (5.14\text{a})$$

$$\hat{w}_1 = C_1(s)\psi(s z) + D_1(s)\psi'(s z) + \hat{F}_0(s, z) \qquad (5.14\text{b})$$

where

$$\hat{F}_k(s, z) = \frac{1}{2s^3}\int_0^z \Phi(s, z - \xi)\psi^{(k)}(s\xi) \, d\xi. \qquad (k = 0, 1, 2, 3)$$

69

In this formulation $\hat{F}_k(s,z)$, the order of integration is switched and we obtain alternative definition for the non-homogeneous solution to the first order correction terms:

$$\hat{F}_k(s,z) = \frac{i}{4\pi\bar{G}s^2}\int_{-\infty}^{\infty}\left[-2\mathscr{F}[\tilde{G}']\chi\left[(\partial_{zz}-s^2)\hat{w}_0,\psi^{(k)}\right]+\left(s\mathscr{F}[\tilde{G}']\right)\chi\left[s^{-1}(\partial_{zz}+s^2)\hat{w}_0,\psi^{(k)}\right]\right]d\eta \quad (5.15)$$

where operator χ is defined as

$$\chi\left[g(\eta,z),\psi^{(k)}(sz)\right] = \int_0^z g(\eta,z-\xi)\psi^{(k)}(s\xi)\,d\xi$$

Specifically, we obtain formulas

$$\chi\left[(\partial_{zz}-s^2)\hat{w}_0,\psi^{(k)}\right] = 2\eta^2 C_0(\eta)\int_0^z \sinh\left(\eta(z-\xi)\right)\psi^{(k)}(s\xi)\,d\xi$$

$$+2\eta^2 D_0(\eta)\int_0^z \cosh\left(\eta(z-\xi)\right)\psi^{(k)}(s\xi)\,d\xi$$

and

$$\chi\left[s^{-1}(\partial_{zz}+s^2)\hat{w}_0,\psi^{(k)}\right] = 2\eta^2 C_0(\eta)\int_0^z (z-\xi)\cosh\left(\eta(z-\xi)\right)\psi^{(k)}(s\xi)\,d\xi$$

$$+2\eta D_0(\eta)\int_0^z \cosh\left(\eta(z-\xi)\right)\psi^{(k)}(s\xi)\,d\xi + 2\eta^2 D_0(\eta)\int_0^z (z-\xi)\sinh\left(\eta(z-\xi)\right)\psi^{(k)}(s\xi)\,d\xi$$

where the integrals above are calculated analytically using Mathematica. Transforming the boundary conditions (5.8c) and (5.8d), we obtain respectively we get system

$$C_1(s)\beta(s) + D_1(s)\beta'(s) = M_1(s) \quad\quad (5.16a)$$

$$C_1(s)\mu(s) + D_1(s)\mu'(s) = N_1(s) \quad\quad (5.16b)$$

where

$$M_1(s) = \frac{i}{2\pi}\left[\left(\frac{\mathscr{F}[\tilde{G}']}{s}\right)*\left(s^{-1}(\partial_{zz}+s^2)\hat{w}_0\right)\right]_{z=h} - \bar{G}s\left[\hat{F}_2(s,h)+\hat{F}_0(s,h)\right] - k^2\Upsilon s^2\hat{F}_1(s,h)$$

$$N_1(s) = \frac{i}{2\pi}\left[2\left(\frac{\mathscr{F}[\tilde{G}']}{s}\right)*\partial_z\hat{w}_0 - s^{-1}\left(\frac{\mathscr{F}[\tilde{G}']}{s}\right)*\left(s^{-1}(\partial_{zz}-s^2)\partial_z\hat{w}_0\right)+2s^{-1}\mathscr{F}[\tilde{G}']*\partial_z\hat{w}_0\right]_{z=h}$$

$$-\bar{G}s\left[3\hat{F}_1(s,h)-\hat{F}_3(s,h)\right]-\Upsilon s^2\hat{F}_0(s,h)$$

The solution to the linear system (5.16) fully defines both our antisymmetric first order correction BVP (5.8), allowing us to define our transformed displacements $\hat{u}$ and $\hat{w}$ and thus calculate stresses

and strains within the solid substrate. These calculations will be used in §5.6 where the elastic energy of the system will be calculated and the minimum system energy configuration of the droplet will be obtained by choosing contact angles α_l and α_r such that this energy is minimized.

5.2 Surface Energy Gradient

In this section we outline the solution to the model equations for the case of a gradient in solid surface energy γ_s as opposed to a gradient in substrate stiffness G outlined in §5.1. Under our assumptions we have that $\Upsilon(x) = \gamma_s(x)$, and we prescribe a perturbation similar to that in the previous section §5.1:

$$\Upsilon(x) = \bar{\Upsilon} + a\tilde{\Upsilon}(x) \qquad \tilde{\Upsilon}(x) = \frac{2}{\pi}\arctan(x/L) \tag{5.17}$$

where $\bar{\Upsilon}$ is the average surface energy, a is again the small parameter such that the total variation in surface energy is much less than the average surface energy ($|2a| \ll \bar{\Upsilon}$), and L is the length over which the gradient is influential. Again we expand with respect to small parameter a. In this section we hold the shear modulus G constant.

Using a similar method as in the last section, we have scale separated BVPs:

$$\partial_x p_0 = G\Delta u_0 \tag{5.18a}$$

$$\partial_z p_0 = G\Delta w_0 \tag{5.18b}$$

$$\left[G(\partial_z u_0 + \partial_x w_0) - k^2\bar{\Upsilon}\partial_{xx}u_0\right]_{z=h} = f_l\delta(x+R) - f_r\delta(x-R) \tag{5.18c}$$

$$\left[2G\partial_z w_0 - p_0 - \bar{\Upsilon}\partial_{xx}w_0\right]_{z=h} = \gamma\left(\sin\alpha_l\delta(x+R) + \sin\alpha_r\delta(x-R)\right) - \Pi H(R - |x|) \tag{5.18d}$$

and

$$\partial_x p_1 = G\Delta u_1 \tag{5.19a}$$

$$\partial_z p_1 = G\Delta w_1 \tag{5.19b}$$

$$\left[G(\partial_z u_1 + \partial_x w_1) - k^2\bar{\Upsilon}\partial_{xx}u_1\right]_{z=h} = \left[k^2\tilde{\Upsilon}\partial_{xx}u_0\right]_{z=h} \tag{5.19c}$$

$$\left[2G\partial_z w_1 - p_1 - \bar{\Upsilon}\partial_{xx}w_1\right]_{z=h} = \left[\tilde{\Upsilon}\partial_{xx}w_0\right]_{z=h} \tag{5.19d}$$

In this case, both of the scale separated equations have identical homogeneous PDE systems (5.18a),(5.18b) and (5.19a),(5.19b). The solution to this, outlined in §5.1, gives general solution to transformed displacements $\hat{u}$ and $\hat{w}$:

$$\hat{u}_j(s,z) = iC_j(s)\psi'(sz) + iD_j(s)\psi''(sz)$$
$$\hat{w}_j(s,z) = C_j(s)\psi(sz) + D_j(s)\psi'(sz)$$

for $j = 1, 2$.

The zero order boundary value problem is identical to that of §5.1, with resulting linear system to solve for Fourier coefficients $C_0(s)$, $D_0(s)$ given by (5.12). Solving for the first order Fourier coefficients is done by transforming boundary conditions (5.19c), (5.19d) as follows:

$$i C_1(s)\beta(s) + i D_1(s)\beta'(s) = \mathscr{F}\left[k^2 \tilde{\Upsilon} \partial_{xx} u_0\right]_{z=h}$$
$$= -k^2 \frac{1}{2\pi} \mathscr{F}\left[\tilde{\Upsilon}\right] * \left(s^2 \hat{u}_0\right)_{z=h}$$
$$= -k^2 \frac{1}{2\pi} \left(\frac{\mathscr{F}\left[\tilde{\Upsilon}'\right]}{s}\right) * \left(s \partial_z \hat{w}_0\right)_{z=h}$$

and

$$C_1(s)\mu(s) + D_1(s)\mu'(s) = \mathscr{F}\left[\tilde{\Upsilon} \partial_{xx} w_0\right]_{z=h}$$
$$= -\frac{1}{2\pi} \mathscr{F}\left[\tilde{\Upsilon}\right] * \left(s^2 \hat{w}_0\right)_{z=h}$$
$$= \frac{i}{2\pi} \left(\frac{\mathscr{F}\left[\tilde{\Upsilon}'\right]}{s}\right) * \left(s^2 \hat{w}_0\right)_{z=h}$$

This gives us a linear system of equations to evaluate first order Fourier coefficients $C_1(s)$, $D_1(s)$ given by:

$$C_1(s)\beta(s) + C_2(s)\beta'(s) = M_1(s) \tag{5.20a}$$
$$C_1(s)\mu(s) + C_2(s)\mu'(s) = N_1(s) \tag{5.20b}$$

where $M_1(s)$, $N_1(s)$ are given by

$$M_1(s) = \frac{i k^2}{2\pi} \left(\frac{\mathscr{F}\left[\tilde{\Upsilon}'\right]}{s}\right) * \left(s \partial_z \hat{w}_0\right)_{z=h}$$

$$N_1(s) = \frac{i}{2\pi} \left(\frac{\mathscr{F}\left[\tilde{\Upsilon}'\right]}{s}\right) * \left(s^2 \hat{w}_0\right)_{z=h}$$

As in §5.1, this now defines the solution to our first order correction BVP (5.19), allowing us to calculate deformations as well as stresses and strains within the substrate which will be applied to the energy calculations outlined in §5.6.

5.3 Finite Element Method

In this section we aim to solve the model equations $\partial_j \tau_{ij} = 0$ with a substrate gradient as in the previous two sections §5.1 and §5.2, but utilizing the Finite Element Method as opposed to the analytic transform methods outlined previously. In §5.4, the results of the two methods are compared showing agreement in the deformation solutions.

The setup for our Finite Element method will differ slightly from the problems defined in §5.1 and §5.2. Notably we will use a linear gradient in both stiffness and surface energy for this section, different from the smooth perturbation used for the transform methods. In addition, we will work on a finite domain

$$\Omega = \{(x, z) \in \mathbb{R}^2 \mid -l/2 < x < l/2, 0 < z < h\}$$

with boundary

$$\partial\Omega = \Gamma = \Gamma_1 \cup \Gamma_2$$

where Γ_1 is the solid free surface upon which the droplet rests and Γ_2 is the base of the gel at $z = 0$ as well as the two vertical edges at the far boundaries $x = \pm l/2$. We define our shear and normal stresses along the boundary Γ_1 as we do in the previous sections:

$$\tau_{xz}|_{\Gamma_1} = f_l \delta(x + R) - f_r \delta(x - R) + k^2 \Upsilon \partial_{xx} u|_{\Gamma_1}$$

$$\tau_{zz}|_{\Gamma_1} = \gamma \sin\alpha_l \delta(x + R) + \gamma \sin\alpha_r \delta(x - R) - \Pi H(R - |x|) + \Upsilon \partial_{xx} w|_{\Gamma_1}$$

where $f_{l,r}$ are the left and right tangential contact line forces, k is the approximate slope of the vertical displacement at the wetting ridge, γ is the surface tension of the droplet, $\alpha_{l,r}$ are the left and right contact angles of the droplet and Υ is the solid surface stress.

We seek to express the force balance condition in Ω in its weak form in order to apply the finite element approximation to solve for the deformation in the substrate. The force balance equations (5.6) are a system of second order elliptic partial differential equations with respect to the displacements. We define our set of test functions

$$\Phi = \{\phi(x, z) \mid \phi \in H^1(\Omega), \phi|_{\Gamma_2} = 0\}$$

Then for any test function $\phi \in \Phi$, we have

$$\iint_\Omega \phi\left(\partial_x \tau_{xx} + \partial_z \tau_{xz}\right) d\Omega = 0 \tag{5.21}$$

$$\iint_\Omega \phi\left(\partial_x \tau_{xz} + \partial_z \tau_{zz}\right) d\Omega = 0 \tag{5.22}$$

Manipulating (5.21) we get

$$
\begin{aligned}
\iint_\Omega \phi\left(\partial_x \tau_{xx} + \partial_z \tau_{xz}\right) d\Omega &= \int_0^h \left[\int_{-l/2}^{l/2} \phi \partial_x \tau_{xx}\, dx\right] dz + \int_{-l/2}^{l/2} \left[\int_0^h \phi \partial_z \tau_{xz}\, dz\right] dx \\
&= \int_0^h \left[-\int_{-l/2}^{l/2} \partial_x \phi \tau_{xx}\, dx\right] dz \\
&\quad + \int_{-l/2}^{l/2} \left[\phi \tau_{xz}|_{z=h} - \int_0^h \partial_z \phi \tau_{xz} \phi\, dz\right] dx \\
&= \int_{\Gamma_1} \phi \tau_{xz}\, dx - \iint_\Omega \left(\partial_x \phi \tau_{xx} + \partial_z \phi \tau_{xz}\right) d\Omega = 0 \\
\Rightarrow \iint_\Omega \left(\partial_x \phi \tau_{xx} + \partial_z \phi \tau_{xz}\right) d\Omega &= \int_{\Gamma_1} \phi \tau_{xz}\, dx \tag{5.23}
\end{aligned}
$$

and manipulating (5.22) we get

$$
\begin{aligned}
\iint_\Omega \phi\left(\partial_x \tau_{xz} + \partial_z \tau_{zz}\right) d\Omega &= \int_0^h \left[\int_{-l/2}^{l/2} \phi \partial_x \tau_{xz}\, dx\right] dz + \int_{-l/2}^{l/2} \left[\int_0^h \phi \partial_z \tau_{zz}\, dz\right] dx \\
&= \int_0^h \left[-\int_{-l/2}^{l/2} \partial_x \phi \tau_{xz}\, dx\right] dz \\
&\quad + \int_{-l/2}^{l/2} \left[\phi \tau_{zz}|_{z=h} - \int_0^h \partial_z \phi \tau_{zz} \phi\, dz\right] dx \\
&= \int_{\Gamma_1} \phi \tau_{zz}\, dx - \iint_\Omega \left(\partial_x \phi \tau_{xz} + \partial_z \phi \tau_{zz}\right) d\Omega = 0 \\
\Rightarrow \iint_\Omega \left(\partial_x \phi \tau_{xz} + \partial_z \phi \tau_{zz}\right) d\Omega &= \int_{\Gamma_1} \phi \tau_{zz}\, dx \tag{5.24}
\end{aligned}
$$

Using our stress tensor $\tau_{ij} = 2G\varepsilon_{ij} - p\delta_{ij}$, we have the following:

$$\iint_\Omega \partial_x \phi(2G\partial_x u - p) + \partial_z \phi G(\partial_z u + \partial_x w)\, d\Omega = \int_{\Gamma_1} \phi \tau_{xz}\, dx$$

and

$$\iint_\Omega \partial_x \phi G(\partial_z u + \partial_x w) + \partial_z \phi(2G\partial_z w - p)\, d\Omega = \int_{\Gamma_1} \phi \tau_{zz}\, dx$$

74

for which we can evaluate the right hand sides from the assigned stress boundary conditions:

$$\int_{\Gamma_1} \phi \tau_{xz} \, dx = \int_{\Gamma_1} \phi \left(f_l \delta(x+R) - f_r \delta(x-R) + k^2 \Upsilon \partial_{xx} u \right) dx$$

$$= f_l \phi(-R, h) - f_r \phi(R, h) - k^2 \int_{\Gamma_1} \partial_x (\Upsilon \phi) \partial_x u \, dx$$

and

$$\int_{\Gamma_1} \phi \tau_{zz} \, dx = \int_{\Gamma_1} \phi \left(\gamma \sin \alpha_l \delta(x+R) + \gamma \sin \alpha_r \delta(x-R) - \Pi H(R-|x|) + \Upsilon \partial_{xx} w \right) dx$$

$$= \gamma \sin \alpha_l \phi(-R, h) + \gamma \sin \alpha_r \phi(R, h) - \Pi \int_{-R}^{R} \phi(x, h) \, dx - \int_{\Gamma_1} \partial_x (\Upsilon \phi) \partial_x w \, dx$$

Giving us integral formulations defined by the shear and normal boundary conditions:

$$\iint_{\Omega} \partial_x \phi (2G\partial_x u - p) + \partial_z \phi G(\partial_z u + \partial_x w) \, d\Omega + k^2 \int_{\Gamma_1} \partial_x (\Upsilon \phi) \partial_x u \, dx = f_l \phi(-R, h) - f_r \phi(R, h) \tag{5.25}$$

and

$$\iint_{\Omega} \partial_x \phi G(\partial_z u + \partial_x w) + \partial_z \phi (2G\partial_z w - p) \, d\Omega + \int_{\Gamma_1} \partial_x (\Upsilon \phi) \partial_x w \, dx$$

$$= \gamma \sin \alpha_l \phi(-R, h) + \gamma \sin \alpha_r \phi(R, h) - \Pi \int_{-R}^{R} \phi(x, h) \, dx \tag{5.26}$$

We then generate nodes throughout the domain Ω, concentrating nodes around the contact line locations. A sample mesh is depicted in Fig. 5.1 utilizing MATLAB commands `initmesh` to generate a uniform mesh fitting the geometry and `refinemesh` to make locations such as the contact line more densely packed with nodes. In addition to concentrating nodes about the contact line location, nodes are generally more densely packed around the top surface as deformations are larger here than deep into the substrate.

We then define global basis functions depicted in Fig. 5.2. Each node, located at (x_i, z_i) is assigned its own basis function ϕ_i such that $\phi_i(x_j, z_k) = \delta_{ij}\delta_{ik}$, and is piecewise continuous. We then define our approximate solutions

$$u(x, z) \approx \sum_{j=1}^{N} u_j \phi_j(x, z) \qquad w(x, z) \approx \sum_{j=1}^{N} w_j \phi_j(x, z) \qquad p(x, z) \approx \sum_{j=1}^{N} p_j \phi_j(x, z) \tag{5.27}$$

which gives us approximations at nodes $u_j \approx u(x_j, z_j)$, $w_j \approx w(x_j, z_j)$ and $p_j \approx p(x_j, z_j)$. Here N corresponds to the number of nontrivial nodes, or nodes $(x_j, z_j) \in \Omega \cup \Gamma_1$.
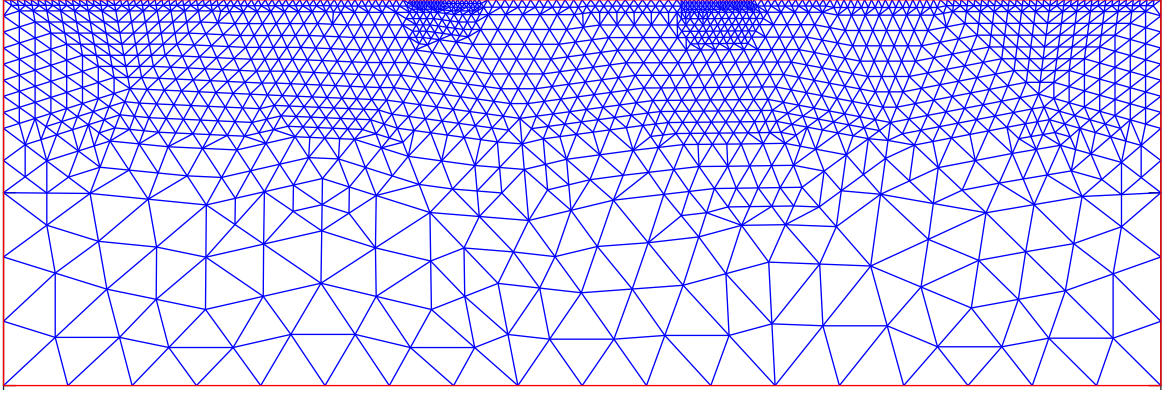
Figure 5.1 Example mesh generated for $l = 300\,\mu$m, $h = 100\,\mu$m and $R = \sqrt{2000/\pi}\,\mu$m. Large concentration of nodes placed around contact line positions as seen at top surface.
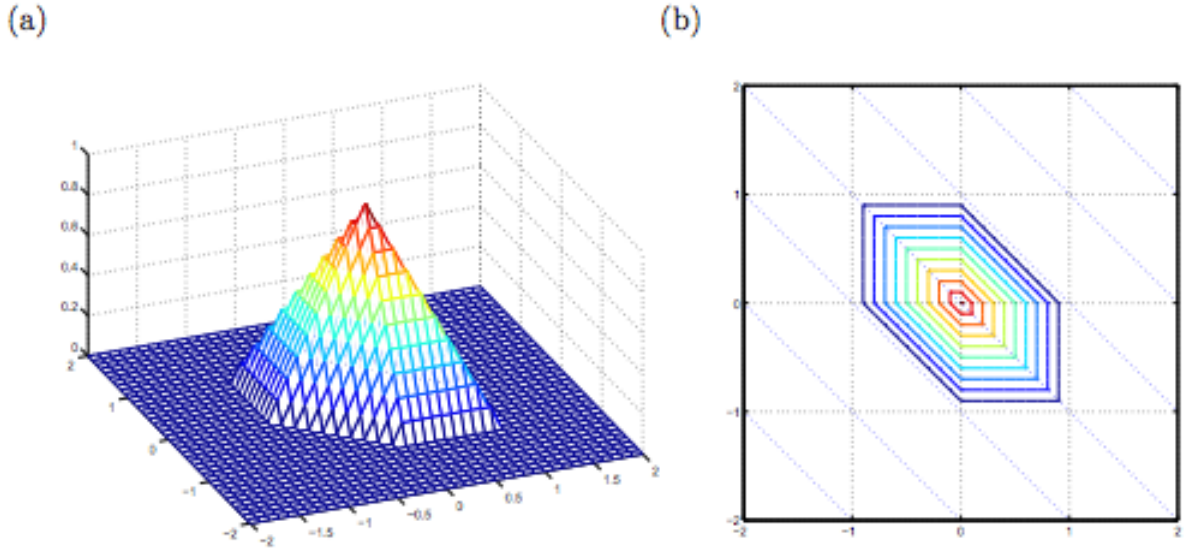

Figure 5.2 Example test function which is equal to one at a node, zero at all other nodes, and is piecewise linear continuous. Figure Credit: Numerical Solutions of Partial Differential Equations, Dr. Zhilin Li

Substituting the approximations (5.27) into the integral formulations (5.25), (5.26), we obtain

$$\sum_{j=1}^{N} u_j \left[\iint_{\Omega} G\left(2\partial_x\phi_i\partial_x\phi_j + \partial_z\phi_i\partial_z\phi_j\right) d\Omega + k^2 \int_{\Gamma_1} \partial_x(\Upsilon\phi_i)\partial_x\phi_j \, dx \right]$$

$$+ \sum_{j=1}^{N} w_j \left[\iint_{\Omega} G\partial_z\phi_i\partial_x\phi_j d\Omega \right] + \sum_{j=1}^{N} p_j \left[-\iint_{\Omega} \partial_x\phi_i\phi_j \, d\Omega \right]$$

76

$$= f_l \phi_i(-R, h) - f_r \phi_i(R, h) \tag{5.28}$$

and

$$\sum_{j=1}^{N} w_j \left[\iint_\Omega G\left(\partial_x \phi_i \partial_x \phi_j + 2\partial_z \phi_i \partial_z \phi_j\right) d\Omega + \int_{\Gamma_1} \partial_x(\Upsilon \phi_i) \partial_x \phi_j \, dx \right]$$

$$+ \sum_{j=1}^{N} u_j \left[\iint_\Omega G\partial_x \phi_i \partial_z \phi_j d\Omega \right] + \sum_{j=1}^{N} p_j \left[-\iint_\Omega \partial_z \phi_i \phi_j \, d\Omega \right]$$

$$= \gamma \sin \alpha_l \phi_i(-R, h) + \gamma \sin \alpha_r \phi_i(R, h) - \Pi \int_{-R}^{R} \phi_i(x, h) \, dx \tag{5.29}$$

We then supplement these equations (5.28), (5.29) with the weak form expression of the incompressibility condition (5.2):

$$\varepsilon_{kk} = \partial_x u + \partial_z w = 0$$

$$\Rightarrow \quad (\forall \phi \in \Phi) \quad \iint_\Omega \phi\left(\partial_x u + \partial_z w\right) d\Omega = 0$$

$$\Rightarrow \sum_{j=1}^{N} u_j \left[\iint_\Omega \phi_i \partial_x \phi_j \, d\Omega \right] + \sum_{j=1}^{N} w_j \left[\iint_\Omega \phi_i \partial_z \phi_j \, d\Omega \right] = 0 \tag{5.30}$$

The deformation $\{u_i\}_1^N$ and $\{w_i\}_1^N$ approximations as well as the hydrostatic pressure approximations $\{p_i\}_1^N$ are then vectorized and placed into a sparse linear system with stiffness matrix and right-hand side vector governed by the formulas (5.28), (5.29), (5.30):

$$\begin{bmatrix} [S^u] & [S^w] & [S^p] \\ [N^u] & [N^w] & [N^p] \\ [C^u] & [C^w] & [0] \end{bmatrix} \begin{bmatrix} \vec{u} \\ \vec{w} \\ \vec{p} \end{bmatrix} = \begin{bmatrix} \vec{f}^u \\ \vec{f}^w \\ \vec{0} \end{bmatrix} \tag{5.31}$$

where sub-matrices of the stiffness matrix are defined as

$$S_{ij}^u = \iint_\Omega G\left(2\partial_x\phi_i\partial_x\phi_j + \partial_z\phi_i\partial_z\phi_j\right) d\Omega + k^2 \int_{\Gamma_1} \partial_x(\Upsilon\phi_i)\partial_x\phi_j \, dx$$

$$S_{ij}^w = \iint_\Omega G\partial_z\phi_i\partial_x\phi_j d\Omega$$

$$S_{ij}^p = -\iint_\Omega \partial_z\phi_i\phi_j \, d\Omega$$

$$N_{ij}^u = \iint_\Omega G\partial_x\phi_i\partial_z\phi_j d\Omega$$

$$N_{ij}^w = \iint_\Omega G\left(\partial_x\phi_i\partial_x\phi_j + 2\partial_z\phi_i\partial_z\phi_j\right) d\Omega + \int_{\Gamma_1} \partial_x(\Upsilon\phi_i)\partial_x\phi_j \, dx$$

$$N_{ij}^p = -\iint_\Omega \partial_z\phi_i\phi_j \, d\Omega$$

$$C_{ij}^u = \iint_\Omega \phi_i\partial_x\phi_j \, d\Omega$$

$$C_{ij}^w = \iint_\Omega \phi_i\partial_z\phi_j \, d\Omega$$

and

$$f_i^u = f_l\phi_i(-R,h) - f_r\phi_i(R,h)$$

$$f_i^w = \gamma\sin\alpha_l\phi_i(-R,h) + \gamma\sin\alpha_r\phi_i(R,h) - \Pi\int_{-R}^R \phi_i(x,h) \, dx$$

Where we note that for the integrals above, in general the integrands are linear with respect to x and z. Here we apply exact quadrature rule for integration of planes over triangular domain:

$$\iint_{\Omega_t} a + bx + cz \, d\Omega_t = A(\Omega_t)(a + b\bar{x} + c\bar{z})$$

where $A(\Omega_t)$ is the area of triangular region Ω_t, and $\bar{x}$, $\bar{z}$ are the average x and z values of the triangle vertices. The stiffness matrix and right hand side vector from (5.31) are then generated and the solution vector is obtained by row reduction.

With the system (5.31) defined as outlined and inverted, we obtain our approximate solutions $\{u_i\}_1^N$, $\{w_i\}_1^N$ and $\{p_i\}_1^N$ from which we can calculate stresses and strains just as in §5.1 and §5.2.

5.4   Deformation Results for Fourier Transform and Finite Element Methods

Here we plot a few cases of comparison for the two methods outlined thus far in the chapter. We can see overall good quantitative agreement between the Fourier Transform method and the Finite Element method. Differences in the graphs can be attributed to the slightly different forms of gradients present in the problem different domains. In Fig. 5.3 we see a comparison of the horizontal and vertical deformation using Fourier Transform method and the Finite Element method.

5.5   Asymmetric Droplet Shape

In the methods outlined previously in the chapter in §5.1, §5.2 and §5.3, we can obtain the deformation field within the substrate for a given set of parameters and thus the strains and stresses within the substrate to obtain the elastic and total system energies outlined in §5.6. We allow for the contact angle parameters α_l and α_r to be defined such that the choice of contact angles minimizes the total system energy. In order to compute the total system energy which is comprised of both solid and liquid surface energies and elastic energy in the substrate due to the elastic deformation of the gel, we need to construct a total energy functional as a function of left and right contact angles α_l and α_r.

From the deformation calculations we are able to calculate the elastic energy as well as the solid surface energy in §5.6. However we are left unable to calculate the liquid surface energy without obtaining the arc length of the droplet, for which the shape would deviate from a circular cap for a droplet with asymetric contact angles. Here we assume the peaks of the wetting ridge are approximately equal, and we calculate the arc length of a droplet with a fixed volume given two contact angles α_l and α_r. For $\alpha_{l,r} < 90°$, we have that the droplet profile f can be expressed in cartesian coordinates obeying the differential equation given in [14]:

$$-\gamma\kappa(x) + \mu x = \Pi \tag{5.32}$$

where $-\gamma\kappa(x)$ is the Laplace pressure of the droplet, μx represents the work done to displace the center of mass of the droplet from $x = 0$ and Π is the total pressure at the surface under the droplet. Solving this equation gives the shape of a two dimensional droplet with specific body force μ acting tangent to the surface, such as a droplet resting on an incline affected by gravity. Integrating this with respect to x we obtain expression

$$\frac{\mu}{2}x^2 - \Pi x + C = \gamma\frac{f'(x)}{\sqrt{1 + (f'(x))^2}} \tag{5.33}$$
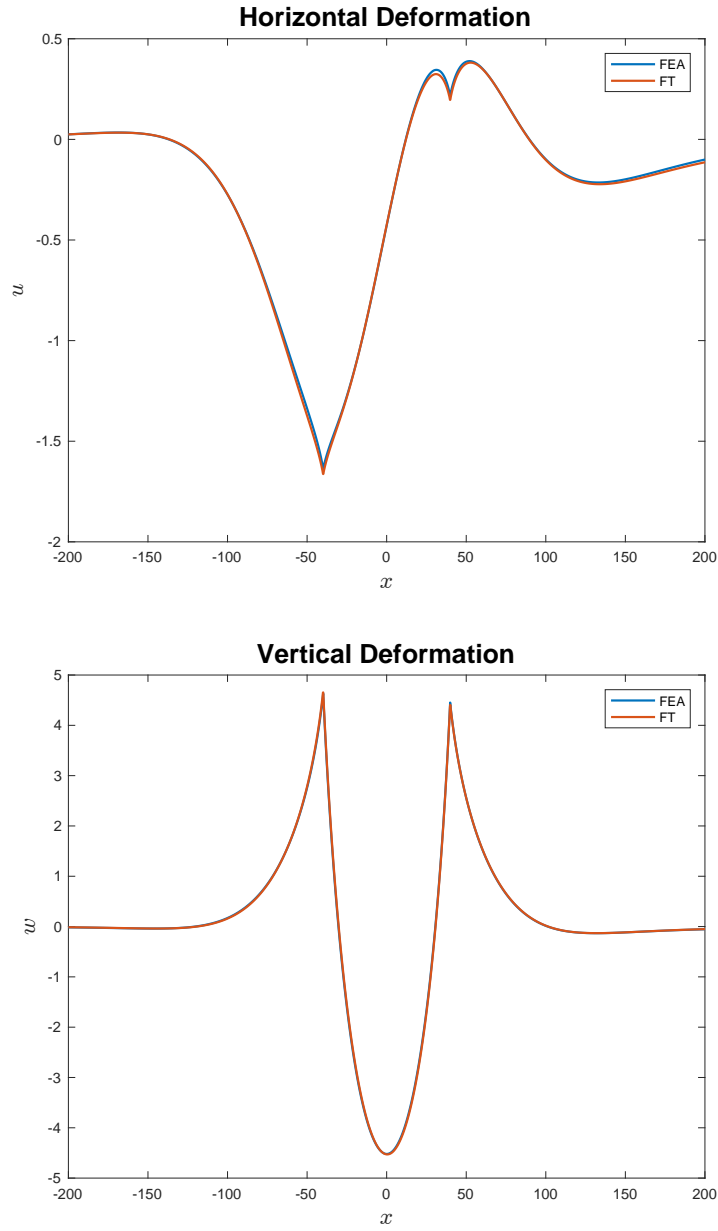
Figure 5.3 Deformation results for $\alpha_l = \pi/2 + .03$ (outward pull), $\alpha_r = \pi/2 - .03$ (inward pull). Surface horizontal deformation u pictured above and surface vertical deformation w depicted below. Comparison of the two techniques shows good agreement in solution between the two methods, where as differences can be attributed to finite domain effects for the FEA method as well as the gradient. The FEA method uses a linear gradient, while the transform method uses the arc tangent gradient.

By applying boundary conditions $f'(-R) = \tan\alpha_r$ and $f'(R) = -\tan\alpha_l$ we obtain system of equations

$$\frac{\mu}{2}R^2 + \Pi R + C = \gamma\sin\alpha_l$$

$$\frac{\mu}{2}R^2 - \Pi R + C = -\gamma\sin\alpha_r$$

where we can solve for the pressure Π by subtracting the bottom equation from the top to obtain

$$\Pi = \gamma\frac{\sin\alpha_l + \sin\alpha_r}{2R}, \tag{5.34}$$

which is consistent with the symmetric case where $\alpha_l = \alpha_r = \alpha$. Continuing with the acute contact angle case we can also solve for integration constant C and manipulate expression (5.33) to obtain

$$f'(x) = \frac{F(x/R)}{\sqrt{1 - (F(x/R))^2}}$$

$$F(\xi) = \frac{1}{2}\left[\frac{\mu R^2}{\gamma}(\xi^2 - 1) - \left(\sin\alpha_l + \sin\alpha_r\right)\xi + \sin\alpha_l - \sin\alpha_r\right] \tag{5.35}$$

Using substitution $\tilde{x} = x/R$ we then define the solution the this by incorporating the endpoint position boundary conditions to obtain droplet profile

$$\frac{f(\tilde{x})}{R} = \int_{-1}^{\tilde{x}} \frac{F(\xi)}{\sqrt{1 - (F(\xi))^2}}d\xi \qquad \text{such that} \quad f(1) = 0 \tag{5.36}$$

A bisection algorithm is employed to obtain dimensionless parameter $\mu R^2/\gamma$ that satisfies the position condition at $\tilde{x} = 1$. Once this is obtained we then calculate the dimensionless height as a function of $\tilde{x}$. Specifying a fixed area A, we then can calculate the radius R by integrating the non-dimensional droplet profile.

$$R = \sqrt{\frac{A}{\int_{-1}^{1}(f(\tilde{x})/R)\, d\tilde{x}}}$$

We can then calculate the arc length of the droplet using

$$L_{drop} = R\int_{-1}^{1} \frac{1}{\sqrt{1 - (F(\xi))^2}}d\xi, \tag{5.37}$$

To solve for the general case for which either or both of the contact angles exceed 90°, we must extend the solution to (5.32) to polar coordinates. We take the total pressure Π to be given by (5.34).

We then convert (5.32) to polar coordinates, where after nondimensionalization by R we obtain:

$$\frac{2(r'(\theta))^2+(r(\theta))^2-r(\theta)r''(\theta)}{\left((r'(\theta))^2+(r(\theta))^2\right)^{3/2}}+\frac{\mu R^2}{\gamma}r(\theta)\cos\theta=\frac{\Pi R}{\gamma} \tag{5.38}$$

Taking initial conditions from $\theta=0$ given by $r(0)=1$ and $r'(0)=-\cot\alpha_r$, the differential equation in polar coordinates is converted to a first order system and solved using MATLAB's `ode45` by minimizing a functional containing penalty constraints for solutions that do not match the boundary conditions $r(\pi/2)=1$ and $r'(\pi/2)=\cot\alpha_l$.

Now having solution for $r(\theta)$ of the liquid profile in polar coordinates, we compute the arc length

$$L_{drop}=R\int_0^\pi\sqrt{r^2+(r')^2}\,d\theta \tag{5.39}$$

Now having defined the arc length for a general droplet (5.39), we can obtain the surface energy associated with the liquid-gas interface:

$$\mathscr{E}_{lg}=\gamma L_{drop}$$

With this remaining calculation above, we can fully define our system energy as the sum of surface interfacial energy and elastic energy, where solid interfacial energy is calculated from deformation results from §5.1, §5.2 and §5.3 and liquid-gas surface energy calculated as outlined in this section. The total system energy is then calculated and minimized in the analysis to follow in §5.6.

5.6 Elastic Energy and the Total Energy Functional

In this section we outline the procedure to calculate the total system energy as a function of contact angles α_l and α_r by the culmination of work thus far in the chapter. We then utilize MATLAB's optimization program `fminsearch` to calculate the minimum energy configuration of the droplet and obtain contact angle asymmetry predictions based on system parameters and the magnitude of the gradient applied to the substrate.

Ultimately we abandon the Finite Element solution method at this point, leaving it to validate our deformation results for the Fourier transform method with substrate gradients in surface energy and shear modulus. Though the elastic energy is convenient to calculate simply using the elastic energy definition (5.40) with our piecewise defined strain field approximation, ultimately the energy calculation had too much noise for the sensitive minimization of total energy via adjusting contact angles α_l and α_r. The source of the noise coming from the slight adjustment in contact angles

leading to slight adjustments in contact line location, where moving the node location associated with the contact line altered the mesh in the local area of the contact line sufficient enough to cause slight numerical fluctuations around the location for which

$$\nabla_\alpha \mathcal{E}_{total} = \vec{0} \qquad \nabla_\alpha = \langle \partial_{\alpha_l}, \partial_{\alpha_r} \rangle.$$

Where the Finite Element model fails, the Fourier transform methods outlined in §5.1 and §5.2 succeed in creating a smooth energy field as a function of contact angles α_l and α_r allowing reliable prediction of the contact angles for which minimize the total system energy.

Elastic energy in the substrate is computed by the following integration over the solid domain:

$$\mathcal{E}_{elastic} = \frac{1}{2} \iint_\Omega \bar{\tau} \cdot \bar{\varepsilon} \, d\Omega \tag{5.40}$$

where manipulating the integrand gives us

$$\begin{aligned}
\bar{\tau} \cdot \bar{\varepsilon} &= \tau_{xx} \varepsilon_{xx} + 2\tau_{xz} \varepsilon_{xz} + \tau_{zz} \varepsilon_{zz} \\
&= (2G\varepsilon_{xx} - p)\varepsilon_{xx} + 4G\varepsilon_{xz}^2 + (2G\varepsilon_{zz} - p)\varepsilon_{zz} \\
&= 2G(\varepsilon_{xx}^2 + 2\varepsilon_{xz}^2 + \varepsilon_{zz}^2) - p(\varepsilon_{xx} + \varepsilon_{zz}).
\end{aligned}$$

Due to incompressibility of the solid we have $\varepsilon_{xx} = -\varepsilon_{zz}$ resulting in $\varepsilon_{xx}^2 = \varepsilon_{zz}^2$. Using this we simplify the integrand in (5.40) to:

$$\begin{aligned}
\bar{\tau} \cdot \bar{\varepsilon} &= 4G(\varepsilon_{zz}^2 + \varepsilon_{xz}^2) \\
&= G\big(4(\partial_z w)^2 + (\partial_z u + \partial_x w)^2\big)
\end{aligned}$$

$$\Rightarrow \mathcal{E}_{elastic} = \frac{1}{2} \iint_\Omega G\big(4(\partial_z w)^2 + (\partial_z u + \partial_x w)^2\big) \, d\Omega$$

For the transform methods, we convert the x-integral to Fourier space by

$$\int_{-\infty}^{\infty} f(x) \, dx = \mathscr{F}\big[f(x)\big]_{s=0} = \hat{f}(0)$$

which allows us to write the elastic energy in terms of known Fourier transforms of deformations $\hat{u}$, $\hat{w}$ as well as $\mathscr{F}[\tilde{G}]$ along with convolution identity to obtain:

$$\mathcal{E}_{elastic} = \frac{1}{2} \int_0^h \mathscr{F}\Big[G\big[4(\partial_z w)^2 + (\partial_z u + \partial_x w)^2\big]\Big]_{s=0} dz$$

$$= \frac{1}{4\pi} \int_0^h \Big[\mathscr{F}[G] * \mathscr{F}\big[4(\partial_z w)^2 + (\partial_z u + \partial_x w)^2\big]\Big]_{s=0} dz$$

$$\mathcal{E}_{elastic} = \frac{1}{4\pi} \int_0^h \Big[\big(\bar{G} + \frac{a}{2\pi}(\mathscr{F}[\tilde{G}]*)\big)\big[4\big((\partial_z \hat{w})*(\partial_z \hat{w})\big) + \big((\partial_z \hat{u} + is\hat{w})*(\partial_z \hat{u} + is\hat{w})\big)\big]\Big]_{s=0} dz \quad (5.41)$$

Note that in the case that we employ the surface energy gradient as opposed to the stiffness gradient as outlined in general above, that (5.41) reduces to

$$\mathcal{E}_{elastic} = \frac{G}{4\pi} \int_0^h \Big[4\big((\partial_z \hat{w})*(\partial_z \hat{w})\big) + \big((\partial_z \hat{u} + is\hat{w})*(\partial_z \hat{u} + is\hat{w})\big)\Big]_{s=0} dz$$

The total energy of the system is given by the combination of elastic and surface energies, where the latter is calculated by the arc lengths of each phase interfaces multiplied by their respective surface energies. The total energy functional is calculated as

$$\mathcal{E}_{total} = \mathcal{E}_{elastic} + \mathcal{E}_{surface}$$

where the surface energy functional is given by

$$\mathcal{E}_{surface} = \gamma L_{drop} + \int_{-\infty}^{\infty} \Upsilon\Big[\sqrt{(1 + \partial_x u|_{z=h})^2 + (\partial_x w|_{z=h})^2} - 1\Big] dx, \quad (5.42)$$

The integral in the above equation (5.42) represents the finite change in solid surface energy from an undeformed state as opposed to the infinite total surface energy associated with an infinite domain.

The integrand of elastic energy (5.41) is then numerically constructed via the outlined procedures in §5.1 and §5.2 where the deformation and strain transforms are approximated. The integrand of (5.41) is constructed by performing the convolutions numerically, then integrated with over the depth of the substrate. Similarly, the surface energy functional (5.42) is calculated by first inverting the surface deformation transforms to obtain solid interface shape. From this the solid energy is calculated and liquid-gas interfacial energy is calculated by (5.39). Example results are plotted in §5.7.

5.7   Results

The total energy minimization outlined in §5.6 was done for typical ideal but physically realistic sets of parameters which could be experimentally tested. Varying mean values of stiffness $\bar{G}$ and surface energy $\bar{\Upsilon}$ for the stiffness gradient and surface energy gradient simulations respectively, we ran the minimization algorithm outlined in §5.6 and computed the contact angle difference $\Delta\alpha = \alpha_l - \alpha_r$ as seen in Fig. 5.4. This is then compared to the benchmark contact angle difference from Style *et al*[43] of $\Delta\alpha = 1.8°$ necessary to drive droplet motion to obtain the necessary gradient for each mean value of stiffness $\bar{G}$ or surface energy $\bar{\Upsilon}$.

In Fig. 5.4, we observe that the stiffness gradient is less effective than the surface energy gradient in driving the contact angle asymmetry to the threshold level for inducing droplet motion. We conclude that the stiffness gradient is likely a physically unrealistic method for driving droplet motion. From the plot we can see that only the lowest average modulus of $\bar{G} = 1$ kPa is successful in generating a contact angle difference sufficient to drive droplet motion according the the benchmark threshold of $1.8°$ within the window provided, needing over a 50% variation ($|a|/\bar{G} > 0.5$, $L \approx 1.5R$) in modulus to reach this threshold. We are concerned about both the accuracy of the expansion method outlined in §5.1 which relies on small parameter a to be small relative to the average modulus $\bar{G}$, as well as the feasibility to create such a large gradient in such a soft material.

In [10], by inter-diffusing soft gel networks of different moduli, they are able to produce a total variation in modulus of approximately 90% over roughly 10 cm with average modulus $\bar{G} \approx 35$ kPa. Both the length of this interval as well as the magnitude of the shear modulus, as indicated by our results, are insufficient to drive droplet motion. Similarly, using gradients in ultra-violet intensity to cure PDMS gels, as discussed in [40], is incapable of creating a modulus gradient large enough to drive motion of a fluid droplet. Though it is possible to make substrates such as silicone gels with shear modulus $G = 1$ kPa, to the best of our knowledge, experimental methods to alter the stiffness of the gel are limited to those mentioned from [10, 40]. This suggests that advances must be made to create substrates which exhibit both extremely soft elastic moduli as well as sharp moduli gradients to make motion induced by a substrate gradient attainable.

On the contrary, the capability to generate a contact angle asymmetry using a surface energy gradient is experimentally feasible. In [9], by exposing the surface to the diffusing front of a vapor of decyltrichlorosilane ($Cl_3Si(CH_2)_9CH_3$), a gradient in solid surface energy was generated causing a contact angle asymmetry of 6-8°. This contact angle asymmetry was sufficient to cause droplets of water to migrate uphill on a rigid surface. Though for rigid substrates, the dominant form of resistance to motion is dissipation within the fluid. In Ch. 6 we discuss the phenomena of viscoelastic
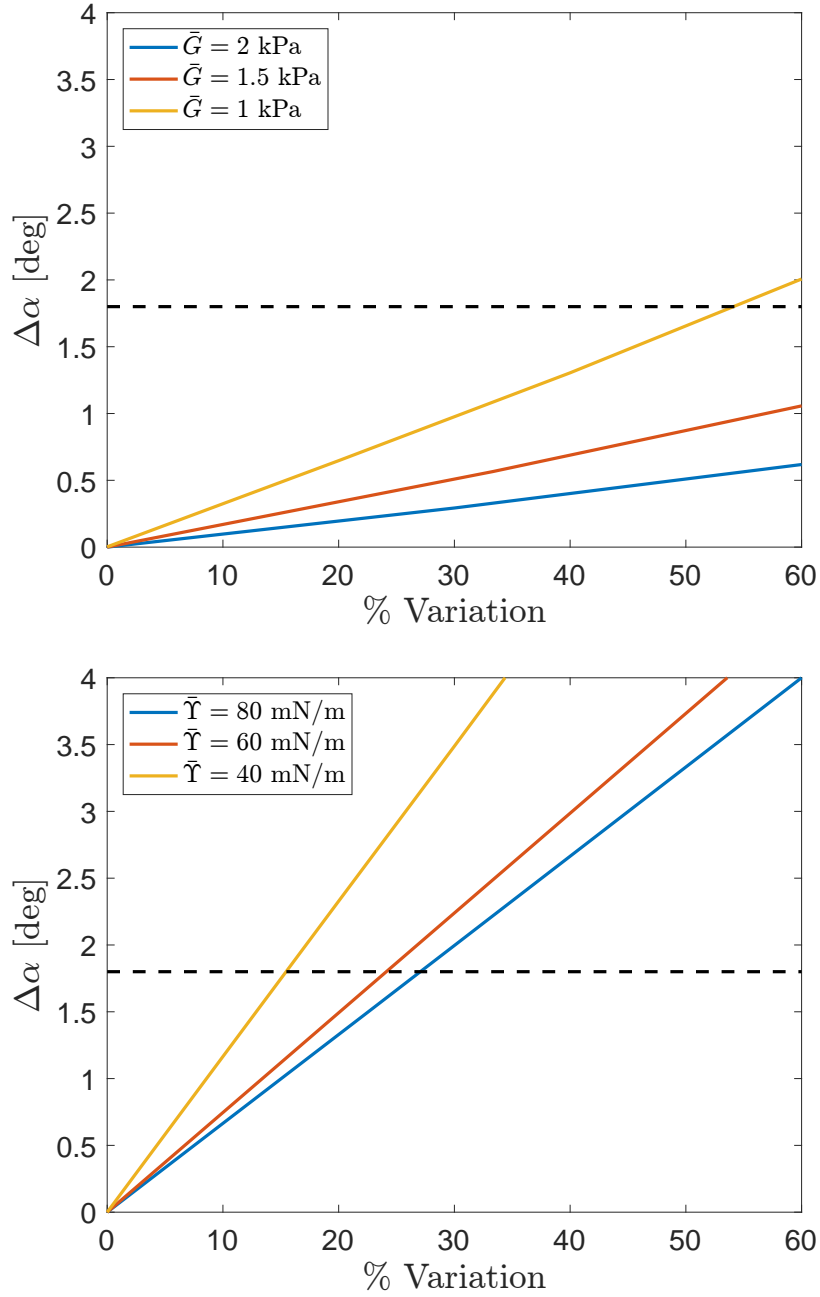
Figure 5.4 Plot of contact angle asymmetry $\Delta\alpha = \alpha_l - \alpha_r$ as function of % variation of elastic shear modulus $|a|/\bar{G} \times 100\%$ for various average shear modulus $\bar{G}$ (top) and as function of % variation of surface energy $|a|/\bar{\Upsilon} \times 100\%$ (bottom). We observe that lower elastic moduli are more feasible in reaching the contact angle threshold of 1.8° (black dotted line). Parameters: $h = 50\ \mu$m, $A = 600\pi\ \mu$m^2, $\gamma = 64$ mN/m.

breaking [35], which for soft motion over soft solids, the main resistance to motion comes in the form of viscoelastic dissipation. Despite this, supplying asymmetry of the magnitude capable by methods in [9] is sufficient to meet the benchmark asymmetry threshold of 1.8° [43]. The predicted velocities of the onset motion from results presented here will be discussed in Ch. 6.

CHAPTER

6

ENERGY DISSIPATION AND DROPLET VELOCITY MODEL

In this chapter we outline the model for predicting droplet velocity based on our results from Ch. 5. This prediction comes from calculating the rate at which total energy is released from the system and equating this to the rate at which energy is dissipated from the substrate at a given velocity. Using the criteria for predicting droplet motion outlined in Ch. 5, we then seek the velocity of the droplet that releases system energy at the same rate at which elastic energy is dissipated in the solid substrate.

First in §6.1 we outline the procedure for obtaining the deformation field of the substrate caused by a two dimensional droplet migrating at velocity v across the substrate surface. Then in §6.2, using this model from §6.1 we calculate the elastic energy contained in the substrate necessary for computing the rate at which energy either is accumulated or released from the system as the droplet migrates with given velocity v. Next in §6.3, the computation of the elastic energy dissipation is introduced and calculated using our transformed stresses and strains obtained from the moving droplet model in §6.1. From here the velocity v such that the rate of energy release matches the rate of energy dissipation is calculated giving us velocity predictions for droplets migrating across soft substrates driven by stiffness or surface energy gradients. These results are given in §6.4.

Throughout the chapter, we use the solid dissipation as an approximation for the total energy

dissipation of the system, neglecting dissipation within the droplet. For rigid substrates, there would be no solid dissipation and the energy sink for a moving droplet is indeed the dissipation within the fluid. This is discussed in [26] where using the lubrication approximation as well as approximating the flow within the droplet as a Poiseuille flow, the fluid dissipation P_{drop} is given approximately as [26]:

$$\mathscr{P}_{drop} = \frac{3v^2 \eta_L \ln r}{\alpha} \tag{6.1}$$

where η_L is the viscosity of the liquid and r is the ratio of the projected droplet radius R to a microscopic length scale ($\ln r$ is typically of $\mathcal{O}(10)$), and α being the contact angle of the advancing contact line. In experiments by [35] studying motion of droplets over soft rubber showed that motion is slower by several orders of magnitude compared to droplets on rigid surfaces. Another finding was that the kinetics was independent of liquid viscosity [35]. This phenomena, coined viscoelastic braking [35], attributes the change in dynamics to the dominant form of dissipation being from the solid as opposed to the liquid. The work done by Long *et al* [26] as well as our results will illustrate that this is true, allowing us to approximate the total dissipation with that dissipated within the solid.

6.1   Moving Droplet Model

We now explore the scenario of a droplet migrating across the surface of a substrate. In the case of a stiffness gradient, it is more energetically favorable for the droplet to rest on a stiffer region of the substrate. While in the case of a surface energy gradient it is more favorable to rest on a region of lower surface energy. In order for the droplet to move, the excess energy of motion must be exceeded by the energy released from migration. We aim to calculate the energy dissipated within the solid to represent the cost of droplet motion and compare this to the rate of energy released by droplet motion. We adopt the dynamic stress tensor given in [20]:

$$\tau_{ij}(x, z, t) = 2 \int_{-\infty}^{t} \zeta(x, z, t - t') \dot{\varepsilon}_{ij}(x, z, t') \, dt' - p(x, z, t) \delta_{ij} \tag{6.2}$$

where ζ is the relaxatiion function of the solid. For a reticulated polymer such as silicone gel, the response function obeys the power law form [20]:

$$\zeta(x, z, t) = G(x) \left(1 + \frac{(t/t_v)^{-n}}{\Gamma(1-n)} \right) \tag{6.3}$$

where $G(x)$ is the static shear modulus, t_v is the viscous time scale, $n > 0$ is a fitting exponent and Γ is the Gamma function. Note that the Gamma function evaluation $\Gamma(1-n)$ could be absorbed into the viscous time scale t_v, but for future calculations we will continue with this given form. Also

note that (6.2) simplifies approximately to our static stress tensor when t is much larger than any instance $t' \in (-\infty, t)$, $t' \ll t$ which had a nonzero strain rate $\dot{\varepsilon} \neq 0$, making relative time $(t - t')/t_v$ large and relaxation function (6.3) approaches the static shear modulus G.

We introduce a temporal Fourier transform similar to the spatial transform defined previously:

$$\mathscr{F}_t\big[f(x,t)\big] = \int_{-\infty}^{\infty} f(x,t)e^{-i\omega t}\,dt = \check{f}(x,\omega)$$

with inverse similarly defined:

$$\mathscr{F}_t^{-1}\big[\check{f}(x,\omega)\big] = \frac{1}{2\pi}\int_{-\infty}^{\infty} \check{f}(x,\omega)e^{i\omega t}\,dt = f(x,t)$$

and further use of the spatial Fourier transform will be denoted by $\mathscr{F}_x\big[\,\cdot\,\big]$ or the ^ symbol. For simplicity of notation we will write a twice transformed variable with a capital letter, ie:

$$\mathscr{F}_x\big[\mathscr{F}_t[f(x,t)]\big] = \mathscr{F}_t\big[\mathscr{F}_x[f(x,t)]\big] = F(s,\omega)$$

Applying the temporal Fourier transform to (6.2) we obtain

$$
\begin{aligned}
\check{\tau}_{ij} &= 2\int_{-\infty}^{\infty}\int_{-\infty}^{t} \zeta(t-t')\dot{\varepsilon}_{ij}(t')\,dt'\,e^{-i\omega t}\,dt - \check{p}\,\delta_{ij} \\
&= 2\int_{-\infty}^{\infty} \dot{\varepsilon}_{ij}(t')\int_{t'}^{\infty} \zeta(t-t')e^{-i\omega t}\,dt\,dt' - \check{p}\,\delta_{ij} \\
&= 2\int_{-\infty}^{\infty} \dot{\varepsilon}_{ij}(t')e^{-i\omega t'}\int_{0}^{\infty} \zeta(t)e^{-i\omega t}\,dt\,dt' - \check{p}\,\delta_{ij} \\
&= 2\Big[i\omega\int_{0}^{\infty} \zeta(t)e^{-i\omega t}\,dt\Big]\check{\varepsilon}_{ij} - \check{p}\,\delta_{ij}
\end{aligned}
$$

From this we define complex shear modulus $g(x,\omega)$ given by [20]:

$$g(x,\omega) = i\omega\int_{0}^{\infty} \zeta\, e^{-i\omega t}\,dt = G(x)\big(1 + (i\omega t_v)^n\big) \tag{6.4}$$

This gives us a familiar form for the temporally transformed stress tensor:

$$\check{\tau}_{ij} = 2g(x,\omega)\check{\varepsilon}_{ij} - \check{p}\,\delta_{ij} \tag{6.5}$$

To adapt the solution to a moving droplet, we consider a droplet moving at a constant velocity $v > 0$. The stress boundary conditions are rewritten in terms of moving reference frame $x' = x - vt$:

$$\tau_{xz}(x', h) = f_l \delta(x' + R) - f_r \delta(x' - R) + k^2 \Upsilon \partial_{xx} u(x', h) \tag{6.6}$$

$$\tau_{zz}(x', h) = \gamma \sin \alpha_l \delta(x' + R) + \gamma \sin \alpha_r \delta(x' - R) - \Pi H(R - |x'|) + \Upsilon \partial_{xx} w(x', h) \tag{6.7}$$

We consider a quasi-static solution for the displacement in the substrate as done in [20]:

$$\partial_j \tau_{ij} = 0 \quad \Rightarrow \quad \mathscr{F}_t[\partial_j \tau_{ij}] = \partial_j \check{\tau}_{ij} = 0$$

with stress boundary conditions (6.6), (6.7) at the free surface $z = h$ along with fixed boundary conditions at the bottom surface $z = 0$. From here-on we proceed with the zero order solution for the displacements as the rate of change of these will dominate those in the first order correction. We have then our boundary value problem formed by the fixed boundary conditions at $z = 0$, stress boundary conditions given by (6.6), (6.7) and manipulation of the quasi-static divergence free stress tensor above, presented in temporally transformed space:

$$\partial_x \check{p} = \bar{g} \Delta \check{u} \tag{6.8a}$$

$$\partial_z \check{p} = \bar{g} \Delta \check{w} \tag{6.8b}$$

$$\left[\bar{g}(\partial_z \check{u} + \partial_x \check{w}) - k^2 \tilde{\Upsilon} \partial_{xx} \check{u} \right]_{z=h} = \mathscr{F}_t \left[f_l \delta(x' + R) - f_r \delta(x' - R) \right] \tag{6.8c}$$

$$\left[2\bar{g} \partial_z \check{w} - \check{p} - \tilde{\Upsilon} \partial_{xx} \check{w} \right]_{z=h} = \mathscr{F}_t \left[\gamma \left(\sin \alpha_l \delta(x' + R) + \sin \alpha_r \delta(x' - R) \right) - \Pi H(R - |x'|) \right] \tag{6.8d}$$

where $\bar{g}$ is the spatially averaged complex shear modulus:

$$\bar{g}(\omega) = G(0) \left(1 + (i \omega t_v)^n \right)$$

Assuming the rate at which energy is injected into the system is constant and balanced exactly by the dissipation, the solutions to the moving boundary value problem (6.8) will be traveling wave solutions with constant velocity v. To solve (6.8), we investigate the properties of a function f in the

moving reference frame when Fourier transforms are applied in both time and space:

$$F(s,\omega) = \mathscr{F}_t\Big[\mathscr{F}_x\big[f(x-vt)\big]\Big]$$

$$= \mathscr{F}_t\left[\int_{-\infty}^{\infty} f(x-vt)e^{-isx}\,dx\right]$$

$$= \mathscr{F}_t\left[e^{-isvt}\int_{-\infty}^{\infty} f(x)e^{-isx}\,dx\right]$$

$$= \mathscr{F}_t\big[e^{-isvt}\hat{f}(s)\big]$$

$$= \hat{f}(s)\int_{-\infty}^{\infty} e^{-isvt}e^{-i\omega t}\,dt$$

$$= 2\pi\hat{f}(s)\delta(\omega+sv) \tag{6.9}$$

where $\hat{f}(s)$ is the spatial Fourier transform of f in the moving reference frame. Then applying the spatial Fourier transform to (6.8) we obtain the familiar differential equation encountered in Chs. 3 and 5:

$$\left(\frac{d^2}{dz^2}-s^2\right)^2 W = 0 \qquad U = \frac{i}{s}\partial_z W$$

which when solved and applying the fixed boundary conditions gives us general solution

$$U(s,\omega,z) = iC(s,\omega)\psi'(sz) + iD(s,\omega)\psi''(sz) \tag{6.10a}$$

$$W(s,\omega,z) = C(s,\omega)\psi(sz) + D(s,\omega)\psi'(sz) \tag{6.10b}$$

where ψ is again defined as $\psi(\xi) = -\sinh\xi + \xi\cosh\xi$. Then using the identity (6.9) derived for a double transformed function, we obtain linear system to solve for Fourier coefficients C and D:

$$C(s,\omega)\beta(s,\omega) + D(s,\omega)\beta'(s,\omega) = 2\pi M(s)\delta(\omega+sv)$$

$$C(s,\omega)\mu(s,\omega) + D(s,\omega)\mu'(s,\omega) = 2\pi N(s)\delta(\omega+sv)$$

where

$$\beta(s,\omega) = \bar{g}(s,\omega)s\big(\psi(sh) + \psi''(sh)\big) + k^2\Upsilon s^2\psi'(sh)$$

$$\beta'(s,\omega) = \bar{g}(s,\omega)s\big(\psi'(sh) + \psi'''(sh)\big) + k^2\Upsilon s^2\psi''(sh)$$

$$\mu(s,\omega) = \bar{g}(s,\omega)s\big(3\psi'(sh) - \psi'''(sh)\big) + \Upsilon s^2\psi(sh)$$

$$\mu'(s,\omega) = \bar{g}(s,\omega)s\big(3\psi''(sh) - \psi''''(sh)\big) + \Upsilon s^2\psi'(sh)$$

and

$$M(s) = (f_r + f_l)\sin sR + i(f_r - f_l)\cos sR$$

$$N(s) = \gamma(\sin\alpha_l + \sin\alpha_r)\cos sR + i\gamma(\sin\alpha_l - \sin\alpha_r)\sin sR - 2\Pi\frac{\sin sR}{s}$$

From this we apply the inverse temporal Fourier Transform to obtain spatial transform of displacements u and w in the moving reference frame:

$$
\begin{aligned}
\hat{u}(s,z,t) &= \mathscr{F}_t^{-1}\big[U(s,z,\omega)\big] \\
&= \frac{1}{2\pi}\int_{-\infty}^{\infty} 2\pi i \frac{(\mu'M - \beta'N)\psi' + (\beta N - \mu M)\psi''}{\beta\mu' - \beta'\mu}\delta(\omega + sv)e^{i\omega t}\,d\omega \\
&= ie^{-isvt}\left[\frac{(\mu'M - \beta'N)\psi' + (\beta N - \mu M)\psi''}{\beta\mu' - \beta'\mu}\right]_{\omega = -sv}
\end{aligned}
$$

and

$$
\begin{aligned}
\hat{w}(s,z,t) &= \mathscr{F}_t^{-1}\big[W(s,z,\omega)\big] \\
&= \frac{1}{2\pi}\int_{-\infty}^{\infty} 2\pi \frac{(\mu'M - \beta'N)\psi + (\beta N - \mu M)\psi'}{\beta\mu' - \beta'\mu}\delta(\omega + sv)e^{i\omega t}\,d\omega \\
&= e^{-isvt}\left[\frac{(\mu'M - \beta'N)\psi + (\beta N - \mu M)\psi'}{\beta\mu' - \beta'\mu}\right]_{\omega = -sv}
\end{aligned}
$$

Setting $t = 0$ we have the spatial Fourier transforms of the moving reference frame:

$$\hat{u}(s,z) = i\left[\frac{(\mu'M - \beta'N)\psi' + (\beta N - \mu M)\psi''}{\beta\mu' - \beta'\mu}\right]_{\omega = -sv} \tag{6.11}$$

$$\hat{w}(s,z) = \left[\frac{(\mu'M - \beta'N)\psi + (\beta N - \mu M)\psi'}{\beta\mu' - \beta'\mu}\right]_{\omega = -sv} \tag{6.12}$$

With these transform solutions (6.11), (6.12), we can proceed to solve for the elastic energy in §6.2 necessary to calculate the rate at which energy is released from the system.

6.2   Elastic Energy of Moving Droplet

We now calculate the elastic energy in the substrate using the definition (5.40) from Ch. 5, noting that for the traveling wave solution given by a droplet with constant velocity the zero order elastic energy is constant in time for a given velocity v:

$$\mathscr{E}_{elastic} = \frac{1}{2}\iint_\Omega \bar{\tau}\cdot\bar{\varepsilon}\,d\Omega$$

Where reworking the integrand we obtain, using incompressibility condition $\varepsilon_{kk} = 0$:

$$\bar{\tau} \cdot \bar{\varepsilon} = \tau_{xx}\varepsilon_{xx} + 2\tau_{xz}\varepsilon_{xz} + \tau_{zz}\varepsilon_{zz}$$

$$= \varepsilon_{xx}\left[2\int_{-\infty}^{0}\zeta(x-vt')\dot{\varepsilon}_{xx}(t')\,dt' - p\right] + 2\varepsilon_{xz}\left[2\int_{-\infty}^{0}\zeta(x-vt')\dot{\varepsilon}_{xz}(t')\,dt'\right]$$

$$+ \varepsilon_{zz}\left[2\int_{-\infty}^{0}\zeta(x-vt')\dot{\varepsilon}_{zz}(t')\,dt' - p\right]$$

$$= 4\varepsilon_{zz}\int_{-\infty}^{0}\zeta(x-vt')\dot{\varepsilon}_{zz}(t')\,dt' + 4\varepsilon_{xz}\int_{-\infty}^{0}\zeta(x-vt')\dot{\varepsilon}_{xz}(t')\,dt'$$

giving us elastic energy calculation

$$\mathcal{E}_{elastic} = 2\iint_{\Omega}\left[\varepsilon_{zz}\int_{-\infty}^{0}\zeta(x-vt')\dot{\varepsilon}_{zz}(t')\,dt' + \varepsilon_{xz}\int_{-\infty}^{0}\zeta(x-vt')\dot{\varepsilon}_{xz}(t')\,dt'\right]d\Omega$$

$$= 2\int_{0}^{h}\mathcal{F}_{x}\left[\varepsilon_{zz}\int_{-\infty}^{0}\zeta(x-vt')\dot{\varepsilon}_{zz}(t')\,dt' + \varepsilon_{xz}\int_{-\infty}^{0}\zeta(x-vt')\dot{\varepsilon}_{xz}(t')\,dt'\right]_{s=0}dz$$

Using that for constant velocity v, our strains ε obey the first order traveling wave equation:

$$\dot{\varepsilon} + v\partial_{x}\varepsilon = 0$$

94

and substituting the definition of the relaxation function (6.3) for ζ we have that

$$
\begin{aligned}
\mathcal{E}_{elastic} = 2\bar{G}\Big[& \int_0^h \mathscr{F}_x\big[\varepsilon_{zz}^2 + \varepsilon_{xz}^2\big]_{s=0} \, dz \\
& + \frac{-v(t_v)^n}{\Gamma(1-n)} \int_0^h \mathscr{F}_x\Big[\varepsilon_{zz} \int_{-\infty}^0 (-t')^{-n} \partial_x \varepsilon_{zz}(x - v t') \, dt'\Big]_{s=0} \, dz \\
& + \frac{-v(t_v)^n}{\Gamma(1-n)} \int_0^h \mathscr{F}_x\Big[\varepsilon_{xz} \int_{-\infty}^0 (-t')^{-n} \partial_x \varepsilon_{xz}(x - v t') \, dt'\Big]_{s=0} \, dz \Big] \\
= 2\bar{G}\Big[& \int_0^h \mathscr{F}_x\big[\varepsilon_{zz}^2 + \varepsilon_{xz}^2\big]_{s=0} \, dz \\
& + \frac{-v(t_v)^n}{\Gamma(1-n)} \int_0^h \mathscr{F}_x\Big[\varepsilon_{zz} \int_0^\infty t^{-n} \partial_x \varepsilon_{zz}(x + v t) \, dt\Big]_{s=0} \, dz \\
& + \frac{-v(t_v)^n}{\Gamma(1-n)} \int_0^h \mathscr{F}_x\Big[\varepsilon_{xz} \int_0^\infty t^{-n} \partial_x \varepsilon_{xz}(x + v t) \, dt\Big]_{s=0} \, dz \Big] \\
= 2\bar{G} & \int_0^h \mathscr{F}_x\big[\varepsilon_{zz}^2 + \varepsilon_{xz}^2\big]_{s=0} \, dz \\
& - \frac{\bar{G} v(t_v)^n}{\pi \Gamma(1-n)}\Big[\int_0^h \Big[\hat{\varepsilon}_{zz} * \mathscr{F}_x\Big[\int_0^\infty t^{-n} \partial_x \varepsilon_{zz}(x + v t) \, dt\Big] \\
& + \hat{\varepsilon}_{xz} * \mathscr{F}_x\Big[\int_0^\infty t^{-n} \partial_x \varepsilon_{xz}(x + v t) \, dt\Big]\Big]_{s=0} \, dz \Big]
\end{aligned}
$$

We calculate the unresolved transform in the above equation for general function $f'(x + v t)$:

$$
\begin{aligned}
\mathscr{F}_x\Big[\int_0^\infty t^{-n} f'(x + v t) \, dt\Big] &= \int_{-\infty}^\infty \int_0^\infty t^{-n} f'(x + v t) e^{-isx} \, dt \, dx \\
&= \int_0^\infty t^{-n} \int_{-\infty}^\infty f'(x + v t) e^{-isx} \, dx \, dt \\
&= \int_0^\infty t^{-n} e^{isvt} \int_{-\infty}^\infty f'(x) e^{-isx} \, dx \, dt \\
&= is\hat{f}(s) \int_0^\infty t^{-n} e^{isvt} \, dt \\
&= -\hat{f}(s) \frac{(-isv)^n}{v} \Gamma(1-n)
\end{aligned}
$$

This gives us estimate for elastic energy of the substrate with a moving droplet given by

$$
\mathcal{E}_{elastic} = 2\bar{G} \int_0^h \mathscr{F}_x\big[\varepsilon_{xx}^2 + \varepsilon_{xz}^2\big]_{s=0} \, dz + \frac{\bar{G}}{\pi}(v t_v)^n \int_0^h \big[\hat{\varepsilon}_{zz} * \big((-is)^n \hat{\varepsilon}_{zz}\big) + \hat{\varepsilon}_{xz} * \big((-is)^n \hat{\varepsilon}_{xz}\big)\big]_{s=0} \, dz
$$

$$= \frac{\bar{G}}{\pi} \int_0^h \left[\hat{\varepsilon}_{zz} * \left((1 + (-i s v t_v)^n) \hat{\varepsilon}_{zz} \right) + \hat{\varepsilon}_{xz} * \left((1 + (-i s v t_v)^n) \hat{\varepsilon}_{xz} \right) \right]_{s=0} dz \tag{6.13}$$

We use this equation (6.13) to calculate the elastic energy contained in the substrate for a moving droplet traveling at constant speed v. This equation (6.13) is calculated using Gaussian quadrature where the integrand is evaluated at Gaussian abscissae corresponding with interval $z \in [0, h]$ and integrated numerically using the associated weights and integrand evaluations.

Note that equation (6.13) generalizes the elastic energy for a given droplet velocity, and indeed is consistent with the zero order elastic energy formulation (5.41) derived in Ch. 5 for $v = 0$. As the droplet migrates, the modulus or surface energy located at the droplet center of mass will adjust according to the specified gradient applied to induce droplet motion according the asymmetric model previously outlined. From this we construct the total energy functional $\mathscr{E}_{total}$ and calculate the rate at which total energy is released from the system by taking a discrete derivative approximation of the total energy:

$$\frac{d}{dt} \mathscr{E}_{total} \approx \frac{\mathscr{E}_{total}(\Delta t) - \mathscr{E}_{total}(0)}{\Delta t} \tag{6.14}$$

which will be used later to compute the velocity v such that (6.14) matches the solid dissipation computed in §6.3.

6.3 Energy Dissipation

Similarly to the elastic energy in the system, we seek to compute the rate at which energy is dissipated $\mathscr{P}_{solid}$ in the form of heat within the substrate. Balancing this with the rate at which energy is released from the system due to migration will give us the predicted velocity v of the droplet for a given gradient in substrate properties. The formula for solid dissipation is given by [26, 49]:

$$\mathscr{P}_{solid} = \frac{1}{2} \iint_{\Omega} \bar{\tau} \cdot \dot{\varepsilon} \, d\Omega \tag{6.15}$$

where we manipulate similar to the definition of elastic energy to obtain:

$$\mathscr{P}_{solid} = 2 \int_0^h \mathscr{F}_x \left[\dot{\varepsilon}_{zz} \int_{-\infty}^0 \zeta(x - v t') \dot{\varepsilon}_{zz}(t') \, dt' + \dot{\varepsilon}_{xz} \int_{-\infty}^0 \zeta(x - v t') \dot{\varepsilon}_{xz}(t') \, dt' \right]_{s=0} dz$$

which substituting in our definition for relaxation function ζ we have

$$
\begin{aligned}
\mathscr{P}_{solid} = {}& 2\bar{G}\Big[\int_0^h \mathscr{F}_x\big[\varepsilon_{zz}\dot{\varepsilon}_{zz}+\varepsilon_{xz}\dot{\varepsilon}_{xz}\big]_{s=0}\,dz \\
& + \frac{-v(t_v)^n}{\Gamma(1-n)}\int_0^h \mathscr{F}_x\Big[\dot{\varepsilon}_{zz}\int_{-\infty}^0 (-t')^{-n}\partial_x\varepsilon_{zz}(x-vt')\,dt'\Big]_{s=0}\,dz \\
& + \frac{-v(t_v)^n}{\Gamma(1-n)}\int_0^h \mathscr{F}_x\Big[\dot{\varepsilon}_{xz}\int_{-\infty}^0 (-t')^{-n}\partial_x\varepsilon_{xz}(x-vt')\,dt'\Big]_{s=0}\,dz\Big] \\
= {}& 2\bar{G}\Big[\int_0^h \mathscr{F}_x\big[\varepsilon_{zz}\dot{\varepsilon}_{zz}+\varepsilon_{xz}\dot{\varepsilon}_{xz}\big]_{s=0}\,dz \\
& + \frac{-v(t_v)^n}{\Gamma(1-n)}\int_0^h \mathscr{F}_x\Big[\dot{\varepsilon}_{zz}\int_0^\infty t^{-n}\partial_x\varepsilon_{zz}(x+vt)\,dt\Big]_{s=0}\,dz \\
& + \frac{-v(t_v)^n}{\Gamma(1-n)}\int_0^h \mathscr{F}_x\Big[\dot{\varepsilon}_{xz}\int_0^\infty t^{-n}\partial_x\varepsilon_{xz}(x+vt)\,dt\Big]_{s=0}\,dz\Big] \\
= {}& \frac{-\bar{G}v}{\pi}\int_0^h \mathscr{F}_x\big[\hat{\varepsilon}_{zz}*(is\hat{\varepsilon}_{zz})+\hat{\varepsilon}_{xz}*(is\hat{\varepsilon}_{xz})\big]_{s=0}\,dz \\
& + \frac{\bar{G}v^2(t_v)^n}{\pi\Gamma(1-n)}\Big[\int_0^h\Big[(is\hat{\varepsilon}_{zz})*\mathscr{F}_x\Big[\int_0^\infty t^{-n}\partial_x\varepsilon_{zz}(x+vt)\,dt\Big] \\
& + (is\hat{\varepsilon}_{xz})*\mathscr{F}_x\Big[\int_0^\infty t^{-n}\partial_x\varepsilon_{xz}(x+vt)\,dt\Big]\Big]_{s=0}\,dz\Big]
\end{aligned}
$$

$$
\Rightarrow \mathscr{P}_{solid} = \frac{\bar{G}v}{\pi}\int_0^h \big[\big(-is\hat{\varepsilon}_{zz}\big)*\big((1+(-isvt_v)^n)\hat{\varepsilon}_{zz}\big)+\big(-is\hat{\varepsilon}_{xz}\big)*\big((1+(-isvt_v)^n)\hat{\varepsilon}_{xz}\big)\big]_{s=0}\,dz
$$

$$(6.16)$$

With traveling displacement transforms (6.11), (6.12) defined in §6.1, we can numerically construct and evaluate the integrand of (6.16) at Gaussian nodes on interval $z \in [0, h]$ and evaluate (6.16) using Gaussian quadrature as done for (6.13). With these computations we can solve for the velocity v such that the rate at which energy is released by migration (6.14) matches that of dissipation within the solid (6.16). These results are discussed in §6.4.

6.4   Results

With the formulation of energy release rate (6.14) from §6.2 and energy dissipation (6.16) from §6.3, we can now predict the velocity v of a droplet for which motion has been induced by equating the rate of energy release with the rate at which energy is dissipated to heat. We seek to solve the

equation

$$\frac{d}{dt}\mathscr{E}_{total}(v;\tilde{G},\tilde{\Upsilon}) = \mathscr{P}_{solid}(v;\tilde{G},\tilde{\Upsilon}) \tag{6.17}$$

This is done for the set of parameters shown in Ch. 5 and plotted in Fig. 6.1 for the case of the surface energy gradient. As seen in Fig. 6.1, we observe that for the surface energy gradient that the mean surface energy Υ is critical in determining the necessary gradient to induce motion as seen in Ch. 5, however is not critical in determining the velocity of the droplet for a given gradient assuming that motion has been induced by the gradient.
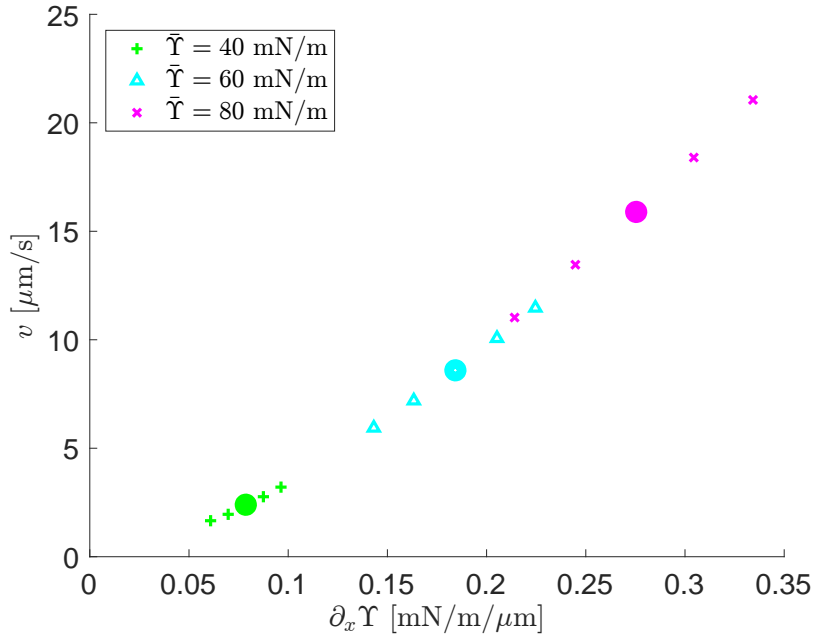
Figure 6.1 Velocity prediction for droplets using the surface energy gradient for various average surface energies $\tilde{\Upsilon}$. Large dots signify the velocity attained meeting at least the benchmark contact angle threshold of $\Delta\alpha = \alpha_l - \alpha_r = 1.8°$.

In addition we plot the results for the stiffness gradient in Fig. 6.2, of which we only plot for average modulus $\bar{G} = 1$ as the results from §5.7 indicate this is the only scenario in the example where the stiffness gradient was sufficient to exceed the benchmark contact angle threshold. As discussed in §5.7, however, we do not believe this scenario the physically feasible.
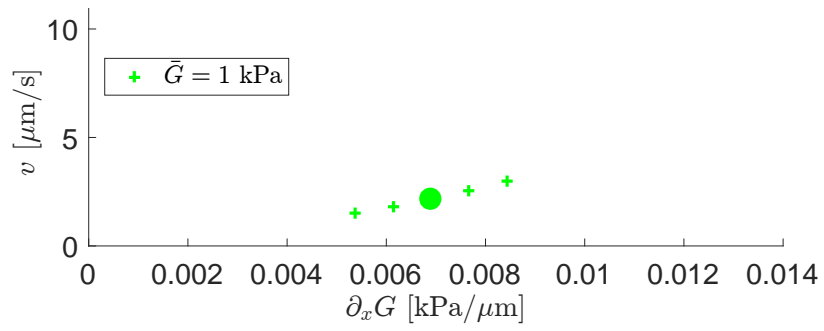
Figure 6.2 Velocity prediction for droplets using the shear modulus ggradient for average modulus $\bar{G} = 1$ kPa. The large dot signifies the velocity attained meeting at least the benchmark contact angle threshold of $\Delta\alpha = \alpha_l - \alpha_r = 1.8°$. These gradients are experimentally unrealistic to currently synthesize for average shear modulus of $\bar{G} = 1$ kPa. Vertical scale kept same as in Fig. 6.1 for comparison.

CHAPTER

7

CONCLUSIONS AND FUTURE DIRECTIONS

In this thesis we have presented modeling and analysis of the elastic deformation of a soft solid as influenced by capillary forces from a fluid. Our work here mainly focused on the interaction of a two dimensional droplet on a soft substrate and the effect this interaction has on the resulting shape of the droplet and the elastic substrate. Working and improving this model we investigated droplet dynamics as caused by gradients in substrate stiffness and solid surface energy.

Notably when solving the symmetric two dimensional geometry as well as the axisymmetric three dimensional geometry in Ch. 3, we highlighted the importance that the traction boundary condition has on the boundedness of solutions under general contact line loading. The generalized linear curvature developed in this chapter led to the bounded solution not only in the vertical displacement w but in the horizontal displacement u at the three phase contact line for a contact line force with non-zero tangential loading. The development of this model was necessary to analyze the deformation at the contact line for general force loading, an issue introduced when considering deformed solids for which the resulting system does not strictly obey Young's equation (1.1) which guarantees that for droplets resting on rigid solids that the net capillary force is entirely normal to the solid interface.

Proceeding with the improved boundary condition presented in Ch. 3, we investigated the influence that substrate gradients such as substrate elastic modulus G and solid surface energy γ_s have on the resulting deformation field in the solid in Ch. 5. The resulting configuration of both the solid deformation as well as the two dimensional droplet shape under these conditions becomes asymmetric. As supported by experiments in [1, 43], the contact angle asymmetry of the resulting configuration is the determining factor in the onset of droplet motion.

Advancing our deformation model from Ch. 3 to accommodate for gradients in substrate properties using both an asymptotic expansion and analytic Fourier transform model as well as a numerical Finite Element based model, solutions to the elastic equilibrium equations (2.18) were obtained. From these solutions the total energy comprised of surface as well as elastic energies was computed and minimized with respect to independent left and right contact angles α_l and α_r. From here we have a full description of the energy minimum configuration of the droplet-substrate system characterized by the minimizing contact angles α_l and α_r. This allows us to predict conditions for which droplet motion is inducted by substrate gradients such as elastic modulus or surface energy based on a benchmark threshold contact angle difference of 1.8° from [43]. Notably we determine that droplet motion solely induced by a stiffness gradient is currently infeasible using current experimental methods available for creating substrates with gradients in elastic moduli.

Using the results from Ch. 5 we then investigate the scenario of a moving droplet in Ch. 6. This model utilized a dynamic viscoelastic stress tensor (6.2) as opposed to the steady state stress tensor utilized in Chs. 3, 4 and 5. Solving the two dimensional moving droplet model involved transforming our equilibrium model (2.18) in both space and time to obtain displacement transforms from which we could obtain deformations and energies associated with our droplet-substrate system. From here the viscoelastic dissipation representing the dominant resistance to motion was calculated and compared to the rate at which energy is released by migration, allowing the droplet velocities associated with dynamic cases predicted in Ch. 5 to be calculated.

Future directions that this project could take include applying the methodology outlined in this thesis to alternative physical scenarios such as gradients in substrate thickness or thermal or electrical gradients. Also investigating methods for applying the methodology outlined here for three dimensional droplets would be of great benefit to observe qualitative similarities and differences between our two dimensional geometry and the physically realistic three dimensional geometry. In addition, taking the recommendations of the model outlined in this thesis and experimentally investigating the feasibility and accuracy of the outlined scenarios would be of great value in validating the model.

Improving the numerical techniques used in Ch. 5 for the finite element analysis to obtain better accuracy by using higher order basis functions would also be an improvement, allowing for a more computationally based method for obtaining the minimum energy configuration leading to the results presented in Chs. 5 and 6. In addition, numerical techniques would allow the model to be generalized for nonlinear elastic solutions. The high strains at contact lines venture on the border of linear and nonlinear elasticity, and considering the general model would allow for higher solution fidelity. Though we believe the linear methodology used throughout the thesis is sufficient to accurately answer the questions posed in this thesis, future directions of the project may benefit from the formulation of a more robust nonlinear model.

BIBLIOGRAPHY

[1] AHMED, G., MATHIEU, S., JERMY, M., TAYLOR, M. (2014) Modeling the Effects of Contact Angle Hysteresis on the Sliding of Droplets Down Inclined Surfaces. *European Journal of Mechanics B/Fluids* **48** 218-230.

[2] ANDREOTTI, B., BÄUMCHEN, O., BOULOGNE, F., DANIELS, K. E., DUFRESNE, E. R., PERRIN, H., SALEZ, T., SNOEIJER, J. H., STYLE, R. W. (2016) Soft Capillarity: When and How Does Surface Tension Deform Soft Solids? *Soft Matter* **12** 2993-2996.

[3] ANDREOTTI, B., SNOEIJER, J. H. (2016) Soft Wetting and the Shuttleworth Effect, at the Crossroads Between Thermodynamics and Mechanics. *Europhysics Letters* **113** 66001.

[4] BARDALL, A., DANIELS, K. E., SHEARER, M. (2018) Deformation of an Elastic Substrate Due to a Resting Sessile Droplet. *European Journal of Applied Mathematics* **29 (2)** 281-300.

[5] BICO, J., REYSSAT, É., ROMAN, B. (2018) Elastocapillarity: When Surface Tension Deforms Elastic Solids, *Annual Reviews* **50** 629-659.

[6] BOSTWICK, J. B., SHEARER, M., DANIELS, K. E. (2014) Elastocapillary Deformations on Partially-Wetting Substrates: Rival Contact-Line Models. *Soft Matter* **10** 7361-7369.

[7] BUENO, J., BAZILEVS, Y., JUANES, R., GOMEZ, H. (2017) Droplet Motion Driven by tensotaxis. *Elsevier* **13** 10-16.

[8] BUENO, J., BAZILEVS, Y., JUANES, R., GOMEZ, H. (2018) Wettability Control of Droplet Durotaxis. *Soft Matter* **14** 1417-1426.

[9] CHAUDHURY, M. K., WHITESIDES, G. M. (1992) How to Make Water Run Uphill. *Science* **256** 1539-1541.

[10] CROWE-WILLOUGHBY, J. A., WEIGER, K. L., ÖZCAM, A. E., GENZER, J. (2010) Formation of Silicone Elastomer Networks Films with Gradients in Modulus. *Elsevier* **51 (3)** 763-773.

[11] DERVAUX, J., LIMAT, L. (2015) Contact Lines on Soft Solids with Uniform Surface Tension: Analytical Solutions and Double Transition for Increasing Deformability. *Proceedings of the Royal Society A* **471** 2176.

[12] DHIR, V., GAO, D., MORLEY, N. B. (2004) Understanding Magnetic Field Gradient Effect from a Liquid Metal Droplet Movement. *Journal of Fluids Engineering* **126** 120-124.

[13] HARLAND, B., WALCOTT, S., SUN, S. X. (2011) Adhesion Dynamics and Durotaxis in Migrating Cells. *Physical Biology* **8** 6665.

[14] HERDE, D. (2013) *Contact Line Dynamics on Heterogeneous Substrates*. (Doctoral dissertation) *Georg-August University School of Science*.

[15] HOURLIER-FARGETTE, A., ANTHOWIAK, A., CHATEAUMINOIS, A., NEUKIRCH, S. (2017) Role of Uncrosslinked Chains in Droplets Dynamics on Silicone Elastomers. *Soft Matter* **13** 3484-3491.

[16] HOURLIER-FARGETTE, A., DERVAUX, J., ANTKOWIAK, A., NEUKIRCH, S. (2018) Extraction of Silicone Uncrosslinked Chains at Air-Water-Poydimethylsiloxane Triple Lines. *Langmuir* **34 (41)** 12244-12250.

[17] HUI, C. Y., JAGOTA, A. (2014) Deformation Near a Liquid Contact Line on an Elastic Substrate. *Proceedings of the Royal Society A* **470** 20140085.

[18] JAGOTA, A., PARETKAR, D., GHATAK, A. (2012) Surface-tension-induced Flattening of a Nearly Plane Elastic Solid. *Physical Review E* **85** 051602.

[19] JERISON, E. R., XU, Y., WILEN, L. A., DUFRESNE, E. R. (2011) Deformation of an Elastic Substrate by a Three-Phase Contact Line. *Physical Review Letters* **106** 186103.

[20] KARPITSCHKA, S., DAS, S., VAN GORCUM, M., PERRIN, H., ANDREOTTI, B., SNOEIJER, J. H. (2015) Droplets Move Over Viscoelastic Substrates by Surfing a Ridge. *Nature Communications* **6** 7891.

[21] KIM, H., MAHADEVAN, L. (2006) Capillary Rise Between Elastic Sheets. *Journal of Fluid Mechanics* **548** 141-150.

[22] KOURSARI, N., AHMED, G., STAROV, V. M. (2018) Equilibrium Droplets on Deformable Substrates: Equilibrium Conditions. *Langmuir* **34 (19)** 5672-5677.

[23] LIANG, H., CAO, Z., WANG, Z., DOBRYNIN, A. V. (2018) Surface Stresses and a Force Balance at a Contact Line. *Langmuir* **34 (25)** 7497-7502.

[24] LIANG, H., CAO, Z., WANG, Z., DOBRYNIN, A. V. (2018) Surface Stress and Surface Tension in Polymeric Networks. *ACS Macro Letters* **7 (1)** 116-121.

[25] LIMAT, L. (2012) Straight Contact Lines on a Soft, Incompressible Solid. *European Phys. Journal E.* **35** 1-13.

[26] LONG, D., AJDARI, A., LEIBLER, L. (1996) Static and Dynamic Wetting Properties of Thin Rubber Films. *Langmuir* **12 (21)** 5221-5230.

[27] LUBBERS, L., A., WEIJS, J. H., BOTTO, L., DAS, S. (2014) Drops on Soft Solids: Free Energy and Double Transition of Contact Angles. *Journal of Fluid Mechanics* **747**

[28] MARCHAND, A., DAS, S., SNOEIJER, J. H., ANDREOTTI, B. (2012) Capillary Pressure and Contact Line Force on a Soft Solid. *Physical Review Letters* **108** 094301.

[29] MASUREL, R., ROCHÉ, M., LIMAT, L., IONESCU, I., DERVAUX, J. (2018) Corners in Soft Solids Behave as Defects in Crystals. `arXiv.1806.07701`

[30] ONUKI, A., KANATANI, K. (2005) Droplet Motion with Phase Change in a Temperature Gradient. *Physical Review E* **72** 27844.

[31] PALCHESKO, R. N., ZHANG, L., SUN, Y., FEINBER, A. W. (2012) Development of Polydimethylsiloxane Substrates with Tunable Elastic Modulus to Study Cell Mechanobiology in Muscle and Nerve. *PLoS ONE* **7 (12)** e51499.

[32] PARK, S. J., WEON, B. M., LEE, J. S., KIM, J., JE, J. H. (2014) Visualization of Asymmetric Wetting Ridges on Soft Solids with X-ray Microscopy. *Nature Communications* **5** 4369.

[33] PARK, S. J., BOSTWICK, J. B., DE ANDRADE, V., JE, J. H. (2017) Self-spreading of the Wetting Ridge During Stick-slip on a Viscoelastic Surface. *Soft Matter* **13** 8331-8336.

[34] SCHULMAN, R. D., TREJO, M., SALEZ, T., RAPHAËL, E., DALNOKI-VERESS, K. (2018) Surface Energy of Strained Amorphous Solids. *Nature Communications* **9** 982.

[35] SHANAHAN, M. E. R., CARRÉ, A. (1995) Viscoelastic Dissipation in Wetting and Adhesion Phenomena. *Langmuir* **11 (4)** 1396-1402.

[36] SHAO, X., SAYLOR, J. R., BOSTWICK, J. B. (2018) Extracting the Surface Tension of Soft Gels from Elastocapillary Wave Behavior. *Soft Matter* **14** 7347-7353.

[37] SNOEIJER, J. H., ANDREOTTI, B. (2013) Moving Contact Lines: Scales, Regimes, and Dynamical Transitions. *Annual Reviews* **45** 269-292.

[38] SNOEIJER, J. H., ROLLEY, E., ANDREOTTI, B. (2018) Paradox of Contact Angle Selection on Stretched Soft Solids. *Physical Review Letters* **121** 068003.

[39] SOUTAS-LITTLE, R. W. (1999) *Elasticity.* Dover Publications.

[40] STRICHER, A., RINALDI, R. G., MACHADO, G., CHAGNON, G., FAVIER, D., CHAZEAU, L., GANACHAUD, F. (2016) Light-induced Bulk Architecturation of PDMS Membranes. *Macromolecula Materials and Engineering* **301 (10)** 1151-1157.

[41] STYLE, R. W., DUFRESNE, E. R. (2012) Static Wetting on Deformable Substrates, From Liquids to Soft Solids. *Soft Matter* **8** 7177-7184.

[42] STYLE, R. W., BOLTYANSKIY, R., CHE, Y., WETTLAUFER, J. S., WILEN, L. A., DUFRESNE, E. R. (2013) Universal Deformation of Soft Substrates Near a Contact Line and the Direct Measurement of Solid Surface Stresses. *Physical Review Letters* **110** 066103.

[43] STYLE, R. W., CHE, Y., PARK, S. J., WEON, B. M., JE, J. H., HYLAND, C., GERMAN, G. K., POWER, M. P., WILEN, L. A., WETTLAUFER, J. S., DUFRESNE, E. R. (2013) Patterning Droplets with Durotaxis. *Proceedings of the National Academy of Sciences* **110 (31)** 12541-12544.

[44] STYLE, R. W., HYLAND, C., BOLTYANSKIY, R., WETTLAUFER, J. S., DUFRESNE, E. R. (2013) Surface Tension and Contact with Soft Elastic Solids. *Nature Communications* **4** 2728.

[45] STYLE, R. W., JAGOTA, A., HUI, C., DUFRESNE, E.R. (2017) Elastocapillarity: Surface Tension and the Mechanics of Soft Solids. *Annual Reviews* **8** 99-118.

[46] STYLE, R. W., XU, Q. (2018) The Mechanical Equilibrium of Soft Solids with Surface Elasticity. *Soft Matter* **14** 4569-4576.

[47] TEH, S. Y., LIN, R., HUN, L. H., LEE, A. P. (2008) Droplet Microfluidics. *Lab on a Chip* **8** 99-118.

[48] THEODORAKIS, P.E., EGOROV, S. A., MILCHEV, A. (2017) Stiffness-guided Motion of a Droplet on a Solid Substrate. *Journal of Chemical Physics* **146** 244705.

[49] Tschoegl, N. W. (2002) *The Phenomenological Theory of Linear Viscoelastic Behavior* Springer, Berlin, Heidelberg.

[50] Voué, M., Rioboo, R., Bauthier, C., Conti, J., Carlot, M., De Coninck, J. (2003) Dissipation and Moving Contact Lines on Non-rigid Substrates. *Journal of the European Ceramic Society* **23 (15)** 2769-2775.

[51] Weijs, J. H., Andreotti, B., Snoeijer, J. H. (2013) Elasto-capillarity at the Nanoscale: On the Coupling Between Elasticity and Surface Energy in Solids. *Soft Matter* **9** 8494-8503.

[52] Weijs, J. H., Snoeijer, J. H., Andreotti, B. (2014) Capillarity of Soft Amorphous Solids: A Microscopic Model for Surface Stress. *Physical Review E* **89** 042408.

[53] Xu, Q., Style, R. W., Dufresne, E. R. (2018) Surface Elastic Constants of a Soft Solid. *Soft Matter* **14** 916-920.

[54] Zhao, M., Dervaux, J., Narita, T., Lequeux, F., Limat, L., Roché, M. (2018) Geometrical Control of Dissipation During the Spreading of Liquids on Soft Solids. *Proceedings of the National Academy of Sciences* **115 (8)** 1748-1753.

APPENDIX

APPENDIX

$$ \text{A} $$

MATLAB CODE

Matlab code for two dimensional homogeneous model (§3.4)

```matlab
1  %clear, clc
2  %close all
3
4  tic;
5
6  %[E,nu,h,R,gamma,gamma_sg,gamma_ls,J,alpha,pg,lambda,L,k_sq0,k_sq1,k_sq2,
       k_sq3,n,n_short,m,S,s(n_short),ds,grav_opt,rad_opt]
7  grav_opt=0;      %0 for no gravity, 1 for first order low gravity, 2 for
       numerical gravity
8  rad_opt=0;       %0 for no radial force, 1 for radial force contact angle
       by energy, 2 for radial force contact angle by stress, 3 for manual
       input of contact angle
9  k_sq0=0;         %Initial k_sq parameter value (squared average slope at
       CL)
10
11  gamma=80;        %Liquid/Gas surface tension [mN/m]
```

```matlab
12  gamma_ls=80;      %Liquid/Solid surface stress [mN/m]
13  gamma_sg=80;      %Solid/Gas surface stress [mN/m]
14  E=6;              %Young's Modulus [kPa]
15  nu=0.5;          %Poisson's Ratio []
16  h=50;             %Height [micrometers]
17  R=150;            %Drop radius [micrometers]
18  pg=9.8;           %Specific gravity [mN/m^2/um]
19
20  Dgamma=gamma_ls-gamma_sg;              %Solid stress differential
21  Mgamma=(gamma_ls+gamma_sg)/2;          %Average solid stress
22  L=sqrt(gamma/(pg 1e6)) 1e6;            %Capillary length scale [
        micrometers]
23  hbar=h/R;                             %Nondimensionalized thickness
24  S=2000;                               %Cutoff Wavelength
25
26  %Node quantity and mesh generation
27  n=4 fix(S/5) ceil(R)+1;
28  s=linspace(0,S,n)';
29  s2=s(2:n);
30  ds=s(2);
31  disp(ds)
32
33  m=20 ceil(R)+1;
34  x=linspace(0,5,m)';
35  x_cl=linspace(.95,1.05,m)';
36
37  %Defines contact angle alpha and radial force imbalance J
38  if rad_opt==0
39      J=5;
40      alpha=acos((gamma_sg-gamma_ls)/gamma);
41  elseif rad_opt==1
42      cosa=(1-nu)/nu (gamma_sg-gamma_ls)/gamma+(1-2 nu)/nu;
43      J=gamma (1 - 2 nu)/(1-nu) (1+cosa); %<= CHANGE BACK!
44      alpha=acos(cosa);
45  elseif rad_opt==2
```

```matlab
46      cosa=(gamma_sg-gamma_ls)/gamma;
47      J=gamma(1-2nu)/(1-nu)(1+cosa);
48      alpha=acos(cosa);
49  end
50
51  %Surface pressure of fluid droplet
52  if grav_opt==0
53      lambda=gamma sin(alpha)/R;
54  elseif grav_opt==1
55      lambda=gamma sin(alpha)/R+(pg R 1e-6)/2(alpha csc(alpha)^2 - cot(
            alpha));
56  elseif grav_opt==2
57      lambda=pg. pressure_head(L 1e-6,R 1e-6,alpha);
58  end
59
60  %Vector's of commonly used function evaluations (2 signifies it excludes
61  %zero evaluation
62  s_sq = s.^2; s2_sq = s_sq(2:n);
63  sin_vec = sin(s); sin_vec2 = sin_vec(2:n);
64  cos_vec = cos(s); cos_vec2 = cos_vec(2:n);
65  tanh_vec = tanh(s. hbar); tanh_vec2=tanh_vec(2:n);
66
67  %Transform coefficients ('_0' indicates it will need to be re-evaluated
        once
68  %k^2 is obtained)
69  beta1_0 = s2.((1-2nu) E/(1+nu)/R^3 - k_sq0 s2_sq hbar gamma_sg/R^4).
        tanh_vec2 - s2_sq E hbar/(1+nu)/R^3;
70  beta2_0 = s2_sq.(E hbar/(1+nu)/R^3 + k_sq0 (3-4nu) gamma_sg/R^4).
        tanh_vec2 + s2.(2(1-nu) E/(1+nu)/R^3 + k_sq0 s2_sq hbar gamma_sg/R
        ^4);
71  mu1 = s2_sq.(E hbar/(1+nu)/R^3 - (3-4nu) gamma_sg/R^4). tanh_vec2 + s2
        .(-2(1-nu) E/(1+nu)/R^3 + s2_sq hbar gamma_sg/R^4);
72  mu2 = s2.(-1(1-2nu) E/(1+nu)/R^3 - s2_sq hbar gamma_sg/R^4). tanh_vec2
        - s2_sq E hbar/(1+nu)/R^3;
73
```

```matlab
74    M = (−2.J. sin_vec2./sqrt(2 pi))/R;
75    N = (2./sqrt(2 pi).(gamma. sin(alpha). cos_vec2−lambda. R. sin_vec2./s2)
         )/R;
76
77    chi_0 = beta1_0. mu2 − beta2_0. mu1;
78    s2C0_0 = (mu2. M − beta2_0. N)./chi_0;
79    s2D0_0 = (beta1_0. N − mu1. M)./chi_0;
80
81    Cs3lim=(1+nu) R^3 (lambda−gamma sin(alpha)/R)/(sqrt(2 pi) (1−nu) E);
82    w_hat0_0=sqrt(2/pi)./R^2.(s2C0_0.(s2. hbar−(3−4 nu). tanh_vec2)−s2D0_0
         . s2. hbar. tanh_vec2);
83    d1w_hat0_0=−1/R. s2. w_hat0_0;
84    w_hat0_0=[−2 hbar.(1 − 2 nu)./R^2. Cs3lim;w_hat0_0];
85    d1w_hat0_0=[0;d1w_hat0_0];
86
87    w0_0 = zeros(m,1); d1w0_0 = w0_0;
88
89    W=1/3 ones(1,n);
90    for i=2:n−1
91        W(i) = 2/3 (1+mod(i+1,2));
92    end
93
94    for i=1:m
95        wt=w_hat0_0. cos(s. x(i));
96        d1wt=d1w_hat0_0. sin(s. x_cl(i));
97        w0_0(i)=ds W wt;
98        d1w0_0(i)=ds W d1wt;
99    end
100
101   %Estimates parameter k^2 from zero−th order deformation
102   k1=(max(d1w0_0)−min(d1w0_0))/2;
103   %k_sq1=k1^2; %CHANGED 8/8/17 (change back!!!)
104   k_sq1=0;
105
```

```matlab
106   beta1 = s2.((1−2 nu) E/(1+nu)/R^3 − k_sq1 s2_sq hbar gamma_sg/R^4).
          tanh_vec2 − s2_sq E hbar/(1+nu)/R^3;
107   beta2 = s2_sq.(E hbar/(1+nu)/R^3 + k_sq1 (3−4 nu) gamma_sg/R^4).
          tanh_vec2 + s2.(2 (1−nu) E/(1+nu)/R^3 + k_sq1 s2_sq hbar gamma_sg/R
          ^4);
108
109   chi = beta1. mu2 − beta2. mu1;
110   s2C0 = (mu2. M − beta2. N)./chi;
111   s2D0 = (beta1. N − mu1. M)./chi;
112
113   u_hat0=sqrt(2/pi)./R^2.(s2D0.(s2. hbar+(3−4 nu). tanh_vec2)−s2C0.(s2.
          hbar. tanh_vec2));
114   w_hat0=sqrt(2/pi)./R^2.(s2C0.(s2. hbar−(3−4 nu). tanh_vec2)−s2D0. s2.
          hbar. tanh_vec2);
115   u_hat0=[0;u_hat0];
116   w_hat0=[−2 hbar.(1−2 nu)./R^2. Cs3lim;w_hat0];
117   d1u_hat0=1/R. s. u_hat0; d1u_hat0(1) = 0;
118   d1w_hat0=−1/R. s. w_hat0; d1w_hat0(1) = 0;
119
120   u0 = zeros(m,1);
121   w0 = u0; d1u0 = u0; d1w0 = u0;
122
123   for i=1:m
124       ut=u_hat0. sin(s. x(i));
125       wt=w_hat0. cos(s. x(i));
126       d1ut=d1u_hat0. cos(s. x_cl(i));
127       d1wt=d1w_hat0. sin(s. x_cl(i));
128       u0(i)=ds W ut;
129       w0(i)=ds W wt;
130       d1u0(i)=ds W d1ut;
131       d1w0(i)=ds W d1wt;
132   end
133
134   Er1 = 2 R^2/(sqrt(2 pi) (3−4 nu) k_sq1 gamma_sg^2) ((1−2 nu) E gamma sin(
          alpha)/(1+nu));
```

```matlab
135  Er2 = −2 R/(sqrt(2 pi) k_sq1 gamma_sg) J;
136  Er3 = 2 R/(sqrt(2 pi) gamma_sg) gamma sin(alpha);
137  Er4 = −2 R^2/(sqrt(2 pi)(3−4 nu) k_sq1 gamma_sg^2)(k_sq1 (3−4 nu)
         gamma_sg lambda + (1−2 nu) E J/(1+nu));
138
139  u_hat0_lim=Er1 . cos_vec./s_sq./s + Er2 . sin_vec./s_sq;
140  w_hat0_lim=Er3 . cos_vec./s_sq + Er4 sin_vec./s_sq./s;
141
142  sinOs_vec = sin_vec./s; sinOs_vec(1) = 1;
143
144  Du_hat0 = u_hat0 − u_hat0_lim;
145  Dw_hat0 = w_hat0 − w_hat0_lim;
146
147  n_short = ceil((S−1500)/ds) + 1;
148
149  Xn_0 = zeros(n_short,1); Zn_0 = Xn_0;
150  integrand_convz = −2/R^2 sinOs_vec . s_sq . Dw_hat0;
151  integrand_convz(1) = 2/R^2 (Er3+Er4);
152  Zn_0(1) = ds W integrand_convz;
153  for i = 2:n_short
154      Od = (s(i) cos(s(i)) sin_vec − s . sin(s(i)) . cos_vec)./(s_sq−s(i)^2);
155      Od(i) = 1/2 (1 − cos(s(i)) sin(s(i))/s(i));
156      Ev = (s . cos(s(i)) . sin_vec − s(i) . sin(s(i)) . cos_vec)./(s_sq−s(i)
            ^2);
157      Ev(i) = 1/2 (1 + cos(s(i)) sin(s(i))/s(i));
158      integrand_convx = −2 k_sq1/R^2 Od . s_sq . Du_hat0;
159      integrand_convx(1) = −2 k_sq1/R^2 (s(i) . cos(s(i)) − sin(s(i)))/(s(i)
            ^2) Er1;
160      integrand_convz = −2/R^2 Ev . s_sq . Dw_hat0;
161      integrand_convz(1) = 2/R^2 sin(s(i))./s(i) (Er3+Er4);
162      Xn_0(i) = ds W integrand_convx;
163      Zn_0(i) = ds W integrand_convz;
164  end
165
166  X_res_0 = −pi k_sq1/2/R^2 Er2 sin_vec(1:n_short);
```

```matlab
167  Z_res_0 = -pi/2/R^2 Er3 cos_vec(1:n_short);
168
169  X_0 = Xn_0 + X_res_0;
170  Z_0 = Zn_0 + Z_res_0;
171
172  s2C1_0 = (mu2(1:n_short-1). X_0(2:end) - beta2(1:n_short-1). Z_0(2:end))
          ./chi(1:n_short-1);
173  s2D1_0 = (beta1(1:n_short-1). Z_0(2:end) - mu1(1:n_short-1). X_0(2:end))
          ./chi(1:n_short-1);
174
175  s2C_0 = s2C0(1:n_short-1) + Dgamma/pi s2C1_0;
176  s2D_0 = s2D0(1:n_short-1) + Dgamma/pi s2D1_0;
177
178  w_hat_0=sqrt(2/pi)./R^2.(s2C_0.(s2(1:n_short-1). hbar-(3-4 nu).
          tanh_vec2(1:n_short-1))-s2D_0. s2(1:n_short-1). hbar. tanh_vec2(1:
          n_short-1));
179  w_hat_0=[-2 hbar.(1-2 nu)./R^2. Cs3lim;w_hat_0];
180  d1w_hat_0=-1/R. s(1:n_short). w_hat_0;
181  d1w_hat_0(1) = 0;
182
183  W_short=1/3 ones(1,n_short);
184  for i=2:n_short-1
185      W_short(i) = 2/3(1+mod(i+1,2));
186  end
187
188  w_0 = zeros(m,1); d1w_0 = w_0;
189  for i=1:m
190      wt=w_hat_0. cos(s(1:n_short). x(i));
191      d1wt=d1w_hat_0. sin(s(1:n_short). x_cl(i));
192      w_0(i)=ds W_short wt;
193      d1w_0(i)=ds W_short d1wt;
194  end
195
196  % k2=(max(d1w_0)-min(d1w_0))/2;
197  % k_sq2=k2^2;
```

```matlab
%load('Ksq.mat')
k_sq2=1/3;

beta1 = s2.((1-2 nu) E/(1+nu)/R^3 - k_sq2 s2_sq hbar gamma_sg/R^4).
    tanh_vec2 - s2_sq E hbar/(1+nu)/R^3;
beta2 = s2_sq.(E hbar/(1+nu)/R^3 + k_sq2 (3-4 nu) gamma_sg/R^4).
    tanh_vec2 + s2.(2 (1-nu) E/(1+nu)/R^3 + k_sq2 s2_sq hbar gamma_sg/R
    ^4);

chi = beta1.mu2 - beta2.mu1;
s2C0 = (mu2.M - beta2.N)./chi;
s2D0 = (beta1.N - mu1.M)./chi;

Er1 = 2 R^2/(sqrt(2 pi)(3-4 nu) k_sq2 gamma_sg^2)((1-2 nu) E gamma sin(
    alpha)/(1+nu));
Er2 = -2 R/(sqrt(2 pi) k_sq2 gamma_sg) J;
Er3 = 2 R/(sqrt(2 pi) gamma_sg) gamma sin(alpha);
Er4 = -2 R^2/(sqrt(2 pi)(3-4 nu) k_sq2 gamma_sg^2)(k_sq2 (3-4 nu)
    gamma_sg lambda + (1-2 nu) E J/(1+nu));

u_hat0_lim2=Er1.cos_vec./s_sq./s + Er2.sin_vec./s_sq;
w_hat0_lim2=Er3.cos_vec./s_sq + Er4 sin_vec./s_sq./s;

u_hat0_2=sqrt(2/pi)./R^2.(s2D0.(s2.hbar+(3-4 nu).tanh_vec2)-s2C0.(s2
    .hbar.tanh_vec2));
w_hat0_2=sqrt(2/pi)./R^2.(s2C0.(s2.hbar-(3-4 nu).tanh_vec2)-s2D0.s2
    .hbar.tanh_vec2);
u_hat0_2=[0;u_hat0_2];
w_hat0_2=[-2 hbar.(1-2 nu)./R^2.Cs3lim;w_hat0_2];

Du_hat0 = u_hat0_2 - u_hat0_lim2;
Dw_hat0 = w_hat0_2 - w_hat0_lim2;

Xn = zeros(n_short,1); Zn = Xn;
integrand_convz = -2/R^2 sinOs_vec.s_sq.Dw_hat0;
```

```
226   integrand_convz (1)  =  2/R^2 ( Er3+Er4 ) ;
227   Zn ( 1 )  =  ds  W  integrand_convz ;
228   for  i  =  2: n_short
229       Od  =  ( s ( i )  cos ( s ( i ) )  sin_vec  −  s .  sin ( s ( i ) ) .  cos_vec ) ./( s_sq−s ( i )^2 ) ;
230       Od ( i )  =  1/2 (1  −  cos ( s ( i ) )  sin ( s ( i ) )/ s ( i ) ) ;
231       Ev  =  ( s .  cos ( s ( i ) ) .  sin_vec  −  s ( i ) .  sin ( s ( i ) ) .  cos_vec ) ./( s_sq−s ( i )
               ^2 ) ;
232       Ev ( i )  =  1/2 (1  +  cos ( s ( i ) )  sin ( s ( i ) )/ s ( i ) ) ;
233       integrand_convx  =  −2 k_sq2/R^2 Od .  s_sq .  Du_hat0 ;
234       integrand_convx (1)  =  −2 k_sq2/R^2 ( s ( i ) .  cos ( s ( i ) )  −  sin ( s ( i ) ) )/( s ( i )
               ^2)  Er1 ;
235       integrand_convz  =  −2/R^2 Ev .  s_sq .  Dw_hat0 ;
236       integrand_convz (1)  =  2/R^2 sin ( s ( i ) ) ./ s ( i )  ( Er3+Er4 ) ;
237       Xn ( i )  =  ds  W  integrand_convx ;
238       Zn ( i )  =  ds  W  integrand_convz ;
239   end
240
241   X_res  =  −pi  k_sq2/2/R^2 Er2  sin_vec (1: n_short ) ;
242   Z_res  =  −pi/2/R^2 Er3  cos_vec (1: n_short ) ;
243
244   X  =  Xn  +  X_res ;
245   Z  =  Zn  +  Z_res ;
246
247   s2C1  =  ( mu2 (1: n_short−1) .  X (2: end )  −  beta2 (1: n_short−1) .  Z (2: end ) )./ chi
           (1: n_short−1) ;
248   s2D1  =  ( beta1 (1: n_short−1) .  Z (2: end )  −  mu1 (1: n_short−1) .  X (2: end ) )./ chi
           (1: n_short−1) ;
249
250   s2C  =  s2C0 (1: n_short−1)  +  Dgamma/pi  s2C1 ;
251   s2D  =  s2D0 (1: n_short−1)  +  Dgamma/pi  s2D1 ;
252
253   u_hat=sqrt (2/ pi ) ./R^2 . ( s2D .  ( s2 (1: n_short−1) .  hbar+(3−4 nu ) .  tanh_vec2
           (1: n_short−1))−s2C .  ( s2 (1: n_short−1) .  hbar .  tanh_vec2 (1: n_short−1) ) ) ;
254   w_hat=sqrt (2/ pi ) ./R^2 . ( s2C .  ( s2 (1: n_short−1) .  hbar−(3−4 nu ) .  tanh_vec2
           (1: n_short−1))−s2D .  s2 (1: n_short−1) .  hbar .  tanh_vec2 (1: n_short−1) ) ) ;
```

```matlab
255  u_hat=[0;u_hat];
256  w_hat=[−2 hbar.(1−2 nu)./R^2.Cs3lim;w_hat];
257  d1u_hat=1/R.s(1:n_short).u_hat;
258  d1w_hat=−1/R.s(1:n_short).w_hat;
259  d1u_hat(1) = 0; d1w_hat(1) = 0;
260
261  u = zeros(m,1); w = u; d1u = u; d1w = u;
262  for i=1:m
263      ut=u_hat.sin(s(1:n_short).x(i));
264      wt=w_hat.cos(s(1:n_short).x(i));
265      d1ut=d1u_hat.cos(s(1:n_short).x_cl(i));
266      d1wt=d1w_hat.sin(s(1:n_short).x_cl(i));
267      u(i)=ds W_short ut;
268      w(i)=ds W_short wt;
269      d1u(i)=ds W_short d1ut;
270      d1w(i)=ds W_short d1wt;
271  end
272
273  k3=(max(d1w)−min(d1w))/2;
274  k_sq3=k3^2;
275
276  disp([k_sq0 k_sq1 k_sq2 k_sq3])
277
278  params=[E,nu,h,R,gamma,gamma_sg,gamma_ls,J,alpha,pg,lambda,L,k_sq0,k_sq1,
            k_sq2,k_sq3,n,n_short,m,S,s(n_short),ds,grav_opt,rad_opt];
279
280  data.params=params;
281  data.s=s;
282  data.s_short=s(1:n_short);
283  data.x=x;
284  data.x_cl=x_cl;
285  data.u0=u0;
286  data.w0=w0;
287  data.d1u0=d1u0;
288  data.d1w0=d1w0;
```

```
289  data.u=u;
290  data.w=w;
291  data.d1u=d1u;
292  data.d1w=d1w;
293  data.u_hat0=u_hat0;
294  data.w_hat0=w_hat0;
295  data.d1u_hat0=d1u_hat0;
296  data.d1w_hat0=d1w_hat0;
297  data.u_hat=u_hat;
298  data.w_hat=w_hat;
299  data.d1u_hat=d1u_hat;
300  data.d1w_hat=d1w_hat;
301  data.X=X;
302  data.Z=Z;
303
304  Time = toc;
```

Matlab code for obtaining energy minimizing droplet contact angles for the case of a stiffness gradient (§5.7)

```matlab
function [Etot, data] = stiffgrad_energy(alpha, params)
tic;

h = params(1);
A = params(2);
Gbar = params(3);
c = params(4);
L = params(5);
gam = params(6);
Ups = params(7);
k_sq = gam^2/(4 Ups^2 - gam^2);

al = alpha(1);
ar = alpha(2);

fl = gam cos(al); fr = gam cos(ar);
[Ldrop, R, Fdrop_param] = polar_arclength(al, ar, A);
PI = gam (sin(al)+sin(ar))/(2 R);

dx = R/floor(R); X = 7;
x = -X R:dx:X R; n = length(x);

S = 10; ds = .001;
s = -S:ds:S; m = length(s); m0 = find(s==0);
sh = s h; sR = s R; s_sq = s.^2;
tanhsh = tanh(sh); coshsh = cosh(sh); sinhsh = sinh(sh);

xs = zeros(n,m-m0+1);
for i = 1:n
    xs(i,:) = s(m0:end) . x(i);
end
```

```matlab
33  M_r = (fl+fr) sin(sR);
34  M_i = (fr−fl) cos(sR);
35  N_r = gam (sin(al)+sin(ar)) cos(sR) − 2 PI sin(sR)./s; N_r(m0) = 0;
36  N_i = gam (sin(al)−sin(ar)) sin(sR);

38  psi0_h = −tanhsh + sh;
39  psi1_h = sh . tanhsh;
40  psi2_h = sh + tanhsh;
41  psi3_h = sh . tanhsh + 2;
42  psi4_h = sh + 3 tanhsh;

44  beta1 = Gbar s . (psi0_h+psi2_h) + k_sq Ups s.^2. psi1_h;
45  beta2 = Gbar s . (psi1_h+psi3_h) + k_sq Ups s.^2. psi2_h;
46  mu1 = Gbar s . (3 psi1_h−psi3_h) + Ups s.^2. psi0_h;
47  mu2 = Gbar s . (3 psi2_h−psi4_h) + Ups s.^2. psi1_h;
48  denom = beta1 . mu2 − beta2 . mu1;

50  C0_r = (mu2 . M_r − beta2 . N_r)./denom; C0_r(m0) = 0;
51  C0_i = (mu2 . M_i − beta2 . N_i)./denom; C0_i(m0) = −(gam R (sin(al)−sin(ar
        ))−h (fr−fl))/(2 Gbar);
52  D0_r = (beta1 . N_r − mu1 . M_r)./denom; D0_r(m0) = R (fl+fr)/(2 Gbar);
53  D0_i = (beta1 . N_i − mu1 . M_i)./denom; %D0_i scales like (fr−fl)/(2 Gbar
        s) for small s, limit adjustments in transforms
54  D0_i2 = D0_i; D0_i2(m0) = 0; %used for simplicity for calculations where
        multiplied by s^k (k>1)
55  %C0 is (odd) + i(even), D0 is (even) + i(odd)

57  uhat0_r = −C0_i . psi1_h − D0_i . psi2_h; uhat0_r(m0) = −C0_i(m0) psi1_h(m0
        ) − h (fr−fl)/Gbar;
58  uhat0_i = C0_r . psi1_h + D0_r . psi2_h;
59  what0_r = C0_r . psi0_h + D0_r . psi1_h;
60  what0_i = C0_i . psi0_h + D0_i . psi1_h; what0_i(m0) = 0;%C0_i(m0) psi0_h(
        m0);

62  W = 2/3 (1+(mod(1:m−m0+1,2)==0)); W(1) = 1/3; W(end) = 1/3;
```

```matlab
63
64  u0 = zeros(1,n); w0 = u0;
65  for i=1:n
66      wt = (what0_r(m0:m) . cos(xs(i,:)) − what0_i(m0:m) . sin(xs(i,:)))/pi;
67      ut = (uhat0_r(m0:m) . cos(xs(i,:)) − uhat0_i(m0:m) . sin(xs(i,:)))/pi;
68      w0(i) = ds sum(W. wt);
69      u0(i) = ds sum(W. ut);
70  end
71
72  C0 = C0_r + 1i C0_i; D0 = D0_r + 1i D0_i; D0_2 = D0_r + 1i D0_i2; sD0 = s
        . D0; sD0(m0) = 1i (fr−fl)/(2 Gbar);
73  if c~=0
74  %stanhsh = s . tanhsh;
75  FT_Gtp = 2 exp(−abs(s) L); FT_Gtp_sinv = FT_Gtp./s; FT_Gtp_sinv(m0) = 0;
76
77  conv_rad = 5/L; conv_ind = find(abs(s)<=conv_rad); conv_n = length(
        conv_ind); %conv_tail = conv_n − 1;
78  conv_W = ds 2/3 (1+(mod(1:conv_n,2)==0)); conv_W(1) = ds/3; conv_W(conv_n
        ) = ds/3;
79  FT_Gtp_conv = FT_Gtp(conv_ind); sFT_Gtp_conv = s(conv_ind) . FT_Gtp(
        conv_ind);
80  F0 = zeros(1,m−conv_n+1); F1 = F0; F2 = F0; F3 = F0; s_short = F0;
81  midi = (conv_n+1)/2; s_ind = midi:midi+m−conv_n;
82  for i=1:m−conv_n+1
83      index = midi + (i−1);
84      si = s(index); s_short(i) = si;
85      eta = s(i:i+conv_n−1); eta_sq = s_sq(i:i+conv_n−1);
86      eta_sinh = sinhsh(i:i+conv_n−1); eta_cosh = coshsh(i:i+conv_n−1);
87      eta_C0 = C0(i:i+conv_n−1)./eta_cosh;
88      eta_D0 = D0_2(i:i+conv_n−1)./eta_cosh;
89      eta_sD0 = sD0(i:i+conv_n−1)./eta_cosh;
90      eta_msq = eta_sq − si^2; eta_msq2 = eta_msq.^2; eta_msq3 = eta_msq .
            eta_msq2;
91
92      I1 = (si . eta_sinh − eta . sinh(si h))./eta_msq;
```

121

```matlab
93    I2 = si . ( eta_cosh − cosh ( si  h ) ) . / eta_msq ;
94    I3 = ( ( eta_sq + si ^2) . eta_sinh − 2 eta  si  sinh ( si  h ) − eta_msq . eta
          h  cosh ( si  h ) ) . / eta_msq2 ;
95    I4 = ( ( eta_sq + si ^2) . ( eta_cosh − cosh ( si  h ) ) − si  h  eta_msq . sinh (
          si  h ) ) . / eta_msq2 ;
96    I5 = ( 2  si  eta . ( cosh ( si  h ) − eta_cosh ) + si  h  eta_msq . eta_sinh ) . /
          eta_msq2 ;
97    I6 = ( ( eta_sq + si ^2)  sinh ( si  h ) − 2  si  eta . eta_sinh + si  h  eta_msq
          . eta_cosh ) . / eta_msq2 ;
98    I7 = ( 2  eta . ( eta_sq + 3  si ^2) . ( cosh ( si  h ) − eta_cosh ) + eta_msq . ( h
          ( eta_sq + si ^2) . eta_sinh + 2  si  h  eta  sinh ( si  h ) ) ) . / eta_msq3 ;
99    I8 = ( 2  si  ( 3  eta_sq + si ^2)  sinh ( si  h ) − 2  eta . ( eta_sq + 3  si ^2) .
          eta_sinh + h  ( eta_sq .^2 − si ^4) . ( cosh ( si  h ) + eta_cosh ) ) . /
          eta_msq3 ;
100   I9 = eta . ( eta_cosh − cosh ( si  h ) ) . / eta_msq ;
101   I10 = ( eta . eta_sinh − si  sinh ( si  h ) ) . / eta_msq ;
102   I11 = eta . ( 2  si  ( eta_cosh − cosh ( si  h ) ) − eta_msq  h  sinh ( si  h ) ) . /
          eta_msq2 ;
103   I12 = ( 2  si  eta . eta_sinh − ( eta_sq + si ^2) . sinh ( si  h ) − si  h
          eta_msq  cosh ( si  h ) ) . / eta_msq2 ;
104   I13 = ( 2  eta . si  sinh ( si  h ) − ( eta_sq + si ^2) . eta_sinh + eta . h .
          eta_msq . eta_cosh ) . / eta_msq2 ;
105   I14 = ( h  eta . eta_msq . eta_sinh − ( eta_sq + si ^2) . ( eta_cosh − cosh (
          si  h ) ) ) . / eta_msq2 ;
106   I15 = 2 ( si  h  eta . eta_msq . ( eta_cosh + cosh ( si  h ) ) + eta . ( eta_sq +
          3  si ^2) . sinh ( si  h ) − si  ( 3  eta_sq + si ^2) . eta_sinh ) . / eta_msq3 ;
107   I16 = ( 2  si  ( 3  eta_sq + si ^2) . ( cosh ( si  h ) − eta_cosh ) + h  eta_msq
          . ( 2  si  eta . eta_sinh + ( eta_sq + si ^2) . sinh ( si  h ) ) ) . / eta_msq3 ;
108   %psi0 = ( − sinh ( st ) + st  cosh ( st ) ) ;
109   chi0_1 = 2  eta_sq . ( eta_C0 . ( − I1 + si  I3 ) + eta_D0 . ( − I2 + si  I4 ) ) ;
110   chi0_2 = 2  eta_sq . ( eta_C0 . ( − I6 + si  I8 ) + eta_D0 . ( − I5 + si  I7 ) )
          ...
111       + 2  eta_sD0 . ( − I2 + si  I4 ) ;
112   %psi1 = st  sinh ( st ) ;
113   chi1_1 = 2  si  eta_sq . ( eta_C0 . I11 + eta_D0 . I12 ) ;
```

122

```matlab
114        chi1_2 = 2 si eta_sq . ( eta_C0 . I16 + eta_D0 . I15) + 2 si eta_sD0 . I12
               ;
115        %psi2 = sinh(st) + st cosh(st);
116        chi2_1 = 2 eta_sq . ( eta_C0 . ( I1 + si I3) + eta_D0 . ( I2 + si I4));
117        chi2_2 = 2 eta_sq . ( eta_C0 . ( I6 + si I8) + eta_D0 . ( I5 + si I7)) ...
118            + 2 eta_sD0 . ( I2 + si I4);
119        %psi3 = 2 cosh(st) + st sinh(st);
120        chi3_1 = 2 eta_sq . ( eta_C0 . ( 2 I9 + si I11) + eta_D0 . ( 2 I10 + si I12
               ));
121        chi3_2 = 2 eta_sq . ( eta_C0 . ( 2 I14 + si I16) + eta_D0 . ( 2 I13 + si
               I15)) ...
122            + 2 eta_sD0 . ( 2 I10 + si I12);

124        CHI = [ chi0_1; chi0_2; chi1_1; chi1_2; chi2_1; chi2_2; chi3_1; chi3_2 ];

126        %singularity at midi eta=si
127        CHI(: , midi) = (4 (CHI(: , midi−1)+CHI(: , midi+1)) − (CHI(: , midi−2)+CHI
               (: , midi+2))) ./6;
128        if isnan (CHI(1 , midi)) == 1%isnan ( chi0_1 ( midi)) == 1
129            CHI(: , midi) = (CHI(: , midi+1) + CHI(: , midi−1))/2;
130        end

132        %singularity eta = −si ( only if in conv_rad)
133        %i0 = find ( isnan ( real ( chi0_1)));
134        i0 = find ( isnan ( real (CHI(1 ,:))));
135        if isempty (i0) == 0
136        if (i0==1 || i0==2) == 1
137            CHI(: , i0) = (4 CHI(: , i0 +1) − CHI(: , i0 +2))./3;
138        elseif (i0 == conv_n || i0 == conv_n−1) == 1
139            CHI(: , i0) = (4 CHI(: , i0 −1) − CHI(: , i0 −2))./3;
140        else
141            CHI(: , i0) = (4 (CHI(: , i0 −1)+CHI(: , i0 +1)) − (CHI(: , i0 −2)+CHI(: , i0
                   +2)))./6;
142        end
143        end
```

```matlab
144
145         sconv0_integrand = 1i./(4 pi Gbar si^2).(-2 FT_Gtp_conv.CHI(1,:) +
                sFT_Gtp_conv.CHI(2,:));
146         sconv1_integrand = 1i./(4 pi Gbar si^2).(-2 FT_Gtp_conv.CHI(3,:) +
                sFT_Gtp_conv.CHI(4,:));
147         sconv2_integrand = 1i./(4 pi Gbar si^2).(-2 FT_Gtp_conv.CHI(5,:) +
                sFT_Gtp_conv.CHI(6,:));
148         sconv3_integrand = 1i./(4 pi Gbar si^2).(-2 FT_Gtp_conv.CHI(7,:) +
                sFT_Gtp_conv.CHI(8,:));
149
150 %       F0(i) = conv_W sconv0_integrand';
151 %       F1(i) = conv_W sconv1_integrand';
152 %       F2(i) = conv_W sconv2_integrand';
153 %       F3(i) = conv_W sconv3_integrand';
154         F0(i) = sum(conv_W.sconv0_integrand);
155         F1(i) = sum(conv_W.sconv1_integrand);
156         F2(i) = sum(conv_W.sconv2_integrand);
157         F3(i) = sum(conv_W.sconv3_integrand);
158
159 end
160
161 F0_r = real(F0); F0_i = imag(F0);
162 F1_r = real(F1); F1_i = imag(F1);
163
164 Dw0hat = s.(C0.(psi2_h+psi0_h) + D0_2.psi1_h) + sD0.psi3_h;
165 Lw0hat = s.^2.(C0.(psi3_h-psi1_h) + D0_2.(psi4_h-psi2_h));
166 dzw0hat = s.(C0.psi1_h + D0_2.psi2_h);
167
168 M1_conv = 1i./(2 pi) ds.conv(FT_Gtp_sinv,Dw0hat,'same');
169 N1_conv = 1i./(2 pi) ds.(2 conv(FT_Gtp_sinv,dzw0hat,'same') - 1./s.(
        conv(FT_Gtp_sinv,Lw0hat,'same') ...
170         - 2 conv(FT_Gtp,dzw0hat,'same')));
171
172 M1 = M1_conv(midi:midi+m-conv_n) - Gbar s_short.(F2 + F0) - k_sq Ups
        s_short.^2.F1;
```

124

```matlab
173   N1 = N1_conv(midi:midi+m-conv_n) - Gbar s_short.(3 F1 - F3) - Ups
          s_short.^2. F0;
174   M1_r = real(M1); M1_i = imag(M1);
175   N1_r = real(N1); N1_i = imag(N1);
176
177   m0s = find(s_short==0);
178
179   C1_r = (mu2(s_ind). M1_r - beta2(s_ind). N1_r)./denom(s_ind); %odd ~1/s
180   C1_i = (mu2(s_ind). M1_i - beta2(s_ind). N1_i)./denom(s_ind); C1_i(m0s) =
          (4 C1_i(m0s+1) - C1_i(m0s+2))/3; %even
181   D1_r = (beta1(s_ind). N1_r - mu1(s_ind). M1_r)./denom(s_ind); D1_r(m0s) =
          (4 D1_r(m0s+1) - D1_r(m0s+2))/3; %even
182   D1_i = (beta1(s_ind). N1_i - mu1(s_ind). M1_i)./denom(s_ind); D1_i(m0s) =
          0; %odd
183
184   sC1_r = s_short. C1_r; sC1_r(m0s) = (4 sC1_r(m0s+1) - sC1_r(m0s+2))/3;
185
186   uhat1_r = -C1_i. psi1_h(s_ind) - D1_i. psi2_h(s_ind) - F1_i; uhat1_r(m0s)
          = (4 uhat1_r(m0s+1) - uhat1_r(m0s+2))/3;
187   uhat1_i = C1_r. psi1_h(s_ind) + D1_r. psi2_h(s_ind) + F1_r; uhat1_i(m0s)
          = 0;
188   what1_r = C1_r. psi0_h(s_ind) + D1_r. psi1_h(s_ind) + F0_r; what1_r(m0s)
          = (4 what1_r(m0s+1) - what1_r(m0s+2))/3;
189   what1_i = C1_i. psi0_h(s_ind) + D1_i. psi1_h(s_ind) + F0_i; what1_i(m0s)
          = 0;
190
191   u1 = zeros(1,n); w1 = u1; xsind = 1:((m-conv_n)/2 + 1);
192   W2 = 2/3(1+(mod(xsind,2)==0)); W2(1) = 1/3; W2(end) = 1/3;
193   for i=1:n
194       wt = (what1_r(m0s:end). cos(xs(i,xsind)) - what1_i(m0s:end). sin(xs(i
              ,xsind)))/pi;
195       ut = (uhat1_r(m0s:end). cos(xs(i,xsind)) - uhat1_i(m0s:end). sin(xs(i
              ,xsind)))/pi;
196       w1(i) = ds sum(W2. wt);
197       u1(i) = ds sum(W2. ut);
```

125

```matlab
198    end
199
200    u_FT = u0+c u1; w_FT = w0+c w1;
201    end
202    %CALCULATING ELASTIC ENERGY
203
204    % zc = h/2; zn1 = 10; zn2 = 12; zn = zn1+zn2;
205    % [nodes1,weights1] = lgwt(zn1,0,zc);
206    % d = 0; power = 1;
207    % [nodes2,weights2] = lgwt(zn2,(zc-d)^power,(h-d)^power);
208    % weights2 = nodes2.^(1/power-1). weights2/power; nodes2 = nodes2.^(1/
            power) + d;
209    % nodes = [flipud(nodes1);flipud(nodes2)]'; weights = [flipud(weights1);
            flipud(weights2)];
210
211    zn = 10;
212    [nodes,weights] = lgwt(zn,0,h);
213    nodes = flipud(nodes)'; weights = flipud(weights);
214
215    dEz = zeros(1,zn);
216    if c~=0
217    W3 = 2/3(1+(mod(1:m-conv_n+1,2)==0)); W3(1) = 1/3; W3(end) = 1/3;
218    else
219    W3 = 2/3(1+(mod(1:m,2)==0)); W3(1) = 1/3; W3(end) = 1/3;
220    end
221
222    for i=1:zn
223
224    zi = nodes(i);
225
226    sinhsz = sinh(zi s); coshsz = cosh(zi s);
227    psi0 = -sinh(s zi) + zi s . cosh(s zi);
228    psi1 = zi s . sinh(s zi);
229    psi2 = sinh(s zi) + zi s . cosh(s zi);
230    psi3 = zi s . sinh(s zi) + 2 cosh(s zi);
```

126

```matlab
231
232   if c~=0
233   F0z = zeros(1,m-conv_n+1); F1z = F0z; F2z = F0z;
234   for j=1:m-conv_n+1
235       index = midi + (j-1);
236       sj = s(index);
237       eta = s(j:j+conv_n-1); eta_sq = s_sq(j:j+conv_n-1);
238       eta_sinh = sinhsz(j:j+conv_n-1); eta_cosh = coshsz(j:j+conv_n-1);
239 %       eta_C0 = C0(j:j+conv_n-1)./eta_cosh;
240 %       eta_D0 = D0_2(j:j+conv_n-1)./eta_cosh;
241 %       eta_sD0 = sD0(j:j+conv_n-1)./eta_cosh;
242       eta_C0 = C0(j:j+conv_n-1)./coshsh(j:j+conv_n-1);
243       eta_D0 = D0_2(j:j+conv_n-1)./coshsh(j:j+conv_n-1);
244       eta_sD0 = sD0(j:j+conv_n-1)./coshsh(j:j+conv_n-1);
245       eta_msq = eta_sq - sj^2; eta_msq2 = eta_msq.^2; eta_msq3 = eta_msq.
           eta_msq2;
246
247       I1 = (sj. eta_sinh - eta. sinh(sj zi))./eta_msq;
248       I2 = sj. (eta_cosh - cosh(sj zi))./eta_msq;
249       I3 = ((eta_sq + sj^2). eta_sinh - 2 eta sj sinh(sj zi) - eta_msq. eta
            zi cosh(sj zi))./eta_msq2;
250       I4 = ((eta_sq + sj^2). (eta_cosh - cosh(sj zi)) - sj zi eta_msq. sinh
           (sj zi))./eta_msq2;
251       I5 = (2 sj eta. (cosh(sj zi) - eta_cosh) + sj zi eta_msq. eta_sinh)./
           eta_msq2;
252       I6 = ((eta_sq + sj^2) sinh(sj zi) - 2 sj eta. eta_sinh + sj zi
           eta_msq. eta_cosh)./eta_msq2;
253       I7 = (2 eta. (eta_sq + 3 sj^2). (cosh(sj zi) - eta_cosh) + eta_msq. (
           zi (eta_sq + sj^2). eta_sinh + 2 sj zi eta sinh(sj zi)))./
           eta_msq3;
254       I8 = (2 sj (3 eta_sq + sj^2) sinh(sj zi) - 2 eta. (eta_sq + 3 sj^2).
           eta_sinh + zi (eta_sq.^2 - sj^4). (cosh(sj zi) + eta_cosh))./
           eta_msq3;
255 %     I9 = eta. (eta_cosh - cosh(sj zi))./eta_msq;
256 %     I10 = (eta. eta_sinh - sj sinh(sj zi))./eta_msq;
```

127

```matlab
257     I11 = eta.(2 sj (eta_cosh - cosh(sj zi)) - eta_msq zi sinh(sj zi))./
            eta_msq2;
258     I12 = (2 sj eta.eta_sinh - (eta_sq + sj^2).sinh(sj zi) - sj zi
            eta_msq cosh(sj zi))./eta_msq2;
259 %    I13 = (2 eta.sj sinh(sj zi) - (eta_sq + sj^2).eta_sinh + eta.zi.
        eta_msq.eta_cosh)./eta_msq2;
260 %    I14 = (zi eta.eta_msq.eta_sinh - (eta_sq + sj^2).(eta_cosh - cosh
        (sj zi)))./eta_msq2;
261     I15 = 2(sj zi eta.eta_msq.(eta_cosh + cosh(sj zi)) + eta.(eta_sq
            + 3 sj^2).sinh(sj zi) - sj (3 eta_sq + sj^2).eta_sinh)./
            eta_msq3;
262     I16 = (2 sj (3 eta_sq + sj^2).(cosh(sj zi) - eta_cosh) + zi eta_msq
            .(2 sj eta.eta_sinh + (eta_sq + sj^2).sinh(sj zi)))./eta_msq3;
263
264     %psi0 = (-sinh(st) + st cosh(st));
265     chi0_1 = 2 eta_sq.(eta_C0.(-I1 + sj I3) + eta_D0.(-I2 + sj I4));
266     chi0_2 = 2 eta_sq.(eta_C0.(-I6 + sj I8) + eta_D0.(-I5 + sj I7))
            ...
267         + 2 eta_sD0.(-I2 + sj I4);
268     %psi1 = st sinh(st);
269     chi1_1 = 2 sj eta_sq.(eta_C0.I11 + eta_D0.I12);
270     chi1_2 = 2 sj eta_sq.(eta_C0.I16 + eta_D0.I15) + 2 sj eta_sD0.I12
            ;
271     %psi2 = sinh(st) + st cosh(st);
272     chi2_1 = 2 eta_sq.(eta_C0.(I1 + sj I3) + eta_D0.(I2 + sj I4));
273     chi2_2 = 2 eta_sq.(eta_C0.(I6 + sj I8) + eta_D0.(I5 + sj I7)) ...
274         + 2 eta_sD0.(I2 + sj I4);
275
276     CHI = [chi0_1;chi0_2;chi1_1;chi1_2;chi2_1;chi2_2];
277
278     %singularity at midi eta=si
279     CHI(:,midi) = (4 (CHI(:,midi-1)+CHI(:,midi+1)) - (CHI(:,midi-2)+CHI
            (:,midi+2)))./6;
280     if isnan(CHI(1,midi)) == 1%isnan(chi0_1(midi)) == 1
281         CHI(:,midi) = (CHI(:,midi+1) + CHI(:,midi-1))/2;
```

128

```matlab
282        end
283
284        %singularity eta = −si (only if in conv_rad)
285        %i0 = find(isnan(real(chi0_1)));
286        i0 = find(isnan(real(CHI(1,:))));
287        if isempty(i0) == 0
288        if (i0==1 || i0==2) == 1
289            CHI(:,i0) = (4 CHI(:,i0+1) − CHI(:,i0+2))./3;
290        elseif (i0 == conv_n || i0 == conv_n−1) == 1
291            CHI(:,i0) = (4 CHI(:,i0−1) − CHI(:,i0−2))./3;
292        else
293            CHI(:,i0) = (4 (CHI(:,i0−1)+CHI(:,i0+1)) − (CHI(:,i0−2)+CHI(:,i0
                +2)))./6;
294        end
295        end
296        %CHI = 0 CHI;
297
298        sconv0_integrand = 1i ./(4 pi Gbar sj^2).(−2 FT_Gtp_conv. CHI(1,:) +
                sFT_Gtp_conv. CHI(2,:));
299        sconv1_integrand = 1i ./(4 pi Gbar sj^2).(−2 FT_Gtp_conv. CHI(3,:) +
                sFT_Gtp_conv. CHI(4,:));
300        sconv2_integrand = 1i ./(4 pi Gbar sj^2).(−2 FT_Gtp_conv. CHI(5,:) +
                sFT_Gtp_conv. CHI(6,:));
301
302 %      F0z(i) = conv_W sconv0_integrand';
303 %      F1z(i) = conv_W sconv1_integrand';
304 %      F2z(i) = conv_W sconv2_integrand';
305        F0z(j) = sum(conv_W. sconv0_integrand);
306        F1z(j) = sum(conv_W. sconv1_integrand);
307        F2z(j) = sum(conv_W. sconv2_integrand);
308 end
309 F0z(m0s) = .5 (F0z(m0s+1)+F0z(m0s−1));
310 F1z(m0s) = .5 (F1z(m0s+1)+F1z(m0s−1));
311 F2z(m0s) = .5 (F2z(m0s+1)+F2z(m0s−1));
312
```

```
313  swhatz_r = s_short . ( ( C0_r ( s_ind ) ) . psi0 ( s_ind ) + ( D0_r ( s_ind ) + c D1_r )
        . psi1 ( s_ind ) ) . / coshsh ( s_ind ) + c sC1_r . psi0 ( s_ind ) . / coshsh ( s_ind ) +
        c s_short . real ( F0z ) ;
314  swhatz_i = s_short . ( ( C0_i ( s_ind ) + c C1_i ) . psi0 ( s_ind ) + ( D0_i2 ( s_ind )
        + c D1_i ) . psi1 ( s_ind ) ) . / coshsh ( s_ind ) + c s_short . imag ( F0z ) ;
315  dzwhatz_r = s_short . ( ( C0_r ( s_ind ) ) . psi1 ( s_ind ) + ( D0_r ( s_ind ) + c D1_r )
        . psi2 ( s_ind ) ) . / coshsh ( s_ind ) + c sC1_r . psi1 ( s_ind ) . / coshsh ( s_ind ) +
        c s_short . real ( F1z ) ;
316  dzwhatz_i = s_short . ( ( C0_i ( s_ind ) + c C1_i ) . psi1 ( s_ind ) + ( D0_i2 ( s_ind )
        + c D1_i ) . psi2 ( s_ind ) ) . / coshsh ( s_ind ) + c s_short . imag ( F1z ) ;
317  dzuhatz_r = −s_short . ( ( C0_i ( s_ind ) + c C1_i ) . psi2 ( s_ind ) + ( c D1_i ) .
        psi3 ( s_ind ) ) . / coshsh ( s_ind ) − imag ( sD0 ( s_ind ) ) . psi3 ( s_ind ) . / coshsh (
        s_ind ) − c s_short . imag ( F2z ) ;
318  dzuhatz_i = s_short . ( ( C0_r ( s_ind ) ) . psi2 ( s_ind ) + ( D0_r ( s_ind ) + c D1_r )
        . psi3 ( s_ind ) ) . / coshsh ( s_ind ) + c sC1_r . psi2 ( s_ind ) . / coshsh ( s_ind ) +
        c s_short . real ( F2z ) ;
319  end
320  if c==0
321  swhatz_r = s . ( C0_r . psi0 + D0_r . psi1 ) . / coshsh ;
322  swhatz_i = s . ( C0_i . psi0 + D0_i2 . psi1 ) . / coshsh ;
323  dzwhatz_r = s . ( C0_r . psi1 + D0_r . psi2 ) . / coshsh ;
324  dzwhatz_i = s . ( C0_i . psi1 + D0_i2 . psi2 ) . / coshsh ;
325  dzuhatz_r = −( s . C0_i . psi2 + imag ( sD0 ) . psi3 ) . / coshsh ;
326  dzuhatz_i = s . ( C0_r . psi2 + D0_r . psi3 ) . / coshsh ;
327  end
328
329  dzwhatconv = ds conv ( ( dzwhatz_r + 1i dzwhatz_i ) , ( dzwhatz_r + 1i dzwhatz_i
        ) , 'same' ) ;
330  shearconv = ds conv ( ( dzuhatz_r − swhatz_i + 1i ( dzuhatz_i + swhatz_r ) ) , (
        dzuhatz_r − swhatz_i + 1i ( dzuhatz_i + swhatz_r ) ) , 'same' ) ;
331  dzwhatmag_sq = dzwhatz_r .^2 + dzwhatz_i .^2 ;
332  shearmag_sq = ( dzuhatz_r − swhatz_i ) .^2 + ( dzuhatz_i + swhatz_r ) .^2 ;
333
334  E_sintegrand = Gbar ( 4 dzwhatmag_sq + shearmag_sq ) ; % + c / ( 2 pi ) FT_Gtp (
        s_ind ) . fliplr ( real ( 4 dzwhatconv + shearconv ) ) ;
```

130

```
335    if c~=0
336    E_sintegrand = E_sintegrand + c/(2 pi) FT_Gtp_sinv(s_ind). fliplr(imag(4
           dzwhatconv + shearconv));
337    dEz(i) = ds sum(W3. E_sintegrand)/(4 pi);
338    %dEz(i) = ds sum(W3. E_sintegrand)/(4 pi) + Gbar (4 dzwhatconv(m0s) +
           shearconv(m0s))/(4 pi);
339    else
340    dEz(i) = ds sum(W3. E_sintegrand)/(4 pi);
341    end
342
343    end
344    %COMMENT WHEN RUNNING MIN CODE:
345    % figure
346    % plot(nodes,dEz)
347
348    E_elastic = dEz weights;
349
350    %SURFACE ENERGY
351    if c==0
352        u_FT = u0; w_FT = w0;
353        u1 = 0 u0; w1 = 0 w0;
354    end
355    n_cl = find(abs(abs(x)−R) < 1e−2); n1 = min(n_cl); n2 = max(n_cl);
356    x_sg1 = x(1:n1) + u_FT(1:n1); x_ls = x(n1:n2) + u_FT(n1:n2); x_sg2 = x(n2
           :n) + u_FT(n2:n);
357    z_sg1 = w_FT(1:n1); z_ls = w_FT(n1:n2); z_sg2 = w_FT(n2:n);
358    L_sg = parametric_arclength2(x_sg1,z_sg1) + parametric_arclength2(x_sg2,
           z_sg2);
359    L_ls = parametric_arclength2(x_ls,z_ls);
360
361    %E_surface = gam Ldrop + Ups (L_ls + L_sg − 2 X R);
362    %E_surface = gam Ldrop;
363    E_surface = Ups (L_ls + L_sg − 2 X R);
364
365    Etot = E_elastic + E_surface;
```

```matlab
366
367  TIME = toc;
368
369  data.params = params;
370  data.alpha = alpha;
371  data.det_params = [k_sq, fl, fr, R, PI, Ldrop, L_sg, L_ls, abs(Fdrop_param), zn];
372  data.energy = [Etot, E_elastic, E_surface];
373  data.pos = [x; u0; w0; u1; w1; u_FT; w_FT];
374  data.GL_nwd = [nodes; weights'; dEz];
375  data.time = TIME;
376
377  disp([Etot/10000, al, ar]);
```

Matlab code for obtaining energy minimizing droplet contact angles for the case of a surface energy gradient (§5.7)

```matlab
function [Etot, data] = surfgrad_energy(alpha, params)
tic;

h = params(1);
A = params(2);
G = params(3);
c = params(4);
L = params(5);
gam_l = params(6);
gam_s_bar = params(7);
k_sq = gam_l^2/(4 gam_s_bar^2 - gam_l^2);

al = alpha(1);
ar = alpha(2);

fl = gam_l cos(al); fr = gam_l cos(ar);
[Ldrop,R,Fdrop_param] = polar_arclength(al,ar,A);
PI = gam_l (sin(al)+sin(ar))/(2 R);

dx = R/floor(R); X = 7;
x = -X R:dx:X R; n = length(x);

S = 10; ds = .001;
s = -S:ds:S; m = length(s); m0 = find(s==0);
sh = s h; sR = s R; s_sq = s.^2;
tanhsh = tanh(sh); coshsh = cosh(sh); %sinhsh = sinh(sh);

xs = zeros(n,m-m0+1);
for i = 1:n
    xs(i,:) = s(m0:end) . x(i);
end
```

```matlab
M_r = (fl+fr) sin(sR);
M_i = (fr-fl) cos(sR);
N_r = gam_l (sin(al)+sin(ar)) cos(sR) - 2 PI sin(sR)./s; N_r(1) = 0;
N_i = gam_l (sin(al)-sin(ar)) sin(sR);

psi0_h = -tanhsh + sh;
psi1_h = sh. tanhsh;
psi2_h = sh + tanhsh;
psi3_h = sh. tanhsh + 2;
psi4_h = sh + 3 tanhsh;

beta1 = G s. (psi0_h+psi2_h) + k_sq gam_s_bar s.^2. psi1_h;
beta2 = G s. (psi1_h+psi3_h) + k_sq gam_s_bar s.^2. psi2_h;
mu1 = G s. (3 psi1_h-psi3_h) + gam_s_bar s.^2. psi0_h;
mu2 = G s. (3 psi2_h-psi4_h) + gam_s_bar s.^2. psi1_h;
denom = beta1. mu2 - beta2. mu1;

C0_r = (mu2. M_r - beta2. N_r)./denom; C0_r(m0) = 0;
C0_i = (mu2. M_i - beta2. N_i)./denom; C0_i(m0) = -(gam_l R (sin(al)-sin(
    ar))-h (fr-fl))/(2 G);
D0_r = (beta1. N_r - mu1. M_r)./denom; D0_r(m0) = R (fl+fr)/(2 G);
D0_i = (beta1. N_i - mu1. M_i)./denom; %D0_i scales like (fr-fl)/(2 G s)
    for small s, limit adjustments in transforms
%D0_i2 = D0_i; D0_i2(m0) = 0; %used for simplicity for calculations where
    multiplied by s^k (k>1)
%C0 is (odd) + i(even), D0 is (even) + i(odd)

uhat0_r = -C0_i. psi1_h - D0_i. psi2_h; uhat0_r(m0) = -C0_i(m0) psi1_h(m0
    ) - h (fr-fl)/G;
uhat0_i = C0_r. psi1_h + D0_r. psi2_h;
what0_r = C0_r. psi0_h + D0_r. psi1_h;
what0_i = C0_i. psi0_h + D0_i. psi1_h; what0_i(m0) = 0;%C0_i(m0) psi0_h(
    m0);

W = 2/3 (1+(mod(1:m-m0+1,2)==0)); W(1) = 1/3; W(end) = 1/3;
```

134

```matlab
63
64  u0 = zeros(1,n); w0 = u0;
65  for i=1:n
66      wt = (what0_r(m0:m) . cos(xs(i,:)) − what0_i(m0:m) . sin(xs(i,:)))/pi;
67      ut = (uhat0_r(m0:m) . cos(xs(i,:)) − uhat0_i(m0:m) . sin(xs(i,:)))/pi;
68      w0(i) = ds W wt';
69      u0(i) = ds W ut';
70  end
71
72  %C0 = C0_r + 1i C0_i; D0 = D0_r + 1i D0_i; D0_2 = D0_r + 1i D0_i2; sD0 =
        s . D0; sD0(m0) = 1i (fr−fl)/(2 G);
73  FT_gamSp = 2 exp(−abs(s) L); FT_gamSp_sinv = FT_gamSp./s; FT_gamSp_sinv(
        m0) = 0;
74
75  is_squhat0 = s_sq . (−uhat0_i + 1i uhat0_r);
76  s_sqwhat0 = s_sq . (what0_r + 1i what0_i);
77  M1 = −1i k_sq/(2 pi) ds conv(FT_gamSp_sinv, is_squhat0 , 'same');
78  N1 = 1i/(2 pi) ds conv(FT_gamSp_sinv, s_sqwhat0 , 'same');
79
80  C1 = (mu2 . M1 − beta2 . N1)./denom; C1(m0) = (4 (C1(m0+1)+C1(m0−1)) − (C1(
        m0+2)+C1(m0−2)))/6;
81  D1 = (beta1 . N1 − mu1 . M1)./denom; D1(m0) = (4 (D1(m0+1)+D1(m0−1)) − (D1(
        m0+2)+D1(m0−2)))/6;
82
83  uhat1 = 1i (C1 . psi1_h + D1 . psi2_h);
84  what1 = (C1 . psi0_h + D1 . psi1_h);
85
86  u1 = zeros(1,n); w1 = u1;
87  for i=1:n
88      wt = (real(what1(m0:m)) . cos(xs(i,:)) − imag(what1(m0:m)) . sin(xs(i
          ,:)))/pi;
89      ut = (real(uhat1(m0:m)) . cos(xs(i,:)) − imag(uhat1(m0:m)) . sin(xs(i
          ,:)))/pi;
90      w1(i) = ds W wt';
91      u1(i) = ds W ut';
```

```matlab
92   end
93
94   u = u0 + c u1;
95   w = w0 + c w1;
96   % figure
97   % plot(x+u,w)
98   % figure
99   % plot(x,u1)
100  % figure
101  % plot(x,w1)
102
103  sC0 = s . ( C0_r + 1i  C0_i ) ;
104  sD0 = s . ( D0_r + 1i  D0_i ) ; sD0(m0) = ( 4 ( sD0(m0+1)+sD0(m0−1)) − (sD0(m0
         +2)+sD0(m0−2)))/6;
105  sC1 = s . C1 ; sC1(m0) = ( 4 ( sC1(m0+1)+sC1(m0−1)) − (sC1(m0+2)+sC1(m0−2)))
         /6;
106  sD1 = s . D1 ; sD1(m0) = ( 4 ( sD1(m0+1)+sD1(m0−1)) − (sD1(m0+2)+sD1(m0−2)))
         /6;
107  sC = sC0 + c  sC1 ; sD = sD0 + c  sD1 ;
108
109  zn = 15;
110  [ nodes , weights ] = lgwt ( zn , 0 , h ) ;
111  dEz = zeros (1 , zn ) ;
112  for  i =1:zn
113
114  zi = nodes ( i ) ;
115
116  sinhsz = sinh ( zi  s ) ; coshsz = cosh ( zi  s ) ;
117  psi0 = −sinhsz + zi  s . coshsz ;
118  psi1 = zi  s . sinhsz ;
119  psi2 = sinhsz + zi  s . coshsz ;
120  psi3 = zi  s . sinhsz + 2 coshsz ;
121
122  tauhat_n = ( sC . psi1 + sD . psi2 )./ coshsh ;
123  tauhat_s = 1i ( sC . ( psi2 + psi0 ) + sD . ( psi3 + psi1 ))./ coshsh ;
```

```
124  tauhat_n_conv = ds sum(tauhat_n . fliplr (tauhat_n));
125  tauhat_s_conv = ds sum(tauhat_s . fliplr (tauhat_s));
126
127  dEz(i) = G/(4 pi) real (4 tauhat_n_conv + tauhat_s_conv);
128  end
129
130  E_elastic = real (dEz weights);
131
132  n_cl = find (abs(abs(x)−R) < 1e−2); n1 = min(n_cl); n2 = max(n_cl);
133  x_sg1 = x(1:n1) + u(1:n1); x_ls = x(n1:n2) + u(n1:n2); x_sg2 = x(n2:n) +
         u(n2:n);
134  z_sg1 = w(1:n1); z_ls = w(n1:n2); z_sg2 = w(n2:n);
135  E_sg = surfenergy_surfgrad (x_sg1 , z_sg1 , gam_s_bar , c , L) +
         surfenergy_surfgrad (x_sg2 , z_sg2 , gam_s_bar , c , L);
136  E_ls = surfenergy_surfgrad (x_ls , z_ls , gam_s_bar , c , L);
137
138  E_surface = gam_l Ldrop + E_sg + E_ls − gam_s_bar 2 X R;
139
140  Etot = E_elastic + E_surface;
141
142  TIME = toc;
143
144  data.params = params;
145  data.alpha = alpha;
146  data.det_params = [k_sq , fl , fr , R, PI , Ldrop , E_sg , E_ls , abs(Fdrop_param) ,zn ];
147  data.energy = [Etot , E_elastic , E_surface ];
148  data.pos = [x;u0;w0;u1;w1;u;w];
149  data.GL_nwd = [nodes '; weights '; dEz ];
150  data.time = TIME;
151
152  disp ([ Etot /10000, al , ar ]);
153
154  end
```

Matlab code for Computing droplet velocity by balancing energy release with dissipation (§6.4)

```
1  %clear , clc
2  %close all
3
4  %Pm/Pd function of a = G' R/Gbar (migration over dissipation)
5  %STANDARD VALUES: G' = .005 [kPa/um], R = 100 [um], Gbar = 20kPa (a =
        .025)
6  %Cover 0.005 < a < .5 (or higher) by individually varying all values in a
7  %plot Pr, Pd, and Pr/Pd for all cases using various combinations of
8  %supplementary parameters
9
10 %R: [20 50 100 200 500] .005 < a < .125
11 %Gp: [.001 .002 .005 .01 .03 .1] .005 < a < .5
12 %G: [100 40 20 10 5 2 1] .005 < a < .5
13 %RECORD VECTORS P(m/d)_(R/Gp/G)_(trial#) and a_(R/Gp/G)_(trial#)
14
15  tic ;
16
17 %Parameters
18 h = 50;
19 R = sqrt (1200) ;
20 G = 1; Gp = −0.0084345;
21 gam = 64;
22 Ups = 40; Up = 0; %Up = 2a/(pi L) = 2 (percent) Ups/(pi L)
23 t_visc = .03;
24 n_visc = .667;
25 v = 2.96;
26
27 alpha_l = pi/2; sal = sin (alpha_l) ;
28 alpha_r = pi/2; sar = sin (alpha_r) ;
29 k_sq = gam^2/(4 Ups^2 − gam^2) ;
30 fl = gam cos (alpha_l) ; fr = gam cos (alpha_r) ;
31 Ldrop = pi R^2;
32
```

```matlab
33  dt = .0001; %seconds
34
35  S = min([floor(700/h),40]); ds = 1e-3;
36  s = -S:ds:S; m = length(s); m0 = find(s==0);
37
38  dx = R/floor(R); X = 5;
39  x = -X R:dx:X R; n = length(x);
40
41  sh = s h; sR = s R; s_sq = s.^2;
42  tanhsh = tanh(sh); omega = -s v;
43  G_complex = G(1+(1i t_visc omega).^n_visc);
44  G_complex_dt = (G+Gp v dt)(1+(1i t_visc omega).^n_visc);
45
46  xs = zeros(n,m);
47  for i = 1:n
48      xs(i,:) = s. x(i);
49  end
50
51  psi0_h = -tanhsh + sh;
52  psi1_h = sh. tanhsh;
53  psi2_h = sh + tanhsh;
54  psi3_h = sh. tanhsh + 2;
55  psi4_h = sh + 3 tanhsh;
56
57  N = gam ((sal+sar) cos(sR) + 1i (sal-sar) sin(sR) - (sal+sar) sin(sR)./sR
        ); N(m0) = 0;
58  M = (fl+fr) sin(sR) + 1i (fr-fl) cos(sR);
59
60  beta = s. G_complex. (psi0_h + psi2_h) + k_sq Ups s_sq. psi1_h;
61  betap = s. G_complex. (psi1_h + psi3_h) + k_sq Ups s_sq. psi2_h;
62  mu = s. G_complex. (3 psi1_h - psi3_h) + Ups s_sq. psi0_h;
63  mup = s. G_complex. (3 psi2_h - psi4_h) + Ups s_sq. psi1_h;
64  denom = beta. mup - betap. mu;
65
66  beta_dt = s. G_complex_dt. (psi0_h + psi2_h) + k_sq (Ups-Up v dt) s_sq.
```

139

```matlab
            psi1_h ;
67  betap_dt = s . G_complex_dt . ( psi1_h + psi3_h ) + k_sq ( Ups−Up v dt) s_sq .
            psi2_h ;
68  mu_dt = s . G_complex_dt . ( 3 psi1_h − psi3_h ) + (Ups−Up v dt) s_sq . psi0_h
            ;
69  mup_dt = s . G_complex_dt . ( 3 psi2_h − psi4_h ) + (Ups−Up v dt) s_sq .
            psi1_h ;
70  denom_dt = beta_dt . mup_dt − betap_dt . mu_dt;
71
72  FTu = 1i ((mup. M−betap . N) . psi1_h+(beta . N−mu. M) . psi2_h)./denom; FTu(
            m0) = (4 FTu(m0+1) − FTu(m0+2))/3;
73  FTw = ((mup. M−betap . N) . psi0_h+(beta . N−mu. M) . psi1_h)./denom; FTw(m0)
            = (4 FTw(m0+1) − FTw(m0+2))/3;
74
75  FTu_real = real(FTu); FTu_imag = imag(FTu);
76  FTw_real = real(FTw); FTw_imag = imag(FTw);
77
78  FTu_dt = 1i (( mup_dt. M−betap_dt. N) . psi1_h+(beta_dt . N−mu_dt. M) .
            psi2_h)./denom; FTu_dt(m0) = (4 FTu_dt(m0+1) − FTu_dt(m0+2))/3;
79  FTw_dt = ((mup_dt. M−betap_dt. N) . psi0_h+(beta_dt . N−mu_dt. M) . psi1_h)
            ./denom; FTw_dt(m0) = (4 FTw_dt(m0+1) − FTw_dt(m0+2))/3;
80
81  FTu_real_dt = real(FTu_dt); FTu_imag_dt = imag(FTu_dt);
82  FTw_real_dt = real(FTw_dt); FTw_imag_dt = imag(FTw_dt);
83
84  W = 2/3. (1+(mod(1:m,2)==0)); W(1) = 1/3; W(m) = 1/3;
85  u = zeros(1,n); w = u;
86  u_dt = u; w_dt = u;
87  for i=1:n
88      ut = (FTu_real . cos(xs(i,:)) + FTu_imag . sin(xs(i,:)));
89      wt = (FTw_real . cos(xs(i,:)) + FTw_imag . sin(xs(i,:)));
90      ut_dt = (FTu_real_dt . cos(xs(i,:)) + FTu_imag_dt . sin(xs(i,:)));
91      wt_dt = (FTw_real_dt . cos(xs(i,:)) + FTw_imag_dt . sin(xs(i,:)));
92      u(i) = ds W ut'/(2 pi);
93      w(i) = ds W wt'/(2 pi);
```

```matlab
94      u_dt(i) = ds W ut_dt'/(2 pi);
95      w_dt(i) = ds W wt_dt'/(2 pi);
96  end
97
98  % figure
99  % plot(x,u,x,u_dt)
100 % figure
101 % plot(x,w,x,w_dt)
102
103 sC = s.(mup.M-betap.N)./(denom.cosh(sh));
104 sC(m0) = (4(sC(m0+1)+sC(m0-1))-(sC(m0+2)+sC(m0-2)))/6;
105 sD = s.(beta.N-mu.M)./(denom.cosh(sh));
106 sD(m0) = (4(sD(m0+1)+sD(m0-1))-(sD(m0+2)+sD(m0-2)))/6;
107
108 sC_dt = s.(mup_dt.M-betap_dt.N)./(denom_dt.cosh(sh));
109 sC_dt(m0) = (4(sC_dt(m0+1)+sC_dt(m0-1))-(sC_dt(m0+2)+sC_dt(m0-2)))/6;
110 sD_dt = s.(beta_dt.N-mu_dt.M)./(denom_dt.cosh(sh));
111 sD_dt(m0) = (4(sD_dt(m0+1)+sD_dt(m0-1))-(sD_dt(m0+2)+sD_dt(m0-2)))/6;
112
113 zn = round(h/2);
114 [nodes,weights] = lgwt(zn,0,h);
115 nodes = flipud(nodes); weights = flipud(weights);
116 dEz = zeros(1,zn); dPz = dEz; dEz_dt = dEz;
117 Px = zeros(zn,n);
118
119 for i=1:zn
120     zi = nodes(i);
121
122     sinhsz = sinh(zi s); coshsz = cosh(zi s);
123     psi0 = -sinh(s zi) + zi s.cosh(s zi);
124     psi1 = zi s.sinh(s zi);
125     psi2 = sinh(s zi) + zi s.cosh(s zi);
126     psi3 = zi s.sinh(s zi) + 2 cosh(s zi);
127
128     eps_zz_hat = sC.psi1 + sD.psi2;
```

```matlab
129        eps_xz_hat = .5i (sC. (psi0+psi2) + sD. (psi1+psi3));
130        Leps_zz_hat = (1+(-1i omega t_visc).^n_visc). eps_zz_hat;
131        Leps_xz_hat = (1+(-1i omega t_visc).^n_visc). eps_xz_hat;
132
133        eps_zz_hat_dt = sC_dt. psi1 + sD_dt. psi2;
134        eps_xz_hat_dt = .5i (sC_dt. (psi0+psi2) + sD_dt. (psi1+psi3));
135        Leps_zz_hat_dt = (1+(-1i omega t_visc).^n_visc). eps_zz_hat_dt;
136        Leps_xz_hat_dt = (1+(-1i omega t_visc).^n_visc). eps_xz_hat_dt;
137
138        dEz(i) = ds real(sum(W. (eps_zz_hat. fliplr(Leps_zz_hat) + eps_xz_hat
               . fliplr(Leps_xz_hat))));
139        dPz(i) = -ds imag(sum(W. (s. eps_zz_hat. fliplr(Leps_zz_hat) + s.
               eps_xz_hat. fliplr(Leps_xz_hat))));
140        dEz_dt(i) = ds real(sum(W. (eps_zz_hat_dt. fliplr(Leps_zz_hat_dt) +
               eps_xz_hat_dt. fliplr(Leps_xz_hat_dt))));
141
142
143        %SPATIAL VIEW OF DISSIPATION (not necessary, time consuming,
               uncomment only if you want to)
144 %         Pconv = 1i ds (conv(s. eps_zz_hat,Leps_zz_hat,'same') + conv(s.
       eps_xz_hat,Leps_xz_hat,'same'));
145 %         for j=1:n
146 %             Pt = (real(Pconv). cos(xs(j,:)) + imag(Pconv). sin(xs(j,:)));
147 %             Px(i,j) = ds sum(W. Pt)/(2 pi);
148 %         end
149
150 end
151
152 % [X,Z] = meshgrid(x,nodes);
153 % figure
154 % surf(X,Z,Px,'edgecolor','none')
155
156 % TIME = toc;
157 % disp(TIME)
158
```

```matlab
159  % figure
160  % plot(nodes,dEz)
161  % figure
162  % plot(nodes,dPz)
163
164  n_cl = find(abs(abs(x)-R) < 1e-2); n1 = min(n_cl); n2 = max(n_cl);
165  x_sg1 = x(1:n1) + u(1:n1); x_ls = x(n1:n2) + u(n1:n2); x_sg2 = x(n2:n) +
          u(n2:n);
166  z_sg1 = w(1:n1); z_ls = w(n1:n2); z_sg2 = w(n2:n);
167  L_sg = parametric_arclength2(x_sg1,z_sg1) + parametric_arclength2(x_sg2,
          z_sg2);
168  L_ls = parametric_arclength2(x_ls,z_ls);
169
170  x_sg1_dt = x(1:n1) + u_dt(1:n1); x_ls_dt = x(n1:n2) + u_dt(n1:n2);
          x_sg2_dt = x(n2:n) + u_dt(n2:n);
171  z_sg1_dt = w_dt(1:n1); z_ls_dt = w_dt(n1:n2); z_sg2_dt = w_dt(n2:n);
172  L_sg_dt = parametric_arclength2(x_sg1_dt,z_sg1_dt) +
          parametric_arclength2(x_sg2_dt,z_sg2_dt);
173  L_ls_dt = parametric_arclength2(x_ls_dt,z_ls_dt);
174
175  %Power dissipated:
176  P_diss = G v/pi dPz weights;
177  %Elastic and surface energies at current stiffness:
178  E_elastic = G/pi dEz weights;
179  E_surface = gam Ldrop + Ups ( L_ls + L_sg - 2 X R);
180  %Elastic and surface energies at future stiffness:
181  E_elastic_dt = (G+Gp dt v)/pi dEz_dt weights;
182  E_surface_dt = gam Ldrop + (Ups-Up v dt) ( L_ls_dt + L_sg_dt - 2 X R);
183  %Energy rate gained by migration:
184  %P_mig = (E_elastic - E_elastic_dt)/dt;
185  P_mig = (E_elastic + E_surface - E_elastic_dt - E_surface_dt)/dt;
186
187  disp([P_diss,P_mig,P_mig/P_diss])
188
189  % %Replicating dissipation approximation in Karpitshka's and Zhao's
```

```
        papers
190  % tauzz_hat = N − Ups s_sq . FTw;
191  % %P_diss_K = v / ( 2 pi ) sum( real ( tauzz_hat . fliplr ( 1 i s . FTw ) ) ) ;
192  % P_diss_K = −v / ( 2 pi ) ds real (sum( tauzz_hat . fliplr ( 1 i s . FTw ) ) ) ;
193  % P_diss_Z = −v / ( 2 pi ) ds real (sum( fliplr ( tauzz_hat ) . s . sign ( s ) . FTu ) ) ;
194  %
195  % % disp ( [ P_diss , P_mig ] )
196  % % disp ( P_diss / P_mig )
197  %
198  % disp ( [ P_diss , P_diss_K , P_diss_Z ] )
```